ULTRAFAST LASER-ABSORPTION SPECTROSCOPY IN THE MID-INFRARED FOR SPATIOTEMPORALLY RESOLVED MEASUREMENTS OF GAS PROPERTIES

by

Ryan J. Tancin

A Dissertation

Submitted to the Faculty of Purdue University

In Partial Fulfillment of the Requirements for the degree of

Doctor of Philosophy

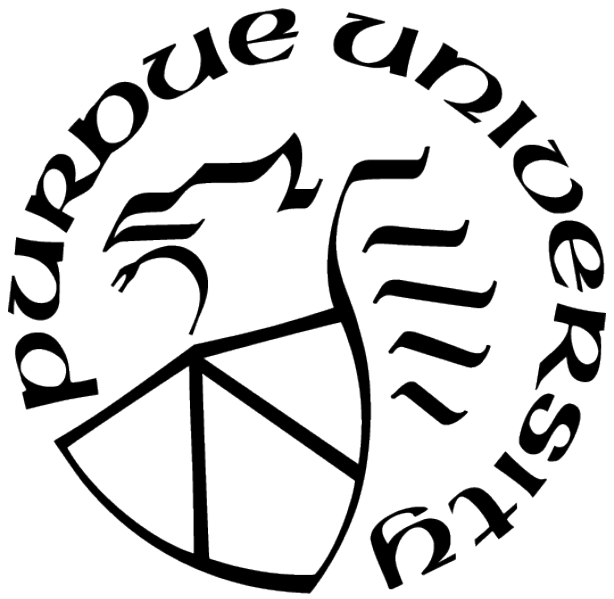

School of Aeronautics and Astronautics

West Lafayette, Indiana

May 2021

THE PURDUE UNIVERSITY GRADUATE SCHOOL
STATEMENT OF COMMITTEE APPROVAL

Dr. Christopher S. Goldenstein, Committee Chair

School of Mechanical Engineering and

School of Aeronautics and Astronautics (by courtesy)

Dr. Steven F. Son

School of Mechanical Engineering and

School of Aeronautics and Astronautics (by courtesy)

Dr. Robert P. Lucht

School of Mechanical Engineering and

School of Aeronautics and Astronautics

Dr. Terrence R. Meyer

School of Mechanical Engineering and

School of Aeronautics and Astronautics (by courtesy)

Approved by:

Dr. Gregory Blaisdell

To my parents, who gave me unconditional love and support through a long and challenging journey.

ACKNOWLEDGMENTS

I would like to offer special thanks to my advisor and mentor, Dr. Christopher Goldenstein who freely offered his help and impartial advice throughout my PhD in all facets of life, even if it was disadvantageous for him to do so. His patient guidance has made me into the engineer I am today.

I would also like to acknowledge my labmates for their countless hours of help in the lab on various projects. Their assistance, knowledge and ideas have played a vital role in many of my accomplishments at Purdue. Particularly, Garrett Mathews with whom I have spent many late nights in the office or lab, finishing assignments or working to make deadlines. The quality of his work and his knowledge of laser-absorption spectroscopy were a motivation for me to improve my own work and knowledge.

I have also had the privilege to explore areas outside my area of research at Purdue. Especially meaningful to me was the opportunity to satisfy a dream of building and testing a liquid-propellant rocket engine as part of the Purdue Space Program student rocketry club. In particular, I would like to thank Scott Meyer for sacrificing his personal time to help us learn new and unique skills, and allowing us to use facilities and equipment for construction and testing of our rocket.

I am, of course, also thankful to many other wonderful faculty at Purdue University. The faculty at Purdue are unique in their enthusiasm for collaboration, which is something I never take for granted. Their willingness to share equipment, funding, students and knowledge demonstrates that the best research is not done in isolation, and that one can achieve more by working with others than alone. I would especially like to thank my committee members: Dr. Son, Dr. Lucht, and Dr. Meyer. Dr. Son reached out to me and encouraged me to come to Purdue. He put me into contact with both Dr. Goldenstein and Dr. Meyer and encouraged me to consider joining their research groups in addition to his own, an embodiment of Purdue's culture of collaboration. His knowledge of energetic materials helped me to identify the "right" questions and learn how to answer them. Dr. Lucht has also provided valuable help to me during my PhD. In particular I would like to thank him for trusting me to operate

his ultrafast laser system and for helping me to better understand its operational principles and troubleshoot problems when they arose.

Designing and building the Purdue HPST was as challenging as it was fulfilling. Many of these challenges were overcome with help from Prof. Mitchell Spearrin of UCLA. Professor Spearrin, who had recently designed and built a shock tube facility for his own research group, shared his time and experience with me when my own designs hit a roadblock. Many of the lessons learned from his shock tube are now incorporated into the design and operational procedures of the Purdue HPST, due to Professor Spearrin's generosity.

Finally, I would like to thank the various sources which provided funding for the many projects I worked on while a Ph.D. student, especially Dr. Mitat Birkan's AFOSR program and the National Science Foundation.

TABLE OF CONTENTS

LIST OF TABLES

LIST OF FIGURES

LIST OF SYMBOLS

A	integrated absorbance [cm^{-1}] or geometric area [m^2]
c	speed of light in a vacuum [cm s^{-1}]
E"	lower-state energy [cm^{-1}]
g	degeneracy of a quantum state [pure]
h	Planck's constant [Js]
I_o	incident (i.e., baseline) laser intensity at detector or camera-spectrograph resolution [a.u.]
$I_{o,HR}$	baseline laser intensity at high resolution [a.u.]
$I_{o,HR,conv}$	baseline laser intensity post convolution with the IRF at high resolution [a.u.]
I_t	transmitted intensity at detector or camera resolution [a.u.]
$I_{t,HR,conv}$	transmitted laser intensity post convolution with the IRF at high resolution [a.u.]
k_B	Boltzmann constant [J/molecule-K]
L	optical path length through absorbing gas [cm]
m	molecular mass [kg]
n	collisional broadening temperature exponent [pure]
N	number density [m^{-3}]
P	pressure [atm]
Q	partition function sum [pure]
S	transition linestrength [cm^{-2}/atm]
t	time [s]
T	temperature [K]
T_0	reference temperature [296 K]
T_{CO}	temperature measured from path-integrated absorbance spectra of CO [K]
T_{CO_2}	temperature measured from path-integrated absorbance spectra of CO_2 [K]
v	velocity [m/s]
V	volume [m^3]

$\alpha(\nu)$	spectral absorbance [pure]
$\alpha_{HR}(\nu)$	simulated absorbance at high resolution prior to convolution with the IRF [pure]
$\alpha_{HR,conv}(\nu)$	simulated absorbance at high resolution after convolution with the IRF [pure]
$\alpha_{conv}(\nu)$	simulated absorbance at camera-spectrograph resolution after convolution with the IRF [pure]
γ	specific heat ratio [pure]
$\Delta\nu_C$	collisional-broadening FWHM [cm^{-1}]
$\Delta\nu_D$	doppler-broadening FWHM [cm^{-1}]
$\Delta\nu_N$	natural-broadening FWHM [cm^{-1}]
λ	optical wavelength [nm]
ν	optical frequency [cm^{-1}]
ν_o	linecenter frequency [cm^{-1}]
σ	standard deviation [a.u.]
$\phi(\nu)$	lineshape function [cm]
χ	species mole fraction [pure]
$\chi_{abs}L$	absorbing-species column density [cm]

ABBREVIATIONS

ANSI	American National Standards Institute
AP	ammonium perchlorate
ASME	American Society of Mechanical Engineers
CAD	computer aided design
CARS	coherant anti-Stokes Raman scattering
FPA	focal-plane array
FTIR	fourier-transform infrared spectroscopy
FWHM	full width at half maximum
HMX	1,3,5,7-tetranitro-1,3,5,7-tetrazoctane
HTPB	hydroxyl-terminated polybutadiene
ID	inner diameter
LAI	laser-absorption imaging
LAS	laser-absorption spectroscopy
LAT	laser-absorption tomography
LOS	line-of-sight
OD	outer diameter
SAE	Society of Automotive Engineers
SS	stainless steel
TDLAS	tunable diode-laser absorption-spectroscopy
ULAS	ultrafast-laser-absorption spectroscopy

ABSTRACT

Laser-absorption spectroscopy (LAS) is widely used for providing non-intrusive and quantitative measurements of gas properties (such as temperature and absorbing species mole fraction) in combustion environments. However, challenges may arise from the line-of-sight nature of LAS diagnostics, which can limit their spatial resolution and can complicate accurate interpretation of LAS measurements. Further, time-resolution of such techniques as scanned direct-absorption or wavelength-modulation spectroscopy is limited by the scanning speed of the laser and the optical bandwidth is often limited by a combination of a laser's intrinsic tunability and its scanning speed. The work presented in this dissertation investigated how recent advancements in mid-IR camera technology and lasers can be leveraged to expand the spatial, temporal, and spectral measurement capabilities of LAS diagnostics. In addition, the high-pressure combustion chamber (HPCC) and high-pressure shock tube (HPST) were designed and built to enable the study of, among others, energetic material combustion, spectroscopy, non-equilibrium and chemistry using optical diagnostics.

A brief overview of laser absorption spectroscopy is provided. The fundamental principles of absorption spectroscopy and statistical mechanics are described. Various physical and instrumental broadening mechanisms which are relevant to this dissertation are discussed.

The design and initial application of the HPCC is also presented in this work. The HPCC exhibits several unique design attributes which mitigate some of the challenges which complicate optical characterization of flames at high-pressure. The HPCC employs a flangeless and weldless design to provide a compact, easy to access, and relatively light weight (for its size and pressure capability) test chamber. It is capable of operating at pressures from vacuum to 206 bar, and it enables laser or wire ignition of propellants and energetic materials to be preformed. Some of the HPCC's testing capabilities are demonstrated via optical characterization of laser-ignited HMX flames. Laser-absorption-spectroscopy measurements of temperature and CO at 2 bar and high-speed IR imaging and at pressures from 2 to 25 bar are presented.

The design and initial application of a mid-infrared laser-absorption-imaging (LAI) technique for two-dimensional (2D) measurements and tomographic reconstruction of gas tem-

perature and CO in laminar flames is presented. In this technique, the output beam from a quantum-cascade laser (QCL) is expanded, passed through the test gas, and imaged in 2D using a high-speed mid-infrared camera. The wavelength of the QCL is scanned across the P(0,20) and P(1,14) transitions of CO near 4.8 μm at 50 Hz to provide 2D measurements of path-integrated gas temperature and CO column density across over 3,300 lines-of-sight simultaneously. This enabled the first sub-second (0.1 s), high-resolution (140 μm), 2D laser-absorption measurements and tomographic reconstruction of flame temperature and CO mole fraction using mid-infrared wavelengths. Prior to entering the test gas, the beam was reflected off two diffusers spinning at 90,000 RPM ($\approx$9400 rad/s) to break the laser's coherence and prevent diffraction-induced image artifacts. This technique was validated with measurements of CO in an isothermal jet and then demonstrated in laminar, partially premixed, oxygen-ethylene flames despite large background emission from soot and combustion products.

Next, the development of an ultrafast (i.e., femtosecond), mid-infrared, laser-absorption diagnostic and its initial application to measuring temperature, CO, and CH_4 in flames is presented. This diagnostic offers several unique advantages: (1) ultrafast (sub-nanosecond) time resolution, (2) access to strong fundamental absorption bands located throughout the mid-IR using a single light source and camera, and (3) potential for single-shot, spatially resolved (1D) thermometry and species measurements at 5 kHz. The diagnostic employs a Ti:sapphire oscillator emitting 55-fs pulses near 800 nm which were amplified and converted into the mid-infrared though optical parametric amplification (OPA) at a repetition rate of 5 kHz. The pulses were directed through the test gas and focused into an imaging spectrometer where they were dispersed and recorded using a high-speed, mid-infrared camera. Images of baseline or transmitted laser intensity were recorded with a spatial and spectral dimension, the latter of which contained $\approx$30 nm of bandwidth for the initial application of the diagnostic. Gas properties were determined by least-squares fitting simulated absorbance spectra to measured single-shot absorbance spectra. The diagnostic was validated with measurements of temperature, CO, and CH_4 in a static-gas cell with an accuracy of 0.7% to 1.8% of the known values. Single-shot, 5 kHz measurements of temperature and CO were acquired near 4.9 μm in a laser-ignited HMX (i.e., 1,3,5,7-tetranitro-1,3,5,7-tetrazoctane) flame and exhib-

ited a 1-σ precision of 0.4% at ≈2700 K. Further, CH_4 and temperature measurements were acquired near 3.3 μm in a partially premixed CH_4-air flame produced by a Hencken burner and exhibited a precision of 0.3% at ≈1000 K.

The ULAS diagnostic was refined through improvements made to the optical setup and data-processing procedure. This enabled the first single-shot, single-spectrum (i.e., no spatial averaging of spectra) measurements which demonstrates the feasibility of acquiring 1D temperature and absorbing species concentration measurements with ULAS. Further, the diagnostic was extended towards measuring CO_2. Wavelengths near 4975 nm and 4186 nm were used to measure spectra of CO and CO_2, respectively, with a spectral bandwidth and resolution near 30 nm and 0.3 nm, respectively. Temperature, CO, and CO_2 column density were measured at a repetition rate of 5 kHz in laser-ignited HMX flames in an air bath gas. Measurements for each species were acquired at the same location in the flame, under identical conditions. The results demonstrate that this diagnostic can provide single-shot temperature measurements via CO or CO_2 with a time resolution less than 1 nanosecond and a 1-σ precision of ≈1-2%. Species-specific differences in the measured path-integrated temperature were used to provide additional insight into the structure of HMX flames burning in air.

A multi-spectrum fitting routine was used to infer instrument broadening parameters for ULAS-acquired transmitted intensity spectra. A heated static-gas cell with an internal path length of 9.4 cm was filled with a mixture of 2% CO by mole and heated to ≈1000 K. ULAS measurements of absorbance spectra were acquired at pressures of 0.3, 1, 3, 10, 20, and 40 bar. The multi-spectrum fitting routine fit spectra acquired at 0.3, 1, 3, and 40 bar simultaneously with a single IRF and a single correction factor on collisional broadening FWHM. This technique allowed for robust determination of instrument broadening parameters by, among others, decoupling the effects of collisional and instrument broadening. The instrument broadening parameters were validated by processing heated-gas cell measurements one-at-a-time with the instrument broadening parameters held constant. The fitting routine returned accurate results for datasets acquired using different grating resolutions, and from datasets acquired using rebuilt optical setups. The instrument broadening parameters returned by the multi-spectrum fitting routine are consistent with those measured using a narrowband (≈

1 MHz) laser (QCL). The potential effects of spectral interpolation methods and incomplete knowledge of the non-absorbing baseline on ULAS-acquired absorbance spectra are also discussed.

Lessons learned from the multi-spectrum fitting routine were applied to enable characterization of AP-HTPB propellant flames using the CO-based ULAS diagnostic. Single-shot measurements of temperature and CO were acquired at 5 kHz near 4.9 μm. AP-HTPB flames were first characterized at atmospheric pressure in air, N_2, and Ar bath gases at locations 2 mm, 2 cm and 4 cm above the burning surface. Measurements of CO absorbance spectra were acquired using a diffraction grating with 300 lines/mm which provided a bandwidth and spectral resolution near 30 nm and 0.3 nm, respectively. A DSLR camera recorded tests in order to provide an estimation of the absorbing path length. Time-averaged temperature and CO mole fraction (χ_{CO}) measurements acquired in different bath gases and at different heights are used to gain insight into the effect of bath gas on solid-propellant flames.

The first application of ULAS to characterizing high-pressure (up to 40 bar), multi-phase combustion gases is also presented here. Single-shot measurements of CO spectra were acquired using a diffraction grating which provided 86 nm of bandwidth and a spectral resolution of $\approx$0.6 nm. A system of corrective optics was employed to diminish the effects of beam steering during high-pressure experiments, thus, greatly increasing the pressure capabilities of the diagnostic. Single-shot measurements of T and χ_{CO} were acquired in AP-HTPB propellant flames in an argon bath gas at pressures of 1, 10, 20, and 40 bar. An aluminized AP-HTPB propellant was also characterized at 10 and 20 bar to demonstrate that ULAS can provide high-fidelity measurements in multi-phase propellant flames. The results demonstrate that ULAS is capable of providing single-shot temperature and species measurements at high pressures with 1-σ precisions less than 1.1% and 3% for temperature and species respectively, despite non-absorbing transmission losses up to 90%.

A high-pressure shock tube (HPST) was designed and constructed at Purdue which will enable gases and plasmas to be studied at high temperatures and pressures. The basic operational procedure of a shock tube experiment is described, and x-t diagrams for visualizing the evolution of gas conditions in space and time are introduced. The HPST is 12.6 m long with an internal diameter of 10.3 cm and it is capable of generating gases at

pressures up to 280 bar and temperatures in excess of 10,000 K. Tube sections and inline components are joined with custom, weldless flanges which reduced the weight of bolted connections by $\approx 85\%$. Optical measurements at or near the test section endwall are facilitated by windows enabling 5 lines-of-sight. Notably, a pair of slot-shaped windows with a maximum clear aperture of 57 x 20 mm are used at one location to facilitate 1D measurements of gas properties. The diaphragm holder employs a breech-screw design to allow for rapid changing of diaphragms, minimizing the time between successive experiments. Detrimental effects from improper diaphragm bursting (e.g., fragmentation, slow bursting times, incomplete diaphragm bursting/small opening area and asymmetric bursting) were mitigated through careful design of the diaphragm holder. The driven section of the tube is designed to be capable of high-vacuum, supporting state 1 conditions needed for, among others, high-temperature, low-pressure tests, as well as tests requiring precise knowledge of gas composition. A custom, large-diameter poppet valve reduces the time needed for achieving high vacuum and lowers the minimum pressure of the tube while maintaining a smooth inner bore to prevent interruption of the incident shock wave. Numerous access ports allow for gas delivery, venting, and instrumentation such as pressure transducers and shock arrival sensors.

1. INTRODUCTION

Combustion systems play an important role in modern life, dominating the transportation, energy, space and defense sectors. Civilization's reliance on combustion systems is long standing, yet they are still subject of intense research and development. Increasingly, research has been focused on reducing pollutant emissions (for public health and environmental considerations) and increased efficiency (to reduce greenhouse-gas emissions and operating costs). Innovative combustion-based technologies such as rotating detonation engines, carbon-free or carbon-neutral fuels, and advanced solid-propellant formulations require advanced diagnostics in order to study and characterize their performance. The demand for better measurements and in more unique and challenging diagnostic environments continues to propel advancements in hardware, techniques and data processing.

Laser-absorption spectroscopy diagnostics are useful tools for characterizing practical combustion devices and characterizing fundamental combustion physics [1]–[5]. These diagnostics are capable of acquiring non-invasive, time-resolved, and quantitative measurements of temperature, pressure, velocity, and species concentration [1]. However, much work is being done by numerous research groups to solve some of the many remaining challenges for advancing LAS diagnostics, namely, mitigating difficulties associated with acquiring high-pressure measurements, developing techniques which rely on multiple lines-of-sight to reduce the effect of line-of-sight non-uniformities, improving time-resolution and measuring more chemical species [6]–[12]. In this dissertation, I present the development of novel solutions for addressing these challenges via a high-speed mid-IR camera and both tunable and ultrafast lasers.

This dissertation is organized in the following manner:

- **Chapter 2** provides an overview of the fundamental principles of laser-absorption spectroscopy and the physics which govern the measured absorbance spectra.
- **Chapter 3** details the design and construction of the high-pressure combustion chamber (HPCC) and describes the numerous novel aspects of this combustion facility which mitigate many of the challenges with acquiring optical measurements at high-pressure.

Scanned-DA measurements of temperature and CO and high-speed IR imaging which were acquired in HMX flames at high-pressure inside the HPCC are also presented.

- **Chapter 4** describes a novel laser-absorption-imaging diagnostic which provides 2D measurements of temperature and absorbing-species mole fraction with unprecedented spatial resolution.

- **Chapter 5** presents the development of ultrafast-laser-absorption spectroscopy (ULAS); a novel diagnostic yielding mid-IR LAS measurements with unprecedented time resolution. Initial flame measurements of CH_4 and CO are presented. The broad wavelength range of the ultrafast laser as well as an improved optical setup are utilized to leverage species-specific temperature differences yielding an in-depth characterization of HMX flames in air.

- **Chapter 6** discusses considerations for the modeling of spectra for broadband, spectrometer-based absorption measurements. A multi-spectrum fitting strategy for inferring instrument broadening parameters is presented. The effect of various data interpolation methods and knowledge of the non-absorbing baseline laser-intensity on modeled spectra is examined.

- **Chapter 7** presents the extension of ultrafast-laser-absorption spectroscopy to high-pressure combustion gases. AP-HTPB composite propellant flames are characterized in various bath gases and at pressures up to 40 bar.

- **Chapter 8** details the development of a shock-tube facility for studying gas dynamics, chemical kinetics, combustion, heat transfer and spectroscopy.

2. FUNDAMENTALS OF ABSORPTION SPECTROSCOPY

2.1 Fundamental Principles

Individual molecules can possess energy in various forms, namely, translational (the velocity of a molecule), rotational (spinning on one of its axes), vibrational (though bending and stretching of bonds) and electronic (through the occupied electron energy levels). From quantum mechanics, it is know that energy stored in any of these forms may only take on quantized values. Energy can be transferred to or from a molecule though collisions with other atoms or molecules or though emission or absorption of a photon. Importantly, the increment of energy transferred must correspond to the difference between any two quantum states. It is also important to note that transitions between a molecule's quantum states can only happen if it is "allowed" by quantum mechanics. These principles are related to absorption spectroscopy by considering the combined effect of many molecules constituting a gas, and many photons contributing to the intensity of a laser beam or other light source. The Beer-Lambert Law (Eq. 2.1), as shown here can then be used to describe how monocromatic light is absorbed in a homogeneous medium as a function of gas properties [1], [13].

$$\frac{I_t}{I_o} = \mathrm{e}^{\alpha(\nu,P,T,\chi,L)} \tag{2.1}$$

2.2 Statistical Mechanics

Quantum mechanics determines the allowed energy levels for translational, rotational, vibrational and electronic modes of energy. In most applications of LAS (particularly for combustion), systems contain vast quantities of molecules, and it becomes useful to determine the proportion of molecules in a given quantum state.

For a system containing an amount of energy, E, there are many ways that the energy can be distributed across different molecules and energy levels. For a system in equilibrium, the proportion of molecules in a given energy state for a given temperature (within the dilute

limit: high temperature and low particle density) is described by the boltzmann distribution, which is given by Eq. 2.2, where j refers to a given rovibrational transition [13].

$$\frac{N_j}{N} = \frac{g_j \mathrm{e}^{-E_j/k_b T}}{\sum_j g_j \mathrm{e}^{-E_j/k_b T}} = \frac{g_j \mathrm{e}^{-E_j/k_b T}}{Q(T)} \tag{2.2}$$

2.3 Absorbance

Generally speaking, laser-absorption experiments involve passing a laser beam through a test gas and recording the transmitted light on a detector or camera. The recorded transmitted intensity is compared to a predicted or empirically measured baseline laser intensity using Eq. 2.1 to calculate the measured spectral absorbance as a function of thermodynamic properties (e.g., T, P, etc.).

In this work, rovibrational absorbance spectra are measured to determine gas properties. Rovibrational spectra are located in the infrared region of the electromagnetic spectrum, and they correspond to a change in vibrational and rotational quantum numbers [1], [13]. In order to relate the measured absorbance spectrum to gas properties, it is necessary to be able to accurately predict absorbance spectra as a function of those properties. The spectral absorbance is related to gas properties through Eq. 2.3.

$$\alpha(\nu) = \int_0^L \sum_j S_j(T(l)) P(l) \chi_{abs}(l) \phi(\nu) dl \tag{2.3}$$

This equation illustrates how the path-integrated absorbance from each individual absorption transition can be calculated from spectroscopic parameters and knowledge of thermodynamic properties along the measurement path [1], [14]–[16]. In particular, spectral absorbance is dependant on the pressure ($P(l)$), absorbing species mole fraction ($\chi_{abs}(l)$), absorbing path length (L), linestrength ($S_\mathrm{j}(T(l))$) and lineshape ($\phi(\nu)$). Parameters which are a function of l vary along the measurement line-of-sight in a non-uniform environment. The Linestregth and lineshape will be discussed in more detail in the following sections. The total absorbance at a given frequency is the sum of the contributions from each individual absorption transition, assuming isolated lines (i.e., linemixing is insignificant).

2.3.1 Linestrength

The linestrength is a temperature dependant parameter that describes the strength of an absorption transition. For a gas in thermal equilibrium, the linestrength scales with temperature according to Eq. 2.4. The equation here yields linestrength in the pressure-normalized convention, in which linestrength has units of $\mathrm{cm}^{-2}/\mathrm{atm}$ [1], [13]–[16].

$$S_j(T) = S_j(T_o)\frac{Q(T_o)}{Q(T)}\frac{T_o}{T}\exp\left[-\frac{hcE_j^{"}}{k_B}\left(\frac{1}{T}-\frac{1}{T_o}\right)\right]\left[1-\exp\left(\frac{-hc\nu_o}{k_BT}\right)\right]\left[1-\exp\left(\frac{-hc\nu_o}{k_BT_o}\right)\right]^{-1} \tag{2.4}$$

Eq. 2.4 takes into account temperature and number density for the lower energy state (and therefore the relative population in the lower energy state according to Boltzmann statistics) as well as the probability of stimulated absorption and emission for a photon with the requisite energy according to Einstein's theory of radiation.

2.4 Line-Broadening Mechanisms and Lineshapes

Until now, transitions have been discussed as occurring at a discrete frequency. However, in reality there are several mechanisms which spectrally broaden absorption lines. Broadening mechanisms which effect molecules of given species equally can be classified as homogeneous and result in a Lorentzian lineshape profile. Those which affect molecules depending on some other class which they belong to (e.g., molecules with different velocities having different Doppler shifts) are classified as inhomogeneous broadening mechanisms and result in a Gaussian lineshape profile. Additionally, there are mechanisms which narrow absorption lines (e.g., Dicke narrowing), though, these are comparatively weaker processes which do not significantly impact the measurements presented in this dissertation. Hence, they will not be discussed here.

2.4.1 Natural Broadening

Natural broadening occurs due to the inherent uncertainty in the energy of the upper and lower quantum states due to the Heisenberg uncertainty principle [13].

$$\Delta E \Delta t \geq h/2\pi \tag{2.5}$$

From the uncertainty principle (Eq. 2.5) it can be seen that as the lifetime of a molecule in a given state decreases, the uncertainty in energy and, therefore, the natural broadening must increase. For rovibrational transitions, $\Delta\nu_N$ (natural broadening FWHM) is typically less than 10^{-6} cm^{-1} for the conditions prevalent in the work presented here, and thus can be neglected. Natural broadening is a homogeneous broadening mechanism and, therefor, it has a Lorentzian contribution to the overall transition lineshape.

2.4.2 Collisional Broadening

Collisions between molecules can reduce the lifetime of molecules in a given energy state and lead to collisional dephasing, both of which broaden energy levels. The increased uncertainty in the lifetime of a molecule in a given state yields increased uncertainty in the energy of the state due to the Heisenberg uncertainty principle (Eq. 2.5) [1], [13]. The collisional FWHM can be calculated using Eq. 2.6 [1], [13], [14], [16].

$$\Delta\nu_c = 2P \sum_A \chi_A \gamma_{B-A}(T) \tag{2.6}$$

Here, χ_A is the mole fraction of the collision partner and $\gamma_{B-A}(T)$ is the collisional broadening coefficient of absorber B with collision partner A. Collisional broadening is a homogeneous broadening mechanism and, thus, its contribution to the overall transition lineshape is Lorentzian. The temperature dependence of $\gamma_{A-B}(T)$ is given by Eq. 2.7.

$$\gamma_{B-A}(T) = \gamma_{B-A}(T_0)\left(\frac{T_0}{T}\right)^n \tag{2.7}$$

T_0 is the reference temperature (296 K) and n is the temperature exponent ($n = 0.5$ for a hard sphere approximation, but n typically varies between 0.5 and 1).

2.4.3 Doppler Broadening

Doppler broadening arises from the doppler shift created by the velocity of a molecule relative to that of an incident photon. Assuming a Gaussian velocity distribution, the lineshape contribution from Doppler broadening is also Gaussian. The FWHM of a Doppler-broadened transition line is given by Eq. 2.8 [1], [13], [16].

$$\Delta\nu_D = 2\sqrt{\frac{2k_B T ln(2)}{mc^2}}\nu_0 \tag{2.8}$$

2.4.4 Voigt Lineshape Function

In nature, transitions are not broadened by a single mechanism, but by each of these previously discussed mechanisms (as well as others) simultaneously. Hence, it is often not valid to assume either a Lorentzian or Gaussian transition lineshape alone. The most common lineshape function used is the Voigt profile, which accounts for both collisional and Doppler broadening through the convolution of the two profiles [1], [13]–[16]. It is important to note that the Voigt profile is an approximation of the true transition linshape. One of the key assumptions for using the Voigt profile is that collisional and Doppler broadening effects are decoupled, which in reality is not always true [13]. In some cases more advanced lineshape models are utilized, to account effects such as collisional narrowing [14].

2.5 Instrument Broadening

The previous section discussed line-broadening mechanisms which can be categorized as physical broadening mechanisms, or in other words, those which result from characteristics of the absorbing atom or molecule and the properties of its environment. Instrumental broadening mechanisms are those which are a consequence of the equipment and methods used to make the measurement. Instrument broadening mechanisms include (but are not

limited to) the slit function of spectrometers, spectrographs, and monochromators, the laser linewidth in the case of scanned-wavelength measurements and power broadening; when the optical intensity is sufficient to perturb the measured energy states. The laser linewidth for most scanned-wavelength lightsources is typically much smaller than absorption linewidths at combustion-relevant conditions and, thus, is often neglected. The slit function is often much larger and is usually accounted for in post-processing of measurements. Power broadening can be avoided by maintaining sufficiently low optical intensities in the experimental setup [13].

3. HIGH-PRESSURE COMBUSTION CHAMBER

The contents of this section are adapted with permission from [6], Review of Scientific Instruments.

3.1 Introduction

Combustion in practical energy and propulsion systems such as rockets, gas turbines, or internal combustion engines is performed at elevated pressures in order to increase thermodynamic efficiency. As a result, controlled studies of combustion at high pressures are needed to understand the complex combustion physics governing these systems. The harsh conditions and small spatial and time scales associated with combustion often render traditional intrusive measurement tools such as thermocouples or gas sampling techniques (e.g., gas chromatography mass spectrometry) incapable of providing the necessary data. For these reasons, optical diagnostics ranging from visual imaging to advanced laser-spectroscopy techniques (e.g., absorption, fluorescence, Raman scattering etc.) are typically used to characterize the combustion process via time-resolved temperature and species measurements [1], [3]–[5]. Unfortunately, deploying optical diagnostics in high-pressure combustion environments is challenging due to a variety of spectroscopic challenges and the thermomechanical difficulties associated with achieving large optical access in such environments.

Despite these challenges, laboratory studies of combustion physics have been performed in a wide range of high-pressure facilities, namely: shock tubes[4], rapid compression machines[17], [18], and pressure chambers[10], [19]–[30]. The short test times associated with the former typically limit or preclude the study of flame physics, thus this work will focus on the latter. One of the earliest pressure chambers designed for combustion research was built in 1928 for the study of the effect of pressure on diffusion flame height[19]. More recently, Carter et al.[20] constructed a chamber from standard piping and bolt circle flanges to re-

duce cost. This chamber is constructed of 316 stainless steel and it is capable of operating at pressures up to 60 atm with four orthogonally oriented windows with a maximum clear aperture of 63.5 mm. The windows are mounted between flanges on a short section of pipe that is welded to the exterior of the chamber. The chamber was built to contain a flat flame burner on an x-y translation stage for studying the spatial evolution of chemical species in laminar and turbulent burner flames.

Soot formation in flat flames (e.g., McKenna burner flames) was studied using another chamber constructed from stainless steel in a similar manner to that of Carter et al.[20], but capable of operating at pressures up to 110 atm with a 24 cm inner diameter, 60 cm height and 27.1 L volume. However, this chamber weighs 700 kg and heavy machinery is required to move the large flanges and gain access to the chamber [21]–[23]. McCrain et al.[24] also studied soot formation in a Burke–Schumann laminar diffusion flame. The stainless steel chamber could sustain a pressure of 35 atm with an internal diameter of 20 cm, a height of 100 cm and a volume of 31.4 L. Large optical access was provided via viewports with a clear aperture of 4 mm x 76 mm which were also held externally via flanges and welded pipe. The chamber walls are water cooled such that water condenses on the walls instead of on the windows [24], [25].

Most recently Joo et al.[26] constructed a chamber with 4 orthogonally oriented windows with a clear aperture of 90 mm. The cylindrical test section of the chamber is capable of operating at pressures up to 35.5 atm, and it has a volume of 25 L, a 25.4 cm inner diameter and a height of 50 cm. Ignition can be achieved via hot-wire ignition or glow plugs. The burner in this chamber is interchangeable and is built into the lower flange of the chamber. The test volume of this chamber can be accessed without heavy machinery and a standard engine hoist can be used to easily move it to a different lab space.

Strand burners (used to measure burning rates of solid and liquid propellants) [10], [28]–[30] typically utilize a single screw plug to gain entry to the chamber and use slot-shaped windows to provide high visibility in the vertical direction. While optically accessible chambers employing this design can operate at higher peak operating pressures (e.g., 344 bar [30], 365 bar [10], 3,000 bar [29]), this has come at the cost of employing smaller test volumes (typically ≈1 L) and less optical access (compared to the design presented here) to provide

lower stress levels and facilitate operation at such high pressures [27]. Unfortunately, the use of smaller internal volumes leads to a larger pressure rise during a combustion test and also encourages product gas recirculation, both of which can alter flame physics and the accuracy of measurements acquired using path-integrated diagnostics (e.g., imaging, laser-absorption spectroscopy). Later in this chapter, we demonstrate that the HPCC does not suffer from these drawbacks. Further, many common burners (e.g., McKenna, Hencken) are too large to physically fit inside such chambers, thereby limiting the range of combustion experiments that can be conducted in such chambers.

In this chapter, the design and application of a High-Pressure Combustion Chamber (HPCC) are discussed in detail. The primary novelty of the HPCC lies in its unique combination of: 1) large test volume (13 L), 2) large optical access (e.g., 50.8 mm clear aperture round windows and 190.5 mm x 38.1 mm slot windows), 3) high peak operating pressure (up to 200 bar), and 4) ease of access and entry. To the best of our knowledge, the HPCC can provide more optical access (quantified in total clear aperture) at pressures up to 200 bar than any combustion vessel that has been reported in the open literature to date. The remainder of this chapter is focused on describing the design process in detail along with an explanation of design decisions and challenges. The chapter concludes with presenting a demonstration of some of the HPCC's testing capabilities. Specifically, high-speed IR images of laser-ignited HMX (i.e., 1,3,5,7-tetranitro-1,3,5,7-tetrazocane) and mid-infrared laser-absorption-spectroscopy measurements of path-integrated flame temperature and CO column density are presented at elevated pressures.

The HPCC and laser-ignition system are shown in Figure 3.1. The external height of the HPCC is 610 mm (24 in) and it has an outer diameter of 356 mm (14 in). The pressurized test volume is roughly cylindrical in shape with a height of 406 mm (16 in) and diameter of 203.2 mm (8 in), yielding a test volume of approximately 13.1 L. The vessel is constructed out of 17-4PH stainless steel to provide resistance to corrosive propellant-combustion products (e.g., HCl) while maintaining high strength. Stress calculations were performed using Solidworks' Finite-Element Solver and indicate that the HPCC can withstand pressures up to 200 bar with a safety factor of 2. The HPCC was hydrostatically proof tested (without windows) at a pressure up to 140 bar (limited only by the water pump). The body of the vessel has

large openings for threaded plugs (128.9 mm (5.07”) diameter) on the top and bottom of the vessel to provide access for setting up experiments and cleaning the test volume. The bottom plug has a tapered thread port to enable hot-wire ignition. Gas delivery, exhaust, pressure sensors and wire feedthroughs all connect to the HPCC body through tapered thread ports.

Optical access is achieved via two round sapphire windows (clear aperture of 50.8 mm (2 in)) and 2 sapphire slot windows (clear aperture of 190.5 mm (7.5 in) by 38.1 mm (1.5 in))

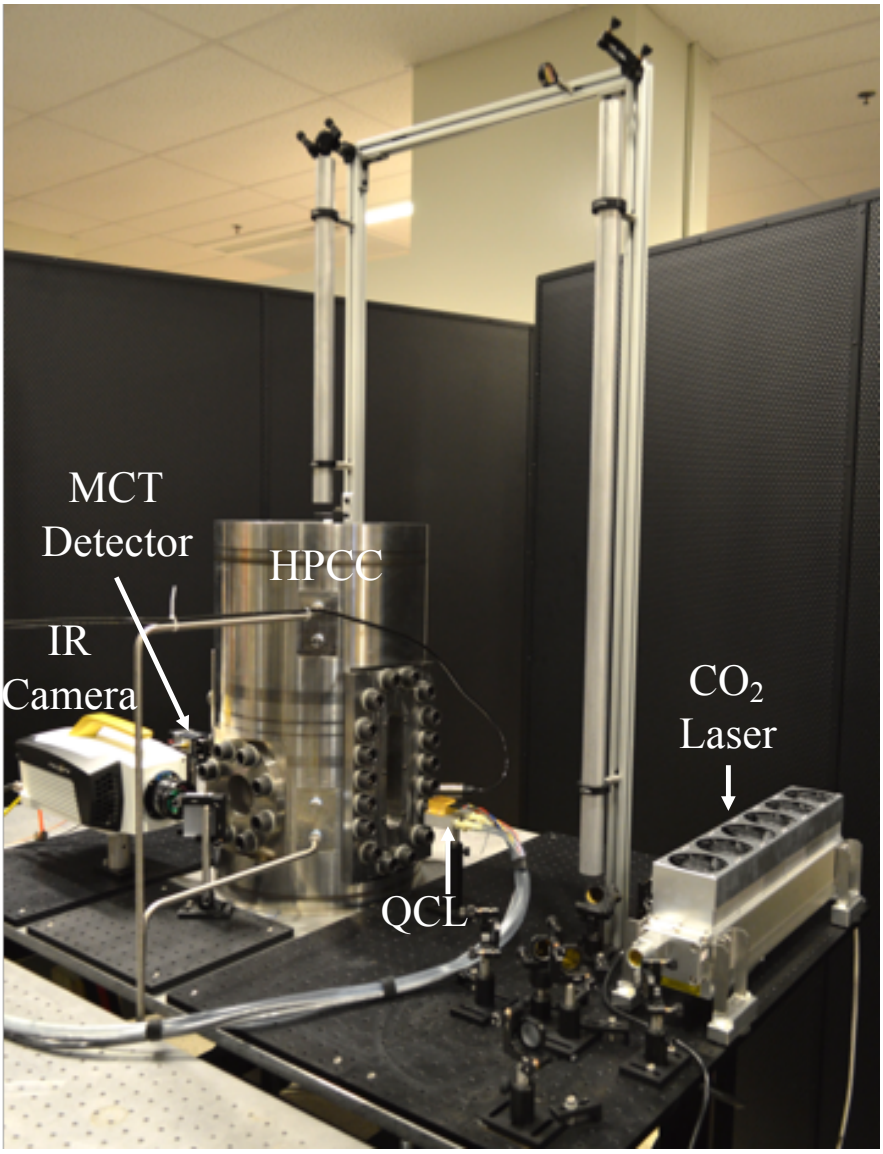

Figure 3.1. Photo of HPCC and experimental setup used to study laser-ignited HMX flames with IR imaging and laser-absorption spectroscopy.

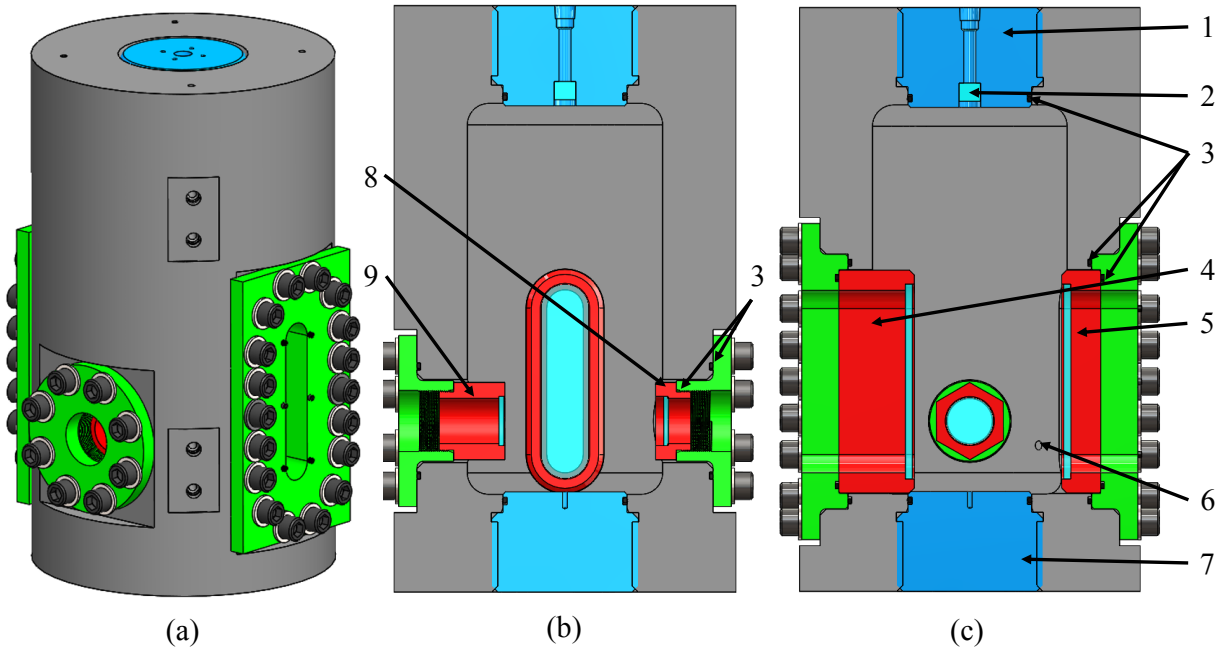

Figure 3.2. CAD model of the HPCC showing the exterior (a) and two radial cross sections (b and c). (1) Top plug, (2) ZnSe laser ignition window, (3) O-ring seals, (4) slot window holder extended into test volume, (5) slot window holder flush with inner wall, (6) gas inlet, (7) bottom plug, (8) round window holder flush with inner wall, (9) round window holder extended into test volume.

that are mounted in window plugs located on opposite sides of the chamber. All windows have a 1° wedge on their inner face to prevent the formation of etalons (i.e., optical fringes) in scanned-wavelength laser-absorption experiments. The flat face of each window is sealed to the shoulder of its window plug using EPO-TEK T7109 epoxy. If necessary, all windows can be extended inside the chamber to bring the windows directly adjacent to the flame and thereby mitigate the potential influence of line-of-sight non-uniformities on laser-absorption measurements. A ZnSe window with a 7.3 mm (0.5 in) clear aperture is mounted in the HPCC's top plug to enable laser-ignition of propellants using a CO_2 laser emitting 90 W of optical power near 10.6 μm.

3.2 Design Goals and Challenges

3.2.1 Optical Access

Optical diagnostics are widely used to characterize combustion science and systems due to their non-intrusive nature and ability to provide high-speed (kHz to MHz rate) measurements of gas properties (e.g., temperature, composition etc.) [1], [4], [31]. Two of the most widely used laser diagnostics in combustion are laser-absorption spectroscopy (LAS) and planar laser-induced fluorescence (PLIF). This section reports the design steps that were taken to enable high-fidelity LAS, PLIF, and imaging measurements of combustion in the HPCC.

The use of LIF and other imaging diagnostics is enhanced by using large windows to maximize the field of view and light collection. Further, LIF is typically performed by imaging orthogonal to the laser beam. To facilitate the use of these diagnostics, the HPCC was designed with four orthogonally oriented windows (see Figures 3.2 and 3.3), all with a clear aperture of at least 38 mm (1.5 in).

The accuracy of both LIF, LAS, and IR imaging measurements can be reduced by line-of-sight non-uniformities and optical trapping, for example, in product gases located outside the flame. This can be a concern when conducting measurements within a closed chamber where recirculation zones can transport combustion products away from the flame and then back into the measurement path but now at a drastically different temperature. As a result, it is desirable to minimize the distance over which the emission or laser light must travel outside the primary region of interest (i.e., the flame). To mitigate this risk, the HPCC employs a large test volume and was designed to enable the windows to protrude inside the HPCC. A similar approach was taken by Smith et al.[32] and Girard et al.[33] who used sapphire rods to direct laser light to and from flat flames in a low-pressure chamber. However, since this configuration is not desirable for all types of experiments, the window design is modular to enable many different window locations to be employed.

Both the round and slot shaped window assemblies employ a window holder and window mount (see Figure 3.3). The window mount is bolted to the outside of the chamber via a bolt circle and sealed to the HPCC body with a face seal O-ring. The window holder is fixed to the inner side of the window mount using bolts for the slot window and an ISO 11926-1 port

for the round window and sealed using face seal and ISO 11926-1 port O-rings, respectively. The sapphire windows are sealed directly to the window holders using a thermally removable epoxy (EPO-TEK T7109). Sealing the windows using epoxy instead of clamping the window between gaskets reduces the risk of breaking windows during installation and testing at high pressures. This method also allows wedged windows to be used to prevent etalons (i.e., optical fringes) from forming in scanned-wavelength laser-absorption measurements. The window holders can be made to different lengths allowing the windows to protrude inside the chamber, thereby adjusting the optical path length through the test volume. The window holders are relatively small and inexpensive to make, facilitating use of different window sizes and locations. To our knowledge, this modular window design is a unique attribute of the HPCC compared to other combustion chambers published in the literature.

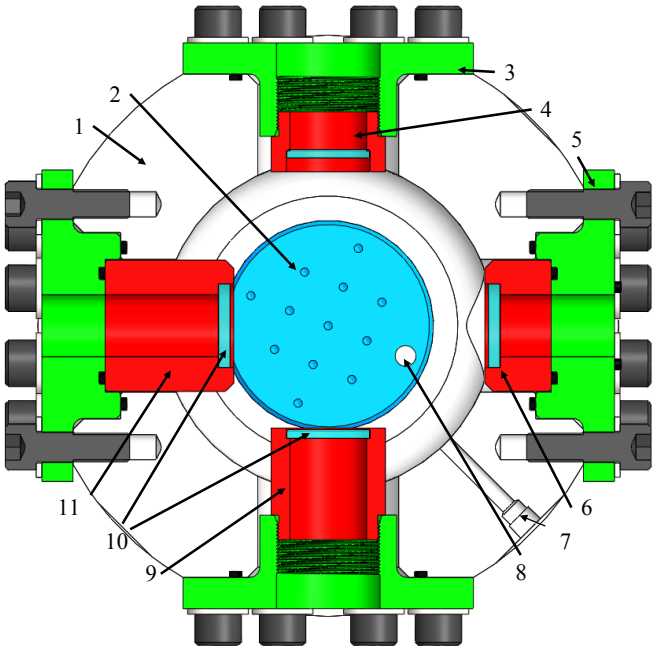

Figure 3.3. Transverse cross section of HPCC CAD model. (1) Chamber body, (2) bottom plug, (3) round window mount, (4) round window holder, (5) slot window mount, (6) slot window holder, (7) tapered thread port, (8) hot wire ignition port, (9) extended round window holder, (10) sapphire windows, (11) extended slot window holder.

FEA simulations of the initial design (performed using Solidworks) of the window holders and mounts indicated the presence of large stress concentrations. The geometry of the window holders, window mounts, and chamber body were iterated until a design with a minimum safety factor of two was achieved at 200 bar. Further, FEA simulations of each component attached to the HPCC were performed to ensure that part-chamber interactions do not adversely affect the strength of each part or the HPCC. For the round windows, the required window thickness was determined using Equation 3.1.

$$Th = \sqrt{\frac{1.1(P)(R^2)(SF)}{MR}} \tag{3.1}$$

Here, Th (in) is the window thickness, P (psi) is the chamber pressure, R (in) is the unsupported radius, SF is the desired safety factor and MR (psi) is the modulus of rupture of the window material. FEA simulations of windows mounted in the window holder were performed for the wedged slot windows to obtain a more accurate result due to their more complex geometry. The minimum acceptable SF of the windows was chosen to be 4 due to the increased risk of fracturing window materials. Both wedged round and wedged slot windows have been tested successfully in the chamber. The round and slot windows have a maximum thicknesses of 5 mm and 7.6 mm and SF=4 pressure ratings of 46.2 and 68.9 bar, respectively. To tolerate the maximum HPCC chamber pressure of 200 bar, the thickness of the round and slot sapphire windows would need to be 10.6 mm and 13 mm, respectively. During operation at elevated pressures, all personnel wear eye protection, and polycarbonate shields are placed around each of the windows to protect personnel in the event of a window failure.

3.2.2 Pressure Capabilities

The HPCC was designed to be suitable for studies of propellant flames and burner flames at both low and high pressures. The chamber is capable of operating at pressures as low as 0.4 mbar using a standard vacuum roughing pump and at pressures up to 200 bar. The former enables studies of low-pressure flat flames (e.g., for studying flame kinetics), while

the latter enables propellant burn rate measurements to be performed at pressures relevant to rocket motors.

Securing safe operation at pressures as high as 200 bar while maintaining large optical access and a large internal volume was extremely challenging. This is because the large internal volume and large holes providing optical access in the HPCC body lead to large stress concentrations. To withstand the high stress, the stainless steel alloy 17-4PH (ISO 15156, EN/DIN 1.4542 X5CrNiCuNb16.4, annealed condition A) was selected. This is because it has almost 3.5 times the yield strength of the more commonly used 316 or 304 stainless steel, yet is still easily available, machinable and relatively inexpensive. The high strength of this material enabled a minimum SF of 2 at 200 bar while also keeping the body to a reasonable size and weight (360 kg) which enables the HPCC to be relocated using a typical engine hoist.

Despite the high strength of the material used, the large stress created by the large test volume and high pressures required careful design of the chamber geometry. The most severe stress concentrations were found near the top inner edge of the window ports made for the slot windows. To reduce stress, the walls of the chamber were thickened to 76.2 mm (3 in) enabling them to support extreme loads despite the presence of large window ports. If the window ports were removed, this wall thickness would enable the chamber to withstand a pressure of 1216 bar with a safety factor of 2.1. Somewhat counterintuitively, stress was further reduced by widening the slot window ports. While this decreased the amount of steel available for support, it greatly increased the area where loads were previously concentrated near the top of the slots, thus reducing the stress. Stress and safety factors were determined using Solidworks Simulation's FEA package as mentioned previously.

Face seal O-rings were used wherever possible to provide low leak rates and to relax machining tolerances. For the slot window ports, the O-ring seat was recessed into the outside of the chamber such that there would be a smaller area for pressure to act laterally upon the sides of the slot and pull it apart (see Figure 3.3). Recessing the seat too far into the side of the chamber reduced the area on the top and bottom of the slots and increased stress. An optimal distance for recessing the seal was found by performing multiple FEA simulations and interpolating to the optimal seat depth. This design provides a leak rate of

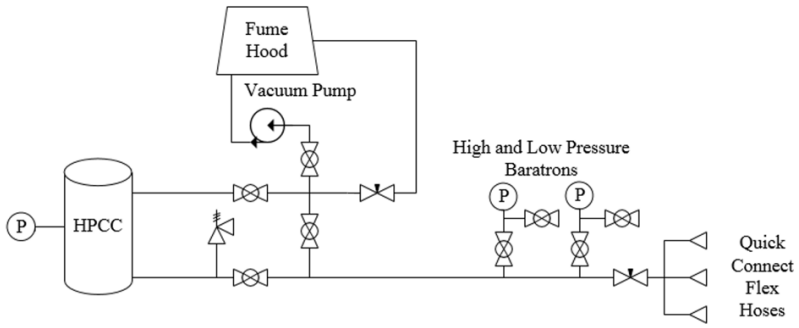

Figure 3.4. Plumbing and instrumentation diagram of the HPCC and gas manifold.

6.5 and 0.46 μbar/minute (at vacuum) to be achieved with windows and without windows (using solid window blanks), respectively.

3.2.3 Gas Delivery and Evacuation

Gases are delivered and removed from the HPCC via a high-pressure gas manifold shown in Figure 3.4. The manifold is connected to a vacuum pump to evacuate the chamber. The manifold also contains needle valves for controlling the flow of gases into and out of the HPCC and an adjustable relief valve to prevent over-pressurizing the test volume. The manifold can be connected to three gas-supply lines at once. The chamber can be vented directly into a fume hood to bring the chamber to atmospheric pressure and/or flush corrosive gases out of the chamber into an exhaust hood. The chamber can also be pumped down to vacuum through the gas manifold. The pressure in the manifold is measured using capacitance manometers with a range of 0 to 1,000 Torr and 0 to 10,000 Torr (both MKS Baratron 627F series). A 0 to 70 bar pressure transducer (Unik 5000 PDCR5011-TA-A3-CB-H0-PF-70BARA, 0.07 ms time response) is mounted directly to the HPCC to record the chamber pressure during a test.

3.2.4 Chamber Access and Support

Threaded plugs, similar to the Crawford bomb design[27], [28], are used to gain entry to the HPCC from the top and bottom (see Figure 3.2). These plugs utilize a piston-seal

O-ring for sealing and weigh only 13 kg. This design was chosen over a more commonly used flange-based design[23]–[25] to facilitate chamber access. For example, flanges that are suitable for this design and operating pressure weigh 39 kg each, which would require assistance from machinery to install and remove, thereby severely complicating access to the chamber. Further, this would increase the weight of the HPCC by 53% and would require a stronger and heavier support system.

A total of 7 NPT ports (2 x 1/4", 4 x 3/8", 1 x 1/2") at various locations around the chamber provide feedthrough access to the test volume. These ports can all support various types of feedthroughs which can be used for gas delivery, wires for sensors and hot-wire ignition, and power for control of actuators.

A custom table was designed to support the HPCC and enable removal of the bottom plug. When fully assembled the HPCC weights 360 kg (793.4 lbs) and an additional 50 kg of aluminum breadboards surround the HPCC to mount optics and other test equipment. Further, a 177.8 mm (7") diameter hole in the table is required to comfortably remove the bottom plug. To support this weight, the table top was made from a 1524 mm x 914 mm x

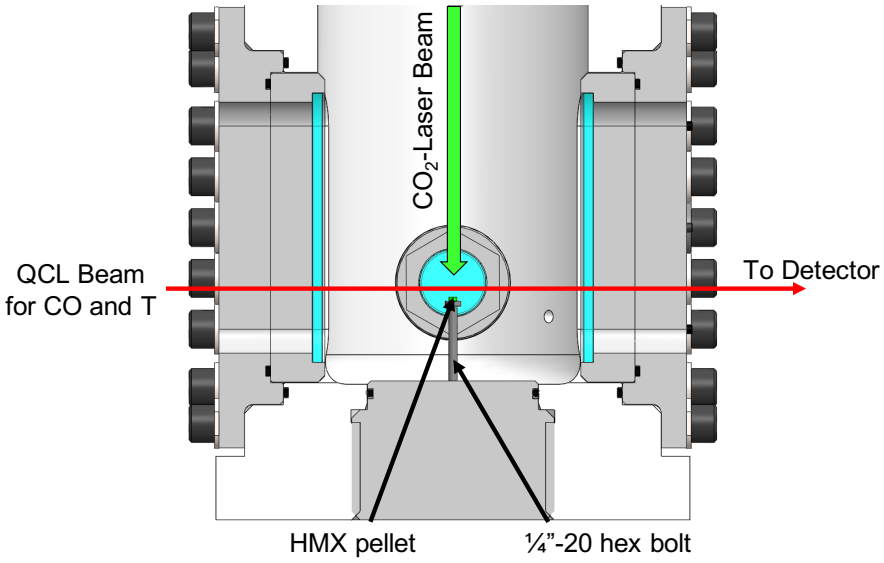

Figure 3.5. Cross-sectional view of HPCC model illustrating the location of the CO_2-laser beam and QCL beam used for laser-ignition of HMX pellets and laser-absorption-spectroscopy measurements of flame temperature and CO column density, respectively.

19 mm (60 in x 36 in x 0.75 in) slab of aluminum 6061-T6. The aluminum slab is supported by a ThorLabs Non-Isolating 800 mm Support Frame with a load capacity of 700kg.

3.3 Experimental Demonstration: Characterization of Laser-Ignited HMX

A portion of the HPCC's testing capabilities were demonstrated by performing laser-absorption-spectroscopy and IR imaging measurements of laser-ignited HMX flames at elevated pressures.

3.3.1 Experimental Setup

Figure 3.1 and Figure 3.5 illustrate the experimental setup used to characterize laser-ignited flames of HMX with laser-absorption spectroscopy and infrared imaging. A continuous-wave (CW) CO_2 laser (Coherent C70A) emitting up to 90 W of power near 10.6 μm was used to ignite pellets of pressed HMX (6 mm diameter, 3 to 5 mm tall). The laser beam was directed to the pressure vessel using a series of uncoated gold mirrors (R=98.82% at 10.6 μm) and the beam path was enclosed using aluminum beam tubes. An anti-reflection-coated ZnSe window was used as a beamsplitter to combine a visible (532 nm) alignment beam (produced by a 5 mW CW diode laser) onto the CO_2 laser's beam path. A 25.4 mm diameter, AR-coated ZnSe lens with a focal length of 1000 mm was used to reduce the diameter of the CO_2 laser's beam to 6 mm at the location of the HMX pellet which was located approximately 3.5 m from the CO_2 laser. Either air or N_2 were used as the bath gas.

A CW quantum-cascade laser (QCL) emitting 30 mW of optical power near 4.8 μm was used to acquire measurements of gas temperature and CO column density in HMX flames using scanned-wavelength direct absorption (scanned-DA) or scanned-wavelength-modulation spectroscopy with first-harmonic-normalized second-harmonic detection (scanned-WMS-$2f/1f$). The laser beam was directed through the HPCC at a location corresponding to 4 mm or 8 mm above the initial surface of the HMX pellet. The laser beam was collected by a 25.4 mm diameter, AR-coated CaF_2 lens with a focal length of 40 mm and focused onto a thermo-electrically cooled, mercury-cadmium telluride (MCT) detector (Vigo Systems PVI-4TE-5)

with a bandwidth of 10 MHz. A bandpass filter centered near 2060 cm^{-1} with a full-width at half-maximum of 40 cm^{-1} was used to reduce the infrared background emission.

In scanned-DA experiments, the wavelength of the QCL was scanned across the P(0,20) and P(1,14) absorption transitions near 2059.9 and 2060.3 cm^{-1}, respectively, at 500 Hz via injection-current tuning. The laser current was scanned below its threshold current to enable the background emission to be recorded between each scan. The wavelength scanning was characterized using a solid germanium etalon with a free-spectral range near 0.0163 cm^{-1}. A Voigt profile was least-squares fit to the measured spectra and the best-fit integrated absorbances were used to determine the path-integrated gas temperature and column density of CO ($\chi_{CO}L$) [34].

The flame temperature and CO column density were not measured at higher-pressures (>2 bar) since the increased collisional broadening and beamsteering prevented *in situ* determination of the incident light intensity (I_o) and reduced SNR, thereby severely complicating scanned-DA measurements. The former effect is illustrated in Figure 3.6 which shows simulated absorbance spectra for the absorption-transitions-of-interest at pressures of 1, 2, and 10 bar. At 10 bar, the spectra are significantly blended and a non-absorbing wavelength does not exist within the wavelength-tuning range of the QCL.

High-speed mid-infrared imaging was performed simultaneously orthogonal to the QCL's beam path. Images were obtained using the Telops FAST-IR 2K camera which employs a cryogenically cooled InSb focal plane array with 256 x 320 pixels. Images were recorded at 2000 frames-per-second (FPS) with an integration time of 7.5 μs. A bandpass filter (Spectrogon NB-3300-066 nm) centered near 3300 nm with a FWHM of 66 nm was used to pass emission from primarily carbonaceous species (e.g., HMX, HCN, formaldehyde) although some emission from H_2O's ν_3 fundamental vibrational band is also detected in this spectral window.

3.3.2 Experimental Results

Figure 3.7 illustrates select IR images acquired during laser-ignition of HMX in N_2 at 2 bar. The first image (a) illustrates the IR emission originating from the boiling surface of

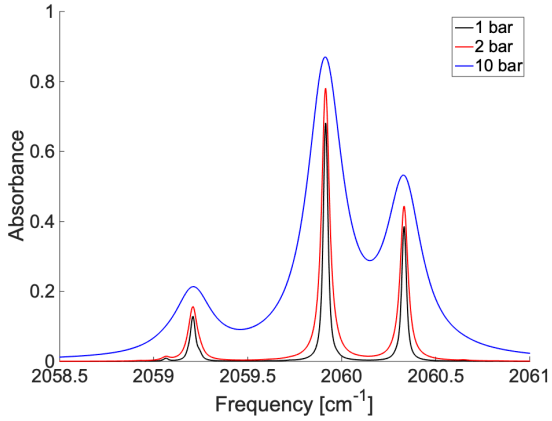

Figure 3.6. Simulated absorbance spectra of CO near 2059.5 cm^{-1} at various pressures for a gas temperature of 2750 K, CO mole fraction of 0.20, and path length of 1 cm. Absorbance spectra were calculated using the HITEMP2010 database [35]

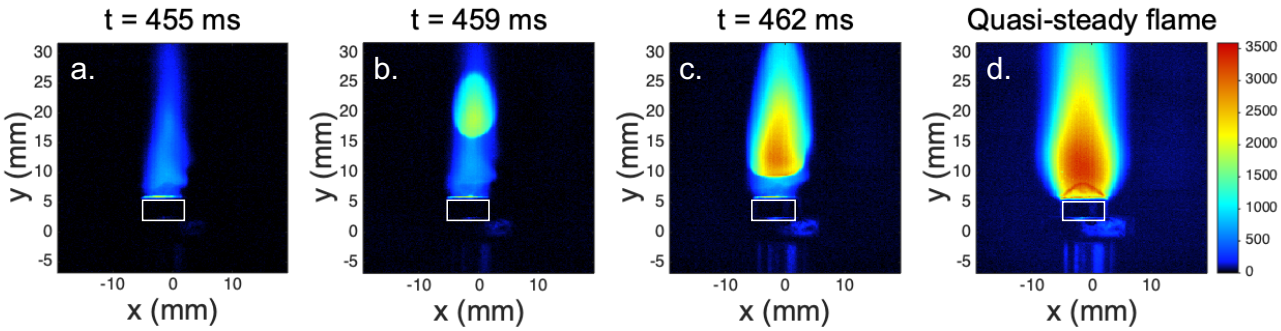

Figure 3.7. Infrared images of an HMX pellet (outlined by white box) undergoing laser ignition in an N_2 bath at 2 bar within the HPCC. Plume of HMX vapor prior to ignition (a), ignition kernel (b), flame front propagating towards surface (c), and quasi-steady flame (d).

HMX and the warm HMX vapor coming off the surface. The second image (b) illustrates the formation of an ignition kernel located above the surface, and the third image (c) illustrates the flame front propagating downward to the boiling surface. The last image (d) illustrates the flame structure as it burns in a quasi-steady state. Figure 3.8 illustrates the structure of HMX flames at 2, 10, and 25 bar. At all pressures, the flames exhibit structure characteristic of laminar premixed flames and the flames propagate linearly down the pellet with little edge burning observed. At 2 bar, a reaction front is visible approximately 2 mm above

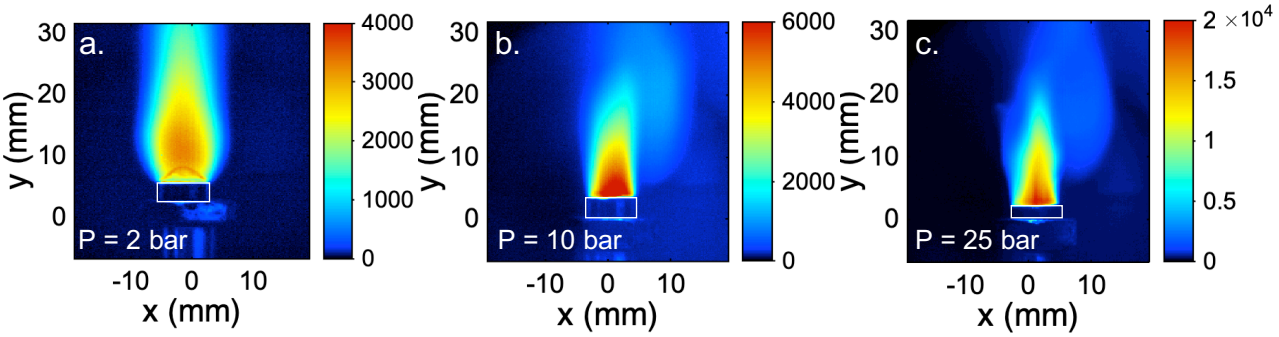

Figure 3.8. IR images of quasi-steady HMX flame in N_2 at 2 bar (a), 10 bar (b), and 25 bar (c). The images illustrate how increasing the bath gas pressure brings the primary reaction front closer to the surface and narrows the flame.

the surface. Surface boiling and miniature surface eruptions are observed throughout the burn period. At 10 and 25 bar, the reaction front is too close to the surface to observe with the optics employed here. Further, the IR image of the flame at 25 bar indicates significant narrowing of the flame core, which may result from alterations in the local flame temperature or concentration of various species emitting in this spectral window. That said, care must be taken in interpreting these images as the intensity of the infrared emission observed exhibits complex dependencies on gas temperature, pressure, and composition[13]. The combination of these results illustrate the ability of IR imaging (unlike visible imaging) to spatially and temporally resolve the entire laser-ignition process, from surface heating through flame holding.

Figure 3.9a shows a representative single-scan measurement of CO's absorbance spectra near 2060 cm^{-1} for a line-of-sight directed through the HMX flame 8 mm above the burning surface at a pressure of 2 bar. The best-fit Voigt profiles were determined using the integrated area, transition linecenter, and collisional width of each transition as free parameters. The Doppler width was initially fixed to the value corresponding to a guess temperature, and then updated according to the measured temperature (obtained from the two-color ratio of integrated areas) obtained from the previous iteration. The incident light intensity was inferred from fitting a 3rd-order polynomial to the non-absorbing regions of the transmitted intensity time history. Background emission was measured in between scans and subtracted from the measured light intensity prior to calculating the absorbance using Beer's Law.

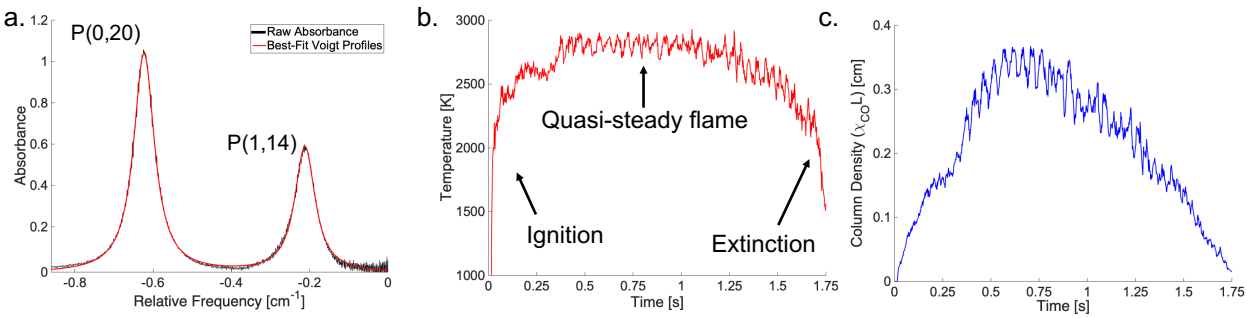

Figure 3.9. Scanned-DA results acquired in HMX flames in air at 2 bar. Measured and best-fit absorbance spectra of CO's P(0,20) and P(1,14) transitions (a), and measured temperature (b) and CO column density (c) time histories. All measurements were acquired at 500 Hz using a line-of-sight located 8 mm above the initial surface location.

Figures 3.9b and 3.9c show time histories of the measured temperature and CO column density ($\chi_{CO}L$), respectively, for a laser-ignited HMX flame in air at 2 bar. After ignition, the flame temperature rises up to near 2750 K which agrees well with radiation-corrected thermocouple measurements acquired at 1 bar using a similar laser fluence for ignition and surface heating[36]. Approximately 300 ms after ignition the path-integrated flame temperature begins to oscillate at approximately 21 Hz with an amplitude of ± 80 K. The 21 Hz oscillation is clearly noticeable in visible and infrared imaging of the HMX flame, and it is well known that HMX flames exhibit natural oscillations [36], [37]. However, to our knowledge the magnitude of the temperature oscillation has not been quantified previously. After accounting for the actual temperature oscillation, the 1-σ precision of the temperature measurement is ± 10 K and efforts to rigorously quantify the measurement accuracy are ongoing. The CO column density oscillates in phase with the temperature oscillation. This is intuitive given that CO is a primary combustion product of HMX. In addition larger CO column density corresponds to a thicker flame which could encourage greater heat release and help insulate the flame core.

In each experiment, the pressure increased by approximately 3.9% during the burn period which indicates that a constant-pressure assumption is appropriate for these experiments. In addition, window extensions were not used to reduce the optical path to include only the flame since there was no evidence of combustion products being transported back into

the optical line-of-sight (e.g., due to recirculation) during the test duration. For example, immediately after the flame extinguished, CO could not be detected in the chamber via the laser-absorption sensor for at least 5 seconds. This results from a combination of the large test volume of the HPCC and the relatively small HMX pellets burned here.

4. LASER-ABSORPTION IMAGING AND TOMOGRAPHY

4.1 Introduction

While single line-of-sight LAS measurements are extremely useful, many combustion applications demand multi-dimensional measurements of chemical species and thermodynamic conditions, for example, to resolve the thermochemical structure of flames and/or, more generally, the spatiotemporal evolution of combustion. To meet this need, LAS diagnostics employing multiple LOS [38]–[44] or mechanical scanning of the LOS [34], [45]–[47] have been used with and without tomographic reconstruction algorithms to quantify how gas properties vary in space and time. In the simplest form, this approach is performed to provide spatially resolved, path-integrated measurements of species and thermodynamic conditions. If absorption transitions with appropriate lower-state energy are used, path-averaged properties (e.g., absorbing-species column density, absorbing-species-weighted path-averaged temperature) can be obtained despite highly non-uniform conditions along the LOS [48]. For example, Goldenstein et al. [45] and Spearrin et al. [34] developed mid-infrared LAS sensors for absorbing-species-weighted path-averaged temperature and absorbing-species column density of H_2O, CO, and CO_2 in a model-scramjet combustor. The authors' mechanically scanned the LOS in two dimensions (x-y) to map out path-averaged gas properties. While effective and convenient to execute in environments with somewhat limited optical access, this approach can be time consuming (often requiring minutes per 2D dataset), provides modest spatial resolution (order 1-10 mm) and is not spatially resolved along the LOS.

Alternatively, numerous researchers have developed laser-absorption tomography (LAT) techniques to provide tomographic reconstruction of 2D temperature and species fields within the measurement plane [9], [41], [43], [46], [47], [49]–[53]. This approach provides the added

benefit of resolving the gas conditions along the line-of-sight; however, it comes at the expense of more complicated data processing routines and steep demands for many lines-of-sight (typically 10s to 1000s of LOS depending on the level of spatial resolution desired [49]). For these reasons, LAT techniques developed to date have primarily used near-infrared wavelengths to exploit relatively inexpensive telecommunication-grade fiber optics (e.g., fibers, multiplexers, splitters) and detectors [41], [43], [46], [47], [49], [50]. Unfortunately, confinement to the near infrared significantly limits the number of chemical species that can be monitored at combustion-relevant concentrations, conditions, and spatial scales. As such, the majority of prior LAT work in combustion applications has focused on detecting H_2O via its combination and overtone bands near 1.4 μm [41], [44], [46], [47]. Additionally, some work has been done to tomographically image hydrocarbons via their overtone C-H stretch absorption band near 1.7 μm [43] and NH_3 via its overtone and combination bands near 1.5 μm [54]. To overcome this limitation several researchers have developed LAT techniques employing mid-infrared wavelengths for tomographic imaging of temperature, CO, and CO_2 [9], [51]–[53], however these works have relied on mechanical scanning of the line-of-sight, thereby significantly limiting the temporal and spatial resolutions to the order of seconds to minutes and mm, respectively.

That being said, there remains a critical need to develop mid-infrared LAS and LAT techniques with higher temporal resolution and spatial resolution (e.g., less than 1 second and 1 mm, respectively). Recent work by Wei et al. [55] demonstrated significant progress towards achieving this goal through the use of laser-absorption imaging (LAI) with a high-speed mid-IR camera. The authors demonstrated the ability to acquire LAS measurements of temperature, CO, CO_2, and C_2H_6 along $\approx$400 lines-of-sight (in a single plane) simultaneously to provide 1D measurements and reconstructions of gas temperature and species concentrations. Diffraction-induced noise and image artifacts prevented use of the entire focal plane array and, thus, mechanical scanning of the measurement plane (in the axial direction) was required to achieve 2D measurements and reconstructions of flame structure. Using this technique the authors' were able to acquire LAS measurements with a spatial resolution of near 50 and 125 μm in the horizontal and vertical directions respectively, and a 2D image of flame properties was acquired in $<$ 10 seconds [55]. As a result, this approach

provided ≈ 10× smaller spatial resolution and ≈ 100× better temporal resolution compared to more conventional LAT techniques that rely on translating the LOS in both the x- and y-direction.

Here we present the development and application of the first mid-infrared laser-absorption imaging technique capable of providing 2D-measurements and -tomographic reconstruction of flame temperature and CO concentration without mechanical scanning of the measurement plane. This was achieved by performing high-speed, 2D imaging of scanned-wavelength, mid-infrared laser light that was reflected off two ground-glass diffusers spinning at 90,000 RPM prior to passing through the flame. Spinning the diffusers was required to break the optical coherence and, thus, prevent diffraction-induced image artifacts. This approach enabled the following advancements in mid-IR LAI: 1) a 8x increase in the number of simultaneous measurement paths (≈3,300 LOS here compared to 400 LOS in [55]) and 2) a ≈20x improvement in 2D-measurement time (0.1 seconds here compared to ≈2 seconds in [55]) by avoiding the need to mechanically scan the measurement plane. We demonstrate that this approach enables 2D measurements of thermochemical flame structure on near-cm scales with a projected pixel size of ≈ 140 μm and a time resolution as small as 0.1 seconds (i.e., 10 Hz). The remainder of this chapter is primarily devoted to presenting the design and evaluation of the optical setup and describing how this LAI technique was applied to provide 2D-measurements and -tomographic reconstruction of flame temperature and carbon monoxide concentration in flames.

4.2 Technical Approach and Equipment

Figure 4.1 illustrates the experimental setup used for LAI of temperature and CO in partially premixed, oxygen-ethylene flames. A continuous-wave (CW) quantum-cascade laser (QCL) providing 30 mW of optical power at wavelengths near 4.8 μm was used to provide 2D measurements of absorbance spectra. The wavelength of the laser was scanned across the P(0,20) and P(1,14) absorption transitions of CO near 2059.9 and 2060.3 cm^{-1}, respectively, at 50 Hz via injection-current tuning with a 700 mV peak-to-peak triangle wave. The QCL's current was scanned below its threshold current to enable the background and flame emission

to be measured in each pixel immediately before each scan. The wavelength scanning of the QCL was characterized using a solid germanium etalon with a free-spectral range of 0.0163 cm^{-1}. It is worth noting that the absorption transitions employed here have recently been used to measure gas temperature and CO in several other combustion environments (e.g., scramjet combustor [34], pulse-detonation engine [39], and propellant flames [6]). We refer the reader to [34] for additional details regarding why these absorption transitions are well suited for studying combustion gases.

A custom built optical assembly (see Fig. 4.1(a)) was used to expand the laser beam and break its coherence to prevent diffraction-induced image artifacts (see Section 4.3) that formed by passing coherent laser light through apertures in the beam-shaping optics and camera. The laser beam was immediately expanded by a 12.7 mm diameter AR-coated CaF_2 concave lens with a focal length of -18 mm. The expanded beam was then directed to a gold-coated, ground-glass diffuser (ThorLabs DG10-120-M01) with 120 grits/inch ($\approx$ 50 grit/cm). The gold coating provides $>$ 97% reflectance at an angle-of-incidence (AOI) of 12° for wavelengths near 4.8 μm. The diffuse reflection was then collimated by a 25.4 mm diameter AR-coated silicon lens with a focal length of 25.4 mm and the beam was

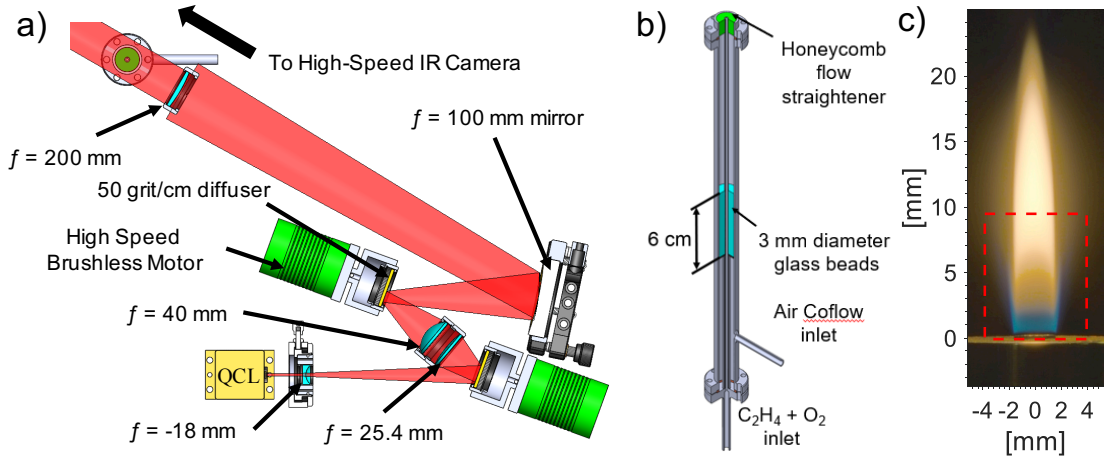

Figure 4.1. (a) Optical setup used to break the laser light's coherence and provide diffraction-free LAI, (b) coflow burner, and (c) HDR image of partially premixed ($\phi = 6.43$) oxygen-ethylene flame studied with LAI. The red dotted line indicates the approximate field of view of the LAI diagnostic.

then focused onto a second diffuser using a 25.4 mm diameter AR-coated CaF_2 lens with a focal length of 40 mm. The AOI for both of these diffusers was approximately 20°. When aligning the diffusers, the beam was directed to the outer edge of each diffuser to concentrate the beam onto regions of each diffuser with the highest velocity (while spinning), thereby providing more rapid scrambling of the laser light's coherence. After the second diffuser, the laser light was partially collimated by a 50.8 mm diameter concave mirror with a focal length of 100 mm. Close to the viewing plane, the beam was passed through a final 25.4 mm diameter lens (CaF_2, focal length of 200 mm) to collimate a portion of the beam which was directed through the flame and into the high-speed IR camera.

Both of the diffusers were mounted in 25.4 mm diameter lens tubes which were mounted to a custom aluminum adapter (using two set screws) in order to attach each diffuser to a motor (Castle Creations 1406 Sensored 4-Pole Brushless Motors, 7700kV). The motors were powered by Mamba X sensored motor controllers. The motors for the first and second diffusers were supplied with 26 V DC and 5 and 7 A of current, respectively. With the diffusers mounted to the motors, both motors were capable of spinning at 90,000 RPM (≈9400 rad/s). Due to the high angular velocity, care was taken to balance the diffuser assembly during machining and shim stock was used to properly seat the diffuser in the diffuser holder. Failure to properly balance the diffusers can cause extreme mechanical vibration which can misalign the optical setup or, at best, introduce unwanted noise and oscillations in the light intensity imaged by a given pixel.

The incoherent laser light was imaged by a Telops Fast-IR 2K high-speed infrared camera which employs a cryogenically cooled InSb focal-plane array with 320 x 256 pixels. At full resolution, the camera is capable of operating at nearly 2000 frames-per-second (FPS). However, during all LAI experiments the field of view was reduced to 64 x 52 pixels to enable frame rates of 24 kFPS to be used. This frame rate was required to sufficiently resolve the absorbance spectrum measured in each pixel when employing the scan rates and amplitudes used here. A bandpass filter centered near 2060 cm^{-1} with a full-width at half-maximum of 40 cm^{-1} was used to prevent pixel saturation from background flame emission which was pronounced in the high-temperature and sooting flame studied here.

Flames were produced by a custom-made coflow burner (see Fig. 4.1(b)). The outer body of the burner is made from a stainless-steel pipe (330 mm long, 19 mm outer diameter) with weld neck flanges on each end. A smaller tube (3.2 mm (1/8") outer diameter and 2.16 mm (0.085") inner diameter) concentric with the outer body of the burner carried a mixture of oxygen and ethylene to the flame. Streams of ethylene (0.045 L/min) and oxygen (0.072 L/in) were mixed ≈150 diameters upstream of the burner exit via a mixing T-junction that was connected to 1/4" diameter gas lines made of 316 stainless steel. A coflow of air entered the burner orthogonally through the main outer body 51 mm above the bottom flange. The air flowed through the annulus between the body wall and central tube and passed through a 6-cm deep bed of 3-mm diameter glass beads located 72 mm downstream of the coflow inlet. The coflow then passed through a 12.7 mm thick honeycomb flow straightener (0.88 mm cell size) at the exit plane to reduce the turbulence level and lateral velocity components. The exit of the fuel supply line is flush with the exit of the honeycomb flow straightener. To mitigate risk of flashback, the burner was first lit without coflow and without premixing to establish a pure-ethylene-air diffusion flame. Once the diffusion flame was established the flow rate of oxygen was gradually increased until the desired equivalence ratio was reached. The C_2H_4-O_2 jet exit velocity and jet Reynolds number were 0.8 m/s and 61.0, respectively. The coflow velocity was adjusted until the flame appeared steady, resulting in an approximate exit velocity and Reynolds number of 0.5 m/s and 331.6, respectively.

Figure 4.1(c) shows the partially premixed (ϕ=6.43) oxygen-ethylene flame studied here using LAI. The image shown in Fig. 4.1(c) was acquired using high dynamic range (HDR) imaging to highlight flame structure and avoid camera saturation. This was required due to the extreme luminosity (too bright to view without eye protection) of this flame. The HDR images were acquired using a Nikon D3200 camera with an AF-S Nikkor 18-55 mm lens. For each HDR image, 4 photos were taken with varying shutter speeds and then combined with Luminance HDR software to create the final image. The shutter speed for each image was chosen to be optimal for a unique region of the flame.

4.3 Motivation for Optical Design

Experiments were conducted without diffusers to illustrate the challenges associated with performing mid-IR LAI with coherent laser light. Without diffusers, pronounced Airy-disk patterns were observed in images of the QCL's laser beam (see Fig. 4.2(a)). These and other diffraction-induced patterns were altered by the presence of the flame and varied in time during scanned-wavelength experiments. For example, Fig. 4.2(b) illustrates the signal time history measured in a single pixel while scanning the wavelength and intensity of the QCL. Pronounced oscillations in signal intensity (analogous to optical fringes formed by conventional etalons) were found in pixels located in the vicinity of diffraction patterns. These oscillations severely complicate *in situ* determination of the non-absorbing light intensity (I_o). This leads to spatially dependent errors in the best-fit spectroscopic parameters (e.g., integrated absorbance) obtained from the spectral-fitting routine, which leads to spatially correlated errors in the measured gas conditions. For example, Fig. 4.2(c) shows a single image of the path-integrated temperature field (calculated from the two-color ratio of integrated absorbances) that is severely compromised by a clear Airy-disk pattern in the middle of the flame.

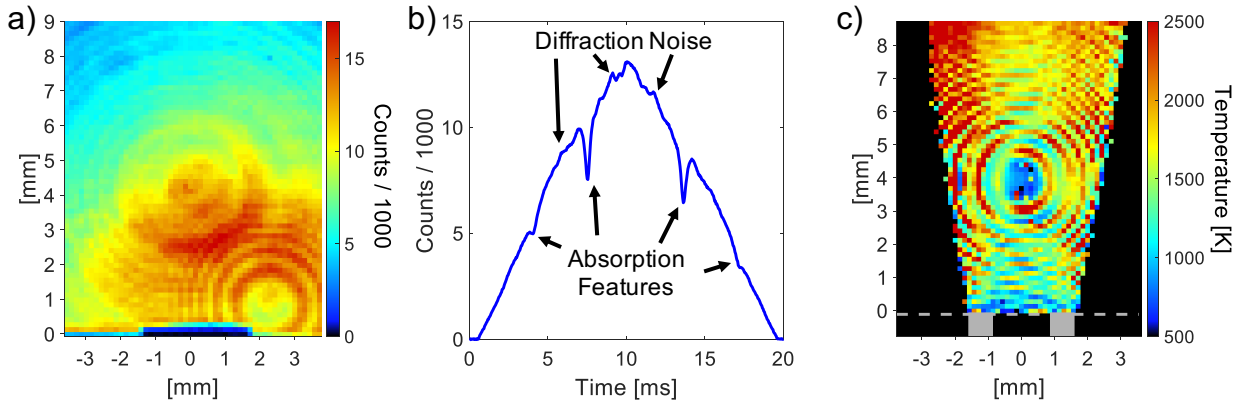

Figure 4.2. (a) Image of coherent laser light near 4.8 μm with Airy-disks. (b) Single-pixel time-history illustrating how diffraction-induced oscillations vary in time and wavelength space. (c) Image of oxygen-ethylene-flame temperature acquired using 2D LAI with coherent laser light which illustrates how diffraction patterns can compromise image quality.

One approach to avoiding these diffraction-induced image artifacts is to destroy the coherence in the laser light by reflecting the beam off spinning diffusers. This technique has been used in a variety of low-speed visible-imaging applications employing laser backlighting [56]–[58], most similarly, to perform low-speed (<30 frames per second) imaging of soot-volume-fraction in flames via 2D imaging of visible (632.8 nm) laser extinction [56]. However, implementing this strategy into a high-speed scanned-wavelength laser-absorption-spectroscopy technique has, to our knowledge, never been done previously and this presented several challenges. Most notably, high angular velocities (approaching 100,000 RPM) were needed to scramble the speckle pattern created by the diffusers (see Fig. 4.3(a) and 4.3(b)) and sufficiently homogenize the local light field on the timescale of the short camera integration times required here (order of 10 μs). For example, Fig. 4.3(c) compares single-pixel time histories measured during a scanned-wavelength experiment with stationary and spinning diffusers. When the diffusers are stationary the light field consists of a speckle pattern (see Fig. 4.3(a)) and large amplitude, temporally structured noise (see Fig. 4.3(c)) persists in each pixel (albeit with altered characteristics). The latter likely originates from wavelength-dependent optical interference. However, by spinning the diffusers the speckle pattern can be sufficiently homogenized on the timescale of the camera integration time (see Fig. 4.3(b)). This leads to the signal in each pixel consisting of relatively random (i.e., unstructured) and lower amplitude noise (see Fig. 4.3(c)) which is much less problematic for the spectroscopic fitting routine. It is worth noting that spinning both diffusers provides only a small gain in SNR compared to spinning a single diffuser. However, it was critical to reflect the light off two diffusers (e.g., 1 stationary, 1 spinning) to achieve an SNR sufficient for 2D LAI in the flames studied here. Fig. 4.3(d) illustrates that using a longer camera integration time (t_{int}) reduces the noise level. This is because it enables the time-varying speckle pattern to be averaged over a longer duration. The measurement of SNR vs integration time was least-squares fit to a power-law function of the form $SNR(t_{int}) = at_{int}^{b}$. The best-fit values of a and b were 4.82 and 0.51, respectively, and the coefficient of determination (i.e., R^2) was 0.999 indicating that the model captures the effect of integration time on SNR well. From this analysis, it is clear that using the highest motor speed and longest integration time possible for a given frame rate is desirable.

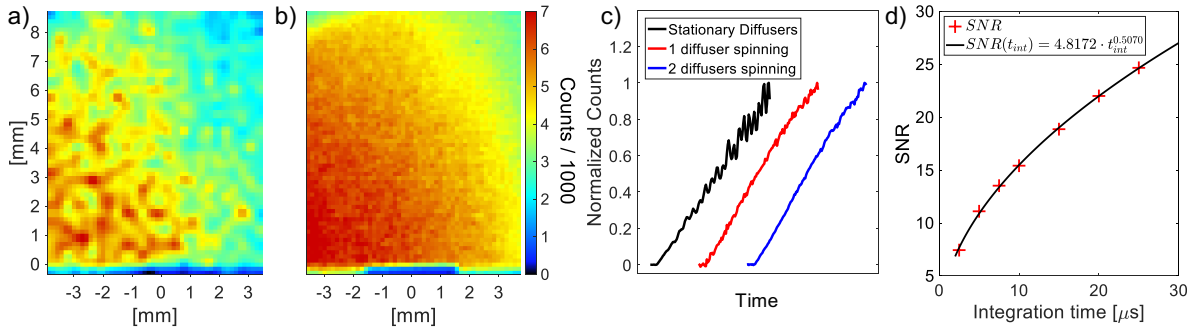

Figure 4.3. (a) Image of the speckle pattern created by reflecting the laser light off two stationary diffusers. (b) Image of laser beam profile with the diffusers rotating at 90,000 RPM which illustrates how spinning the diffusers homogenizes the speckle pattern. (c) 15-scan-averaged signal time-history measured by a single pixel for laser light reflected off two diffusers that are stationary or spinning at 90,000 RPM. (d) Scan-averaged SNR for a single scan as a function of camera integration time.

It is important to note that the results shown in Fig. 4.3 are dependent on the laser wavelength and diffuser grit size. Gold-coated ground-glass diffusers with 120, 220, and 1500 grits/inch were all tested. The diffusers with 120 grits/inch performed best (provided a diffuse beam and dense speckle pattern) when using laser light near 4.8 μm. Conversely, the diffusers with 1500 grits/inch performed best for laser light near 1.4 μm, but performed poorly (providing near-specular reflections with little speckling) for laser light near 4.8 μm.

4.3.1 Validation of LAI Diagnostic

The accuracy of the LAI diagnostic was validated by studying a non-reacting, isothermal, laminar jet of 49% CO, 49% Argon and 2% H_2 flowing into ambient air. The initial jet diameter was 2 mm and the exit velocity of the jet was 3.32 m/s, yielding a jet Reynolds number of 217.6. The spatial resolution of the LAI diagnostic was estimated by imaging a wire mesh backlit with the incoherent mid-infrared laser light (see Fig. 4.4). The known spacing between wires was used to determine that the projected pixel size was 140 μm. In all experiments the camera was focused onto the central axis of the jet (determined by imaging a wire mesh). The QCL was scanned across the P(0,20) transition at 50 Hz and the laser light was imaged at 24 kFPS with a resolution of 64 x 52 pixels. The QCL's current was

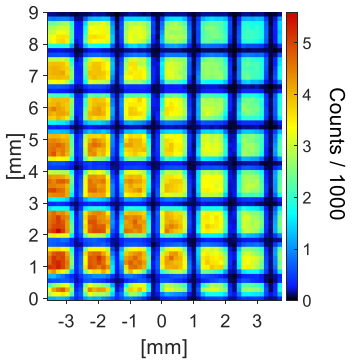

Figure 4.4. Image of wire mesh (wire diameter = 250 μm) backlit with incoherent laser light near 4.8 μm.

scanned below the threshold current to enable the background emission in each pixel to be measured. The measured background emission was subtracted from each pixel and the baseline incident light intensity was then determined for each pixel by least-squares fitting a 3rd-order polynomial to the non-absorbing regions of the intensity scan. The absorbance spectrum measured by each pixel (e.g., see Fig. 4.5(a)) was then calculated using Beer's law. A Voigt profile was least-squares fit to the measured absorbance spectrum in each pixel with the transition linecenter, integrated absorbance (i.e., integrated area) and collisional width as free parameters and the Doppler width fixed at the value corresponding to the known temperature (296 K). With the temperature and pressure known, the integrated absorbance corresponding to the best-fit Voigt profile was then used to calculate the mole fraction or column density of CO using Eq. (4.1).

$$A_{proj,j} = S_j(T) P \chi_{CO} L \tag{4.1}$$

Here $A_{proj,j}$ [cm^{-1}] is the integrated absorbance of transition j, $S_j(T)$ [cm^{-2}/atm] is the linestrength of transition j at temperature T, P [atm] is the pressure of the gas, χ_{CO} is the mole fraction of CO, and L [cm] is the path length through the absorbing gas. Figure 4.5(b) shows that the measured CO mole fraction in the jet core (calculated assuming a constant optical path length equal to the initial jet diameter) agrees within 3% of the known value (i.e., $\chi_{CO} = 0.49$) and the spatial standard deviation in the jet core is 3.1 % of the known

value. The image also reveals the expected structure of a laminar jet, with a near constant mole fraction in the core of the jet and increasing (in the axial direction) transport of CO into the boundary layer. Figure 4.5(c) illustrates how the measured column density of CO varies across the jet and how it compares to the value predicted assuming a constant χ_{CO} = 0.49 (i.e., no mixing) and the known initial jet geometry. At the jet exit, the measured profile of $\chi_{CO}L$ agrees exceptionally well with that predicted assuming constant χ_{CO} and similar agreement exists further downstream (y = 4 mm and 8.5 mm) in the middle of the jet (i.e., -0.75 mm $< r <$ 0.75 mm), thereby supporting the accuracy of this diagnostic. The 95% confidence interval (obtained from the spectral-fitting routine) of $\chi_{CO}L$ varied between 1% and 3% across the jet. The radial profiles indicate increasing transport of CO into the boundary layer and this likely results from a combination of diffusion and laboratory air currents, the latter of which introduced an obvious asymmetry in the jet profile on other occasions.

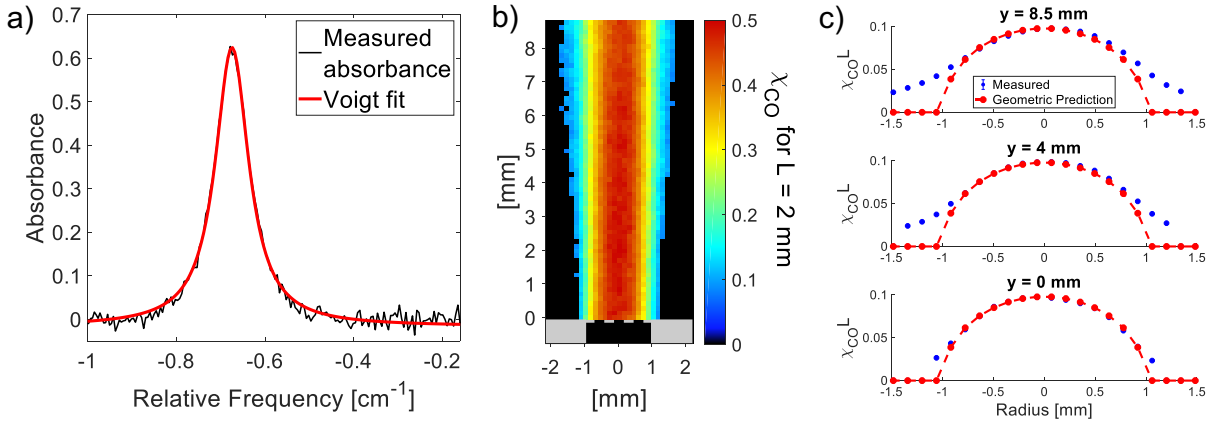

Figure 4.5. (a) 15-scan average of measured absorbance spectrum with best-fit Voigt profile acquired via LAI of a 2 mm diameter jet of CO/Ar/H_2 (0.49/0.49/0.02 by mole). (b) Corresponding 2D image of CO mole fraction (calculated assuming a constant absorbing path length of 2 mm). (c) Comparison between measured and predicted (for constant jet geometry and CO mole fraction) CO column density across the jet at various axial locations (error bars are too small to be seen).

4.3.2 Path-Integrated Measurements of 2D Flame Structure

2D LAI measurements of path-integrated temperature and CO column density were acquired in laminar, partially premixed, oxygen-ethylene flames. Figure 4.1(b) and 4.1(c) illustrate the burner and flame studied, respectively. The LAI measurements were acquired using a 64 x 52 pixel window with a frame rate of 24 kFPS and an integration time of 16.4 μs. Using this exposure time and a bandpass filter near 2060 cm^{-1}, the flame produced ≈12,000 counts of background emission, which was measured with the laser off before each scan and then subtracted from each pixel's time history prior to calculating the absorbance corresponding to each scan. Some slight instabilities in the flame were observed which introduced additional noise in the signal measured by each pixel. As a result, multiple scans were averaged together (after background subtraction) to further improve SNR. Figure 4.6(a) illustrates how averaging multiple scans together improves the SNR. Specifically, the scan-averaged SNR improves from 24.7 to 50.4 for 15- and 50-scan averages, respectively. Figure 4.6(b) shows the corresponding absorbance spectrum (15-scan average) measured by a single pixel imaging the middle of the flame. The absorbance spectrum exhibits a 1-σ absorbance

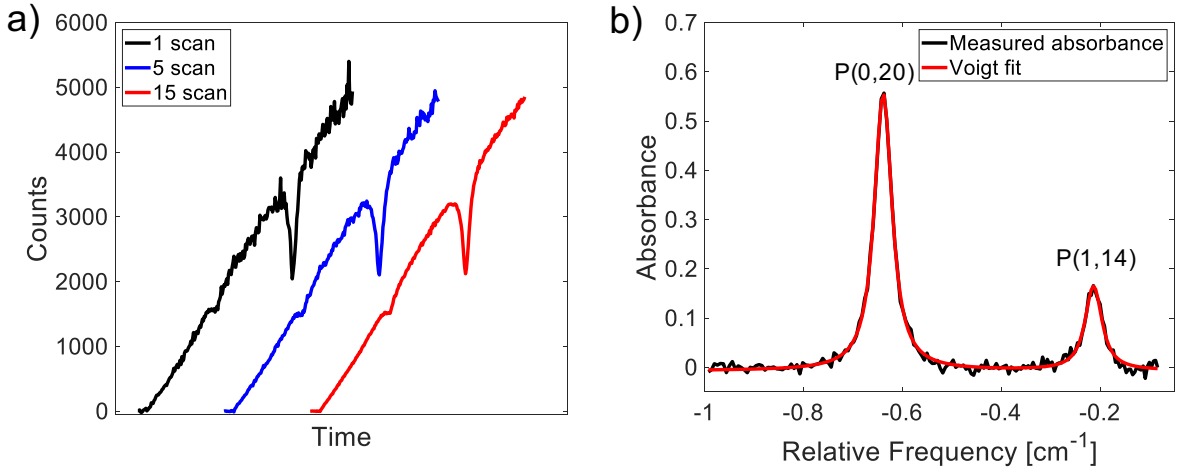

Figure 4.6. (a) Transmission spectrum with varying amounts of averaging measured by a single pixel and (b) measured and best-fit absorbance spectra of CO's P(0,20) and P(1,14) transitions. Measurements were acquired in a partially premixed, oxygen-ethylene flame with $\phi = 6.43$. The measurement location corresponds to the center of the field of view shown in Fig. 4.1(c).

noise level of 0.008. For each spectrum, the transition lineshapes were modeled by a Voigt profile and the best-fit spectrum was determined using a least-squares fitting routine with the transition linecenters, integrated absorbances, and collisional widths as free parameters. The Doppler width of each transition was fixed to the value given by the temperature determined from the two-color ratio of integrated absorbance, R (given by Eq. (4.2)), obtained from the previous iteration.

$$R = \frac{A_{proj,P(1,14)}}{A_{proj,P(0,20)}} \tag{4.2}$$

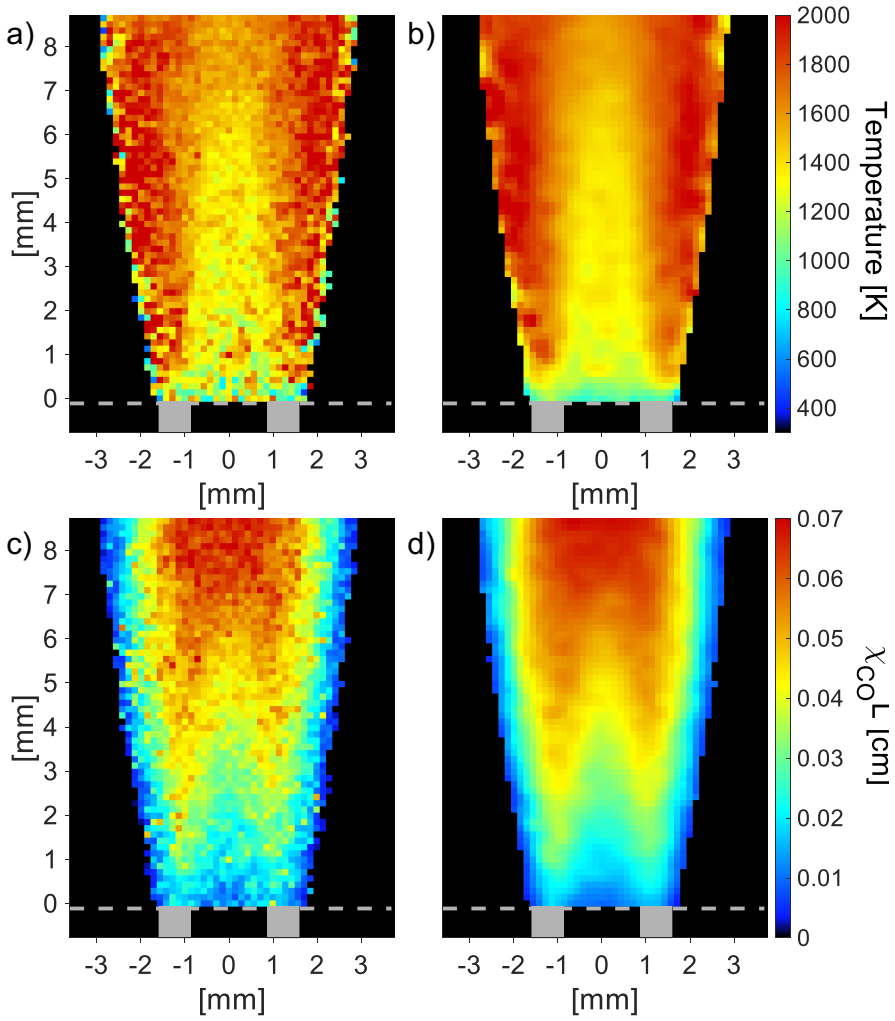

Figure 4.7. Images of path-integrated flame temperature (a,b) and CO column density (c,d) obtained via either a 15-scan (a,c) or 50-scan (b,d) average.

Here, $A_{proj,P(0,20)}$ and $A_{proj,P(1,14)}$ are the integrated absorbance of the P(0,20) and P(1,14) absorption transitions determined by the spectral-fitting routine. With R and spectroscopic constants known, the path-integrated temperature was determined using Eq. (4.3) [13]:

$$T = \frac{\frac{hc}{k_B}(E_2^{"} - E_1^{"})}{ln(R) + ln(\frac{S_2(T_o)}{S_1(T_o)}) + \frac{hc}{k_B}\frac{(E_2^{"}-E_1^{"})}{T_o}} \tag{4.3}$$

where h $[J \cdot s]$ is Planck's constant, c $[cm/s]$ is the speed of light, k_B $[J/K]$ is the Boltzmann constant, $E^{"}$ $[cm^{-1}]$ is the lower-state energy of a given transition (taken from the HITRAN2012 Database [59]), and T_o is the reference temperature (296 K). Here subscripts 1 and 2 refer to the P(1,14) and P(0,20) transitions, respectively.

With the pressure and path-integrated temperature known, the integrated absorbance of the P(0,20) transition was used to calculate the column density of CO ($\chi_{CO}L$) using Eq. (4.1) where the linestrength of the P(0,20) transition was evaluated at the measured path-integrated temperature using Eq. (4.4).

$$S_j(T) = S_j(T_o)\frac{Q(T_o)}{Q(T)}\frac{T_o}{T}\exp\left[-\frac{hcE_j}{k_B}\left(\frac{1}{T}-\frac{1}{T_o}\right)\right]\left[1-\exp\left(\frac{-hc\nu_o}{k_BT}\right)\right]\left[1-\exp\left(\frac{-hc\nu_o}{k_BT_o}\right)\right]^{-1} \tag{4.4}$$

Here, ν_o is the transition linecenter frequency $[cm^{-1}]$. It should be noted that this approach is strictly valid in the limit that the linestrength of each transition exhibits a linear dependence on temperature across the range of temperatures that exist along the line-of-sight [48].

Figures 4.7(a) and 4.7(b) show images of path-integrated flame temperature for a 15- and 50-scan average, respectively, and Figures 4.7(c) and 4.7(d) show images of CO column density for a 15- and 50-scan average, respectively. The spectral-fitting routine was performed in all pixels where the peak absorbance on the P(0,20) transition was greater than 0.05, thereby ignoring pixels with an absorbance SNR lower than 6.25. The images illustrate that 2D LAI is capable of resolving the thermochemical structure of laboratory scale laminar flames. The images reveal that the temperature is lowest in the fuel-rich core near the burner exit and increases in both the radial and axial directions, and peaks near the boundary with the air coflow. These observations are consistent with the expected structure of a laminar

diffusion flame. The image of CO column density is more difficult to interpret given that the flame diameter increases in the flow direction. Regardless, these images illustrate that, in general, the amount of CO present along a given line-of-sight increases in the flow direction. All of the images indicate that the flame is approximately axisymmetric, thereby enabling a tomographic reconstruction to be performed to provide greater detail regarding the 2D flame structure.

4.4 Tomographic Reconstruction of 2D Flame Structure

Figure 4.8 shows tomographic reconstructions of gas temperature and CO mole fraction in the flame's radial plane for a 5-scan (Fig. 4.8(a) and 4.8(c)) and 50-scan (Fig. 4.8(b) and 4.8(d)) average. Radial profiles of temperature and CO mole fraction are shown in Fig. 4.8(e) at select axial locations to further illustrate the thermochemical flame structure. These results were obtained by applying the tomographic reconstruction algorithms developed by Daun et al.[60] to the path-integrated measurements of integrated absorbance obtained via LAI. These alogrithms have previously been applied to numerous flame studies [9], [49], [55]. The results shown in Fig. 4.8 more clearly reveal the flame structure (compared to path-integrated results) and illustrate temperature and species profiles that are consistent with that expected in a fuel rich, partially premixed flame. The temperature is lowest in the core of the flame and, in general, increases in both the axial and radial directions. In comparison to the images of path-integrated temperature, the tomographic reconstruction reveals that the temperature rise in the axial direction within the flame core is more modest, increasing from 740 K to 1320 K between 1 mm and 9 mm above the burner exit, respectively. The temperature is highest (reaching a maximum near 2200 K) near the boundary between the fuel-rich C_2H_4/O_2 stream and air coflow where oxygen supplied by the coflow can reach the unburnt fuel and intermediate species. The reconstructions illustrate that very little CO is present near the burner exit and that the mole fraction of CO increases significantly in both the axial and radial directions before falling off in the boundary layer.

The remainder of this section is devoted to describing the pertinent details of the tomographic reconstructions. Tomographic reconstructions were performed assuming each pixel

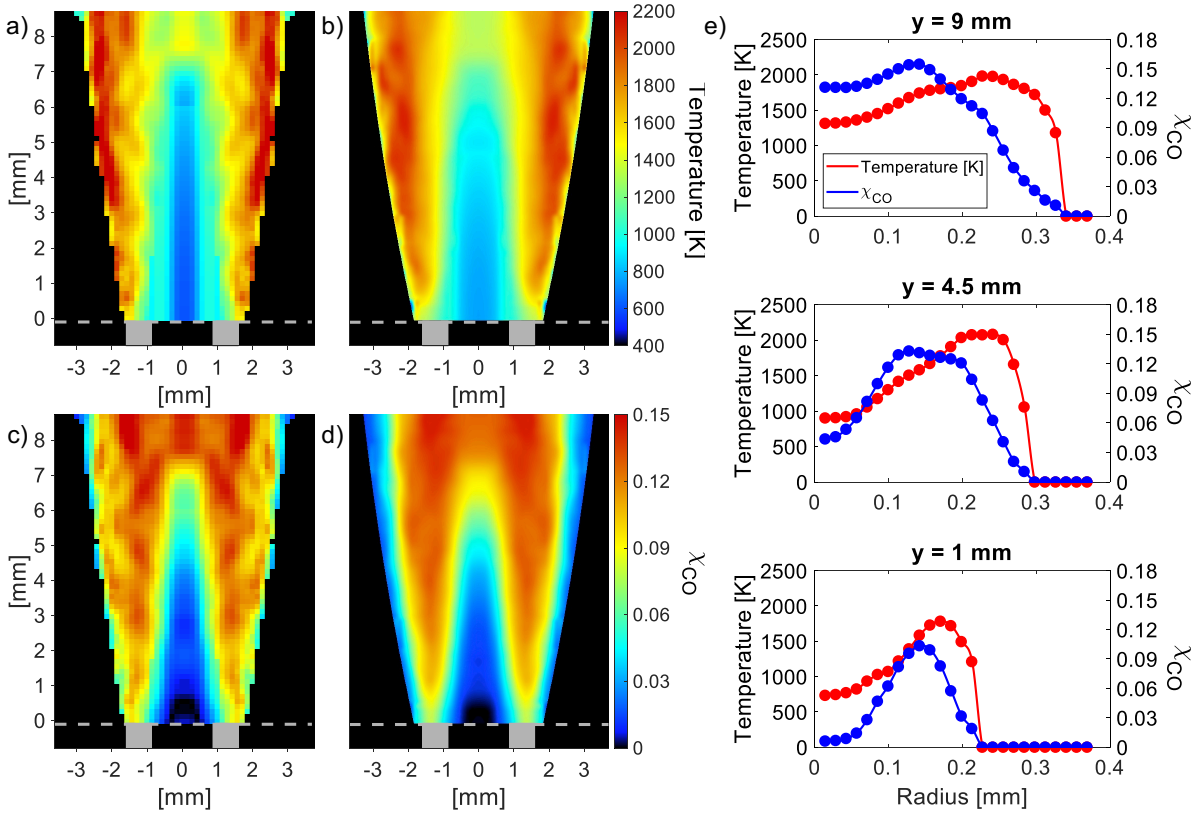

Figure 4.8. Tomographic reconstructions of flame temperature (a,b) and CO mole fraction (c,d) within the flame's radial plane using either a 5-scan/10 Hz average (a,c) or a 50-scan/1 Hz average (b,d). The images shown in (b) and (d) have been enhanced by 10x via cubic-spline interpolation to highlight image quality. (e) Radial profiles of temperature and CO mole fraction at axial locations of $y = 1$, 4.5 and 9 mm for the reconstructions obtained from a 50-scan average with (denoted by lines) and without (denoted by dots) a 10x enhancement in image resolution.

images a unique line-of-sight. Flame-induced beam steering could cause this assumption to break down and ultimately reduce the spatial resolution of the diagnostic. Since tomographic reconstruction is sensitive to noise in the input image, a 2×2-pixel average was applied to all images prior to averaging 5, or 50 measured spectra together (i.e., prior to performing time averaging). This significantly reduced the noise induced by beam steering and the rotating diffusers. Next, the absorbance spectra were processed using a two-line Voigt fit, as described previously, to determine the integrated absorbance (A_{proj}) of the P(0,20) and

P(1,14) absorption transitions corresponding to each pixel. The tomographic reconstruction algorithm employed here relies on assuming that the flame is axisymmetric. As a result, A_{proj} only needs to be resolved along the flame radius. Since A_{proj} was measured here along both halves of the flame, the results for each half were simply averaged together, however it should be noted that this has a small effect on image quality (see Fig. 4.9). The image (i.e., matrix) of each transition's integrated absorbance was then passed to the tomographic reconstruction algorithm as described next.

The tomographic reconstruction algorithm requires the assumption that the flame can be divided into N concentric rings of thickness Δr with a homogeneously distributed field variable, k, which is given by Eq. (4.5) for a specific absorption transition.

$$k = S_j(T)P\chi_{CO} \tag{4.5}$$

k effectively represents the local integrated absorbance per unit path length and the integral of k along a line-of-sight represents the back-projected data (i.e., the measured integrated absorbance: A_{proj}). N is given by the number of pixels that resolve the flame radius and Δr is given by the projected pixel size.

First, a process called onion-peeling deconvolution is used to generate a set of equations of the form $Ax = b$. Here, A is the coefficient matrix which contains the path length of light through each annular section (i.e., the absorbing path length of the line-of-sight imaged by a given pixel) and is given by Eq. (4.6), x contains the to-be-solved-for field variable (k), and b contains the back-projected data (i.e., the integrated absorbance, A_{proj}, measured by each pixel).

$$A_{ij} = \begin{cases} 0, & j < i \\ 2\Delta r[(j+1/2)^2 - i^2]^{1/2}, & j = i \\ 2\Delta r[(j+1/2)^2 - i^2]^{1/2} - [(j-1/2)^2 - i^2]^{1/2}, & j > i \end{cases} \tag{4.6}$$

Solving this system with back substitution may return a solution that is sensitive to noise in the back-projected data which manifests as errors or noise in the reconstruction of k. This is because onion-peeling deconvolution yields an ill-conditioned coefficient matrix which

makes it difficult to find a well defined global minimum [60]. To overcome this, Tikhonov regularization is employed to increase the condition of the matrix [60]. In doing so, the equations shown below are used to provide a more robust solution.

$$A_{Tik}\tilde{k}^* = b_{Tik} \tag{4.7}$$

where

$$A_{Tik} = (A^T A + \alpha_0 A L_0^T L_0) \tag{4.8}$$

and

$$b_{Tik} = A^T b \tag{4.9}$$

Here, $\tilde{k}^*$ is the field variable that yields the global minimum residual after Tikhonov regularization (i.e., the solution that is ultimately used to calculate images of gas properties). For the zeroth order regularization used for the data presented in this chapter, L_0 is given by the $N \times N$ matrix shown in Eq. (4.10).

$$L_0 = \begin{bmatrix} 1 & -1 & 0 & \cdots & 0 \\ 0 & 1 & -1 & \ddots & \vdots \\ \vdots & \ddots & \ddots & \ddots & \vdots \\ 0 & \cdots & & 1 & -1 \\ 0 & \cdots & & 0 & 1 \end{bmatrix} \tag{4.10}$$

The parameter α_0 is called the regularization parameter and it controls the balance between solution accuracy and smoothness/stability [60]. This works by approximating solutions to the ill-conditioned set of equations with those of a similar well-conditioned set. A high value of α_0 will return a solution which is smooth, but less faithful to the original problem, and lower values return high-fidelity but often oscillatory solutions. As $\alpha_0 \to 0$, $\tilde{k}^* \to k^*$ where k^* is the field variable that yields the true minimum residual. Although methods exist for

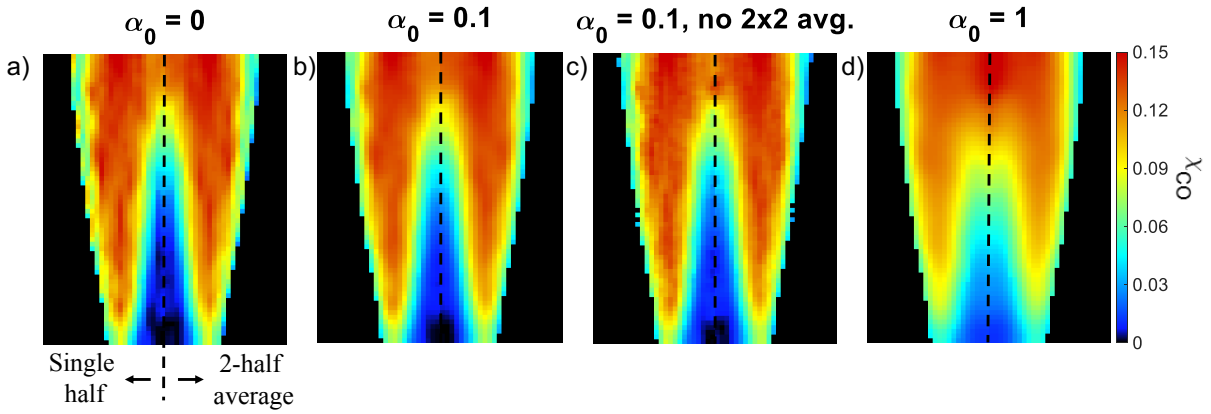

Figure 4.9. Reconstruction of χ_{CO} in the flame's radial plane for varying amounts of regularization: (a) $\alpha_0 = 0$, (b) $\alpha_0 = 0.1$, (c) $\alpha_0 = 0.1$ without 2x2 pixel-averaging, and (d) $\alpha_0 = 1$. Each image also compares how averaging both halves of the image together (prior to reconstruction) slightly improves final image quality, but does not significantly alter the observed structure.

determining an optimum value for α_0 [61], the value is often chosen at the user's discretion to obtain an acceptable balance of accuracy and smoothness [60]. Figure 4.9 illustrates how increasing α_0 from 0 to 1 improves image quality but reduces spatial resolution. In addition, Fig. 4.9 also illustrates how averaging both halves of the absorbance data together (prior to reconstruction) and using a 2x2 pixel average both slightly improve image quality without significantly altering the final images of χ_{CO}. The images presented in Fig. 4.8 were obtained using $\alpha_0 = 0.1$ since this produced solutions with acceptable stability while preserving the vast majority of flame structure that was revealed using $\alpha_0 = 0$.

The solution for each individual transverse plane (i.e., row of pixels) was stable, however differences between adjacent planes gave the final 2D images a somewhat noisy appearance. This noise was attenuated by applying a 6-point moving average filter along the axial direction of the 2D images of $\tilde{k}^*$ for each absorption transition. Figure 4.10 illustrates the row-to-row oscillations in $\tilde{k}^*$ for both absorption transitions near the flame's central axis and how the 6-point moving average is effective at removing the oscillations while preserving flame structure.

After reconstructing the 2D image of $\tilde{k}^*$ for each absorption transition, the two-color ratio of $\tilde{k}^*$, $R_{\tilde{k}^*}$, was calculated using Eq. (4.11).

$$R_{\tilde{k}^*} = \frac{\tilde{k}^*_{P(1,14)}}{\tilde{k}^*_{P(0,20)}} \tag{4.11}$$

The final 2D image of temperature was obtained by replacing R with $R_{\tilde{k}^*}$ in Eq. (4.3). Next, the 2D image of χ_{CO} was obtained using Eq. (4.5) with k replaced by $\tilde{k}^*_{P(0,20)}$ and using the 2D image of temperature to calculate the corresponding image of the P(0,20) transition's linestrength.

The SNR of the measured absorbance for the P(1,14) transition is low in the center of the flame near the exit of the burner since the gas is relatively cool and little CO is present there. This prevented a reliable reconstruction of the 2D temperature field in a 1.7 mm wide region located 0 to 3 mm above the burner exit. As a result, 224 pixels of the temperature data in this region were replaced with values extrapolated from a 2nd-order polynomial which was obtained via least-squares fitting to the remainder of the data set. A total of 224, or 6.7% of the temperature image presents a value that was obtained via extrapolation.

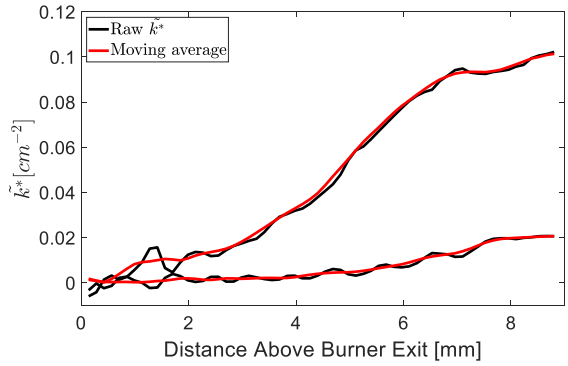

Figure 4.10. Values of $\tilde{k}^*_{P(0,20)}$ and $\tilde{k}^*_{P(1,14)}$ along the flame's central axis and corresponding 6-point moving average used to smooth plane-to-plane oscillations in the reconstructions shown in Fig. 4.8(b) and 4.8(d).

4.5 Conclusions

This work has demonstrated, for the first time, that mid-infrared LAI is capable of providing 2D measurements and tomographic reconstructions of flame temperature and carbon monoxide in axisymmetric flames without mechanical translation of the line-of-sight. This was achieved by reflecting scanned-wavelength laser light off two ground-glass diffusers spinning at 90,000 RPM prior to the light traversing the flame. This was done to break the coherence in the laser light and, therefore, prevent the formation of diffraction-induced image artifacts which have limited previously developed LAI techniques to 1D (simultaneously) imaging. Ultimately this approach enabled measurements of CO's absorbance spectra to be acquired at 50 Hz across ≈3,300 lines-of-sight simultaneously. While additional time averaging of spectra was done to improve the final image quality, this work demonstrated that this technique can provide high-fidelity 2D measurements and tomographic reconstructions of temperature and CO mole fraction on near-cm scales with a projected pixel size of 140 μm and a time resolution of 0.1 to 1 seconds. In comparison to conventional mid-IR LAT techniques employing mechanical translation of the line-of-sight, this technique offers a reduction in data collection time of ≈1,000× and potential for a ≈10× gain in spatial resolution compared to LAT methods that are limited by the laser beam diameter. In short, the capabilities of this 2D mid-IR LAI technique represent a significant step towards achieving high-speed, high-resolution measurements of thermochemical flame structure via LAT.

5. ULTRAFAST-LASER-ABSORPTION SPECTROSCOPY

5.1 Development and Initial Application of ULAS

The contents of this section are reprinted from [62] with permission, © The Optical Society.

5.1.1 Introduction

LAS diagnostics often employ narrowband, wavelength-tunable lasers (e.g., tunable diode lasers, quantum-cascade lasers) which are capable of measuring gas conditions via spectra measured over several cm^{-1} at rates up to 1 MHz [1], [63]. While highly useful, the narrowband nature of this approach can: 1) limit the dynamic range of such diagnostics [64], 2) complicate measurements of molecules with broad spectra (e.g., at high pressures), and 3) often prevents multi-species measurements using a single light source. To address these issues, numerous researchers have developed broadband LAS diagnostics, typically with 10s to 1000s of cm^{-1} of spectral bandwidth [65]–[72].

One common broadband LAS technique employs scanned-wavelength lasers with broad wavelength-tuning capabilities. For example, Sanders et al. [65] used a vertical-cavity surface-emitting laser (VCSEL) to scan ≈30 cm^{-1} near 760 nm in order to acquire measurements of temperature and O_2 at 500 Hz in high-pressure gases. More recently, a MEMS-VCSEL capable of tuning ≈170 cm^{-1} near 1.4 μm has been used to measure temperature and H_2O at 100 kHz in a wide variety of combustion applications (see [66] and references therein). In addition, external-cavity quantum-cascade lasers in the mid- and far-IR with large-amplitude tuning (≈100 cm^{-1}) have emerged, which recently enabled measurements of C_2H_4 between 8.5 and 11.7 μm in shock-heated gases with a time resolution of 3 ms [67]. Unfortunately, light sources suitable for this approach are limited to only a few wavelength

regions and the time-resolution is limited to the reciprocal of the scan frequency (typically on the order of 1 ms to 10 μs).

The broad spectral bandwidth of supercontinuum lasers has been utilized to acquire supercontinuum laser-absorption spectroscopy (SCLAS) measurements of temperature and species. For example, Sanders [68] used a femtosecond-fiber-laser-pumped supercontinuum source and a scanning bandpass filter to produce 1000 cm^{-1} of bandwidth near 1450 nm for measurements of temperature and several species (H_2O, CO_2, C_2H_2, C_2H_6O) at 50 kHz. Blume and Wagner [69] used a commercial supercontinuum light source with a dispersing fiber to acquire measurements of CH_4 and temperature at 200 Hz using 110 cm^{-1} of bandwidth near 1650 nm. More recently, a supercontinuum absorption spectrometer was utilized by Werblinski et al. to acquire temperature, pressure, and H_2O measurements at a rate of 10 kHz in a fired internal combustion engine [73]. Measurements utilized 100 nm of bandwidth near 1400 nm. SCLAS measurements have also been acquired at mid-infrared wavelengths, such as those by Cezard et al. [74]. A mid-infrared supercontinuum fiber laser source was used to generate a supercontinuum spanning from 2-3.5 μm, and used to acquire measurements of absorption spectra of multiple species. This diagnostic has not yet been applied to characterize combustion environments. One drawback to SCLAS is the relatively large noise levels inherent to supercontinuum light sources which necessitates averaging of 100s of spectra, thus, limiting the measurement time resolution.

Numerous techniques employing ultrafast lasers (i.e., lasers emitting ultrashort, typically $<$ 10 ps, pulses) have also been used for broadband LAS measurements of combustion gases, however they have not been applied in the mid-infrared. Recently, Draper et al. [71] applied a dual-frequency-comb spectrometer to characterize combustion environments. The authors used 160 cm^{-1} of bandwidth near 1655 nm to measure temperature and CH_4 concentration in a rapid compression machine. Currently, multi-shot averaging and filtering have extended the repetition rate to $\approx$1.4 kHz [71]. Most recently, time-resolved, optically gated absorption (TOGA) spectroscopy was developed by Stauffer et al. [72] to provide background-free measurements of absorption spectra. The authors used an amplified Ti:Sapphire laser and two frequency-doubling processes to produce 100-fs pulses centered near 310 nm with over 300 cm^{-1} of bandwidth to acquire spectra of OH.

Demonstrated in this chapter is the first, to my knowledge, ultrafast, single-shot, mid-infrared LAS diagnostic for temperature and species measurements in combustion gases. In addition to the aforementioned potential advantages of broadband LAS diagnostics (e.g., improved high-pressure capability, high-dynamic range, multi-species measurements), we demonstrate that this diagnostic offers several unique advantages: 1) ultrafast (<1 ns) time resolution, 2) access to strong fundamental absorption bands located throughout the mid-wave infrared (2 to 5.5 μm) using a single light source and camera, and 3) potential for single-shot, spatially resolved (1D) thermometry and species measurements at 5 kHz. This chapter describes the design and operating principles of this diagnostic technique, in addition to its initial validation and application to characterizing flames. Specifically, single-shot, 5 kHz measurements of temperature and CO were acquired in a laser-ignited HMX flame using wavelengths near 4.9 μm, and measurements of temperature and CH_4 were acquired in a partially premixed CH_4-air Hencken-burner flame using wavelengths near 3.3 μm. The results demonstrate that this diagnostic is capable of providing high-precision measurements of temperature (<1%) and molecular species (<2.5%) in combustion gases with ultrafast (< 1 ns) time resolution.

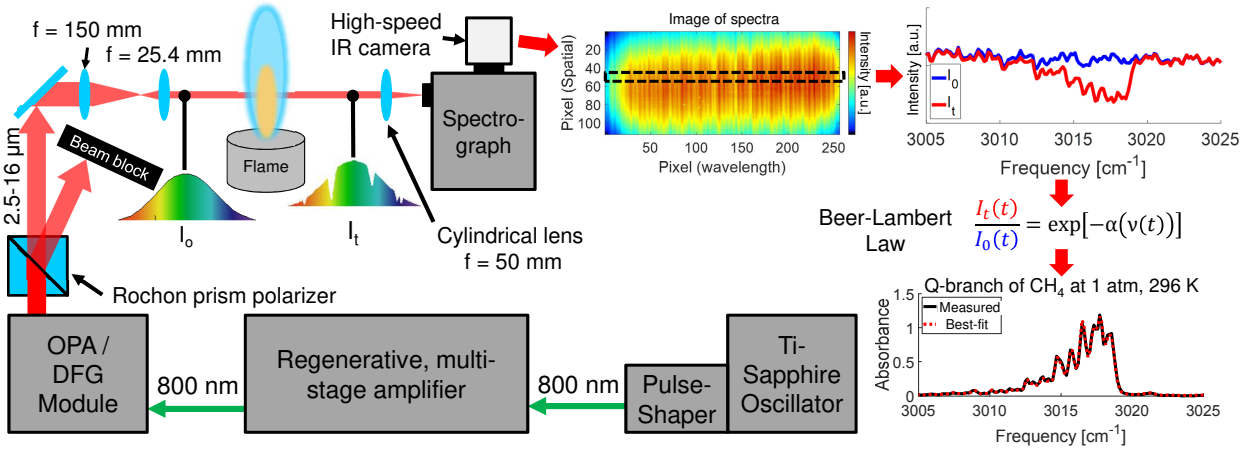

Figure 5.1. Concept schematic illustrating the experimental setup and data processing procedure employed by the ultrafast-laser-absorption diagnostic.

5.1.2 Experimental Setup

The experimental system and data processing procedures are summarized in Fig. 5.1. Ultrafast laser pulses were generated by a mode-locked Ti:Sapphire laser (Coherent Mantis) at a rate of 80 MHz and a center wavelength near 800 nm. The pulses were tailored by a Femtojock pulse-shaper to prepare them for amplification by a multi-stage regenerative chirped-pulse amplifier (Coherent Legend Elite Duo). The amplifier produced pulses with a pulse energy of 2 mJ and duration of 55 fs at a repetition rate of 5 kHz. Next, the pulses were directed into an optical parametric amplifier (OPA) module (Coherent OPerA Solo) equipped with non-collinear difference-frequency generation (NDFG) crystals to generate ultrashort mid-IR pulses. The mid-IR pulses contain ≈600 cm^{-1} of useful spectral bandwidth and the center wavelength can be tuned between 2.5 and 18 μm via computer controlled manipulation of the crystals. For the results presented here, the pulse energies were 30 μJ and 4 μJ for

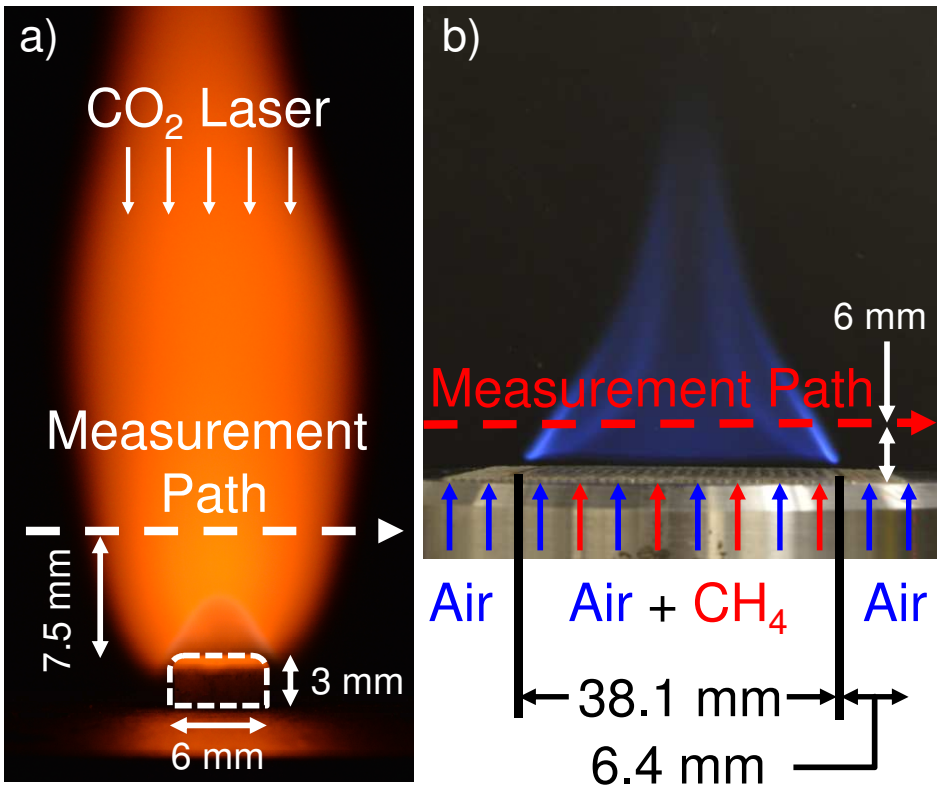

Figure 5.2. Images of and pertinent dimensions for the a) laser-ignited HMX flame and b) partially premixed CH_4-air flame studied here.

wavelengths near 3315 nm and 4858 nm, respectively. A MgF_2 Rochon prism polarizer was used to attenuate the pulse energy to ≈0.75 μJ to prevent camera saturation. The ordinary ray was used for absorption measurements and the extraordinary ray was directed to a beam dump. Next, the mid-IR pulses were directed through the test gas and then focused onto the slit of an Andor Shamrock 500i imaging spectrometer using a cylindrical lens (ZnSe, 50 mm focal length). A 300 groove/mm diffraction grating was used to spectrally disperse the pulses and a Telops FAST-IR 2K high-speed IR camera was used to image each individual pulse in 2D. This configuration provided a theoretical spectral resolution and bandwidth of 0.21 nm and 38 nm, respectively, and similar metrics were achieved in practice. The IR camera recorded 52×256 pixels with a 5 μs exposure time at 10k frames-per-second in order to record two images per pulse (one for the pulse, another to image flame and ambient emission between pulses so it could be subtracted off in post-processing). The camera was synchronized with the laser output.

CO and CH_4 were chosen for the initial application of this diagnostic primarily to demonstrate its ability to measure gas properties via molecules with well isolated lines (CO) or blended spectra (CH_4). Measurements were acquired in CO's P-branch near 2060 cm^{-1} due to favorable absorbance levels, lack of interference from other combustion relevant species (e.g., H_2O, CO_2), and previous combustion studies demonstrating the utility of this spectral region [6], [7], [75], [76]. Temperature and CH_4 measurements were acquired via CH_4's Q-branch near 3015 cm^{-1} due to its strength, isolation from interfering absorption lines, and the large number of transitions with unique lower-state energy comprising it which enhances temperature sensitivity [1], [64].

The center wavelength of the spectrograph and light source were set to 4858 nm for measurements of temperature and CO concentration. Measurements were acquired in a static-gas cell [12] (9.4 cm path length) filled with a commercially prepared gas mixture (2% CO, 1.8% CO_2 and 96.2% N_2 by mole) at 1 atm and 296 K to validate the accuracy of the diagnostic and data processing routine. Measurements of temperature and CO column density ($\chi_{CO}L$) were also acquired in a laser-ignited HMX flame (see Figure 5.2a). The HMX was pressed into a 6 mm diameter, 3 mm tall cylindrical pellet and ignited with a CO_2 laser emitting 78 W/cm^2 at a wavelength of 10.6 μm for the entire test duration. For

this test, the $1/e^2$ diameter of the ultrafast beam was reduced from 7.9 mm to 1.4 mm via a lens telescope consisting of a CaF_2 plano-convex lens (f=150 mm) and an AR-coated Si plano-convex lens (f=25.4 mm). The measurement was acquired 7.5 mm above the initial surface location of the pellet.

The accuracy of the temperature and CH_4 diagnostic was also validated via measurements in a static-gas cell (0.7 cm path length) and Figure 5.1 illustrates an example single-shot measurement of CH_4's Q-branch at 296 K and 1 atm. The cell was filled with a commercially prepared mixture of 7% CH_4, 15% C_2H_2 and 78% N_2 by mole at 1 atm and 296 K. Measurements were also acquired in a laminar, partially-premixed CH_4-air flame (see Figure 5.2b). The flame was produced by a Hencken burner with a 38.1 mm square core consisting of a honeycomb of alternating jets of CH_4 and air surrounded by a 6.4 mm thick co-flow of air. The equivalence ratio was 6.4 with an exit plane velocity of ≈0.9 cm/s.

5.1.3 Data Processing

For each experiment, the measured spectral absorbance (α) was calculated at each frequency (ν) using the measured incident (I_o) and transmitted (I_t) laser intensity and Beer's Law: $\alpha(\nu) = -ln[I_t(\nu)/I_o(\nu)]$. I_o was obtained empirically by recording and averaging (to reduce noise) 200 images of ultrashort mid-IR pulses in the absence of the test gas. The signal-to-noise ratio (SNR) of I_o was then further increased by averaging 8 to 18 (depending on test) spectra of I_o (acquired by adjacent rows of pixels within a single image) together. For the results reported here, this corresponds to spatial averaging across less than 1 mm (vertically) at the measurement location in the flame gas.

The gas temperature and absorbing-species concentration were determined by least-squares fitting a simulated absorbance spectra to the measured absorbance spectra. The fitting routine employs the following free parameters: temperature, absorbing species concentration, the linecenter frequencies for several prominent spectral lines, the width of the empirical instrument response function (IRF), and a scaling factor for I_o to account for shot-to-shot fluctuations in pulse energy. The frequency axis of the data was determined by matching 3 to 4 prominent absorption features to their linecenter frequencies (floated in the

fitting routine) and fitting a linear frequency axis to those points. Absorbance spectra were simulated in the fitting routine using the following procedure: 1) A high-resolution (≈0.0005 cm^{-1}) absorbance spectrum was simulated using Eq. 5.1.

$$\alpha_{HR}(\nu) = \sum_j S_j(T)\phi_j(\nu)P\chi L \tag{5.1}$$

where S_j and ϕ_j are the linestrength and lineshape of transition j, respectively, T is the gas temperature, P is the gas pressure, χ is the absorbing species mole fraction and L is the path length through the absorbing gas. The transition linestrengths at a given temperature were calculated using Eq. 5.2.

$$S_{\mathrm{j}}(T) = S_{\mathrm{j}}(T_o)\frac{Q(T_o)}{Q(T)}\frac{T_o}{T}\exp\left[-\frac{hcE_{\mathrm{j}}}{k_B}\left(\frac{1}{T}-\frac{1}{T_o}\right)\right]\left[1-\exp\left(\frac{-hc\nu_o}{k_BT}\right)\right]\left[1-\exp\left(\frac{-hc\nu_o}{k_BT_o}\right)\right]^{-1} \tag{5.2}$$

Transition lineshapes were modeled as a Voigt profile. 2) The resolution of the empirical baseline (i.e., I_0) was increased to match that of α_{HR} via linear interpolation, thereby yielding $I_{o,HR}$. 3) Next, Eq. 5.3 was used to produce a high-resolution, semi-empirical transmission spectrum ($I_{t,HR,conv}$), which has been convolved with the IRF of the spectrograph-camera setup. 4) $I_{o,HR}$ was then convolved with the IRF to yield $I_{o,HR,conv}$. 5) A simulated absorbance spectrum with the IRF accounted for was then calculated from $I_{o,HR,conv}$ and $I_{t,HR,conv}$ using Beer's Law and then downsampled to the same frequency axis as the measured absorbance spectrum to enable direct comparison and the sum-of-squared error (the optimization parameter) to be computed by the fitting routine.

$$I_{t,HR,conv}(\lambda) = \int_{-\infty}^{\infty} IRF(\lambda-\tau)I_{o,HR}(\tau)\mathrm{e}^{-\alpha_{HR}(T,P,\chi,L)}d\tau \tag{5.3}$$

Here, λ is the wavelength and τ is the convolution shift variable. The IRF was modeled as a Lorentzian lineshape.

It is important to note that the IRF is not directly convolved with the simulated absorbance spectrum because the spectrograph-camera setup "sees" a transmission spectrum, not an absorbance spectrum. The convolution with the IRF was executed in wavelength-

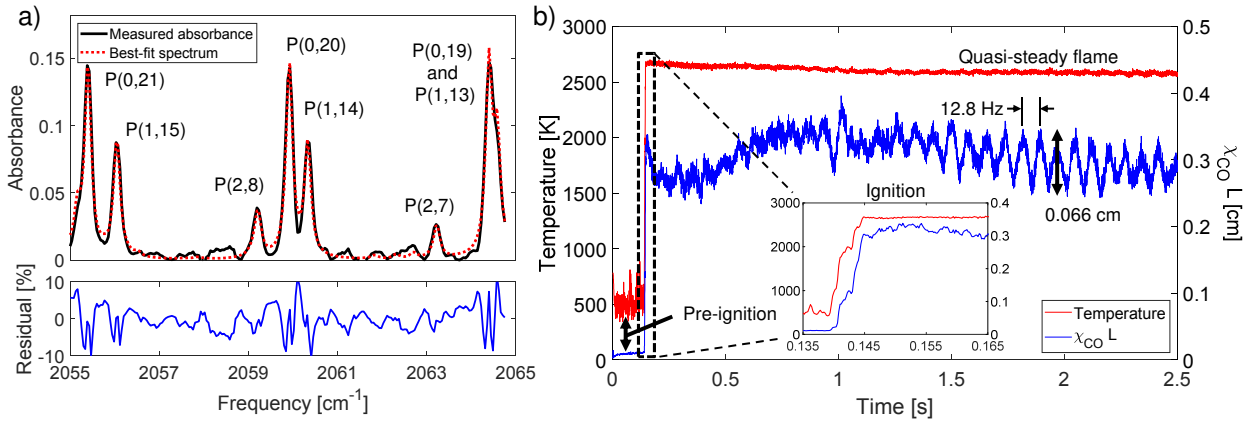

Figure 5.3. Example single-shot measurement and best-fit spectrum for CO near 4.9 μm (a) and corresponding time history of temperature and $\chi_{CO}L$ acquired in a laser-ignited HMX flame (b).

space where the full-width at half maximum (FWHM) of the IRF is constant. The spectroscopic model for CO employed the HITEMP 2019 database [77] and the spectroscopic model for CH_4 utilized the HITEMP 2020 database for methane [78].

5.1.4 Validation and HMX Flame Measurements

Measurements of temperature and CO concentration in static-gas cell experiments were accurate within 1.5% and 1.8% of known values, respectively, with a 1-σ precision of 0.7% and 1.2%, respectively. Figure 5.3a displays a representative measured and best-fit absorbance spectra acquired in the HMX flame during quasi-steady-state. The 1-σ noise level in the measured absorbance was 0.25%. Time histories of temperature and $\chi_{CO}L$ are shown in Figure 5.3b. The diagnostic resolved pre-ignition decomposition of HMX through quasi-steady burning. At quasi-steady-state, the measured time-averaged temperature and CO column density was 2620 K and 0.32 cm (i.e., 21.3% by mole for a 1.5 cm thick flame) respectively, which agree well with measurements acquired in our lab using quantum-cascade lasers similar to as reported in [6]. The 1-σ precisions are 10 K (0.4%) and 0.007 cm (2.3%). Throughout the burn, the temperature decreased by ≈100 K due to the surface of HMX regressing away from the measurement line-of-sight. Large amplitude oscillations in $\chi_{CO}L$ are observed at 12.8 Hz as a result of a natural flame instability [37]. Temperature

measurements acquired prior to ignition were enabled by the broad spectral bandwidth of the measurement. Measurements with an absorbance SNR as low as 20 were made, which occurred at a CO column density of 0.003 cm and temperature of 500 K.

The temperature and CH_4 concentration measured in static-gas cell experiments were accurate within 1.2% and 0.8% of known values, respectively, with a 1-σ precision of 0.2% and 0.7%, respectively. Figure 5.4a shows a typical single-shot absorbance spectra of CH_4's Q-branch and Figure 5.4b shows measured time histories of temperature and CH_4 column density acquired in a partially-premixed CH_4-air Hencken-burner flame. The time-averaged values of temperature and column density are 1023 K and 0.283 cm, both of which exhibit a 95 Hz oscillation (due to a combustion instability) with a peak-to-peak amplitude of 28 K and 0.01 cm, respectively. After accounting for this oscillation, the 1-σ precision of the measured temperature and column density are 3 K (0.3%) and 0.003 cm (1%), respectively. The results shown were acquired with an absorbance-noise level of $\approx$ 0.5%.

The results presented in this chapter illustrate that ultrafast-laser-absorption spectroscopy in the mid-infrared is capable of high-fidelity characterization of combustion gases with ultrafast time resolution.

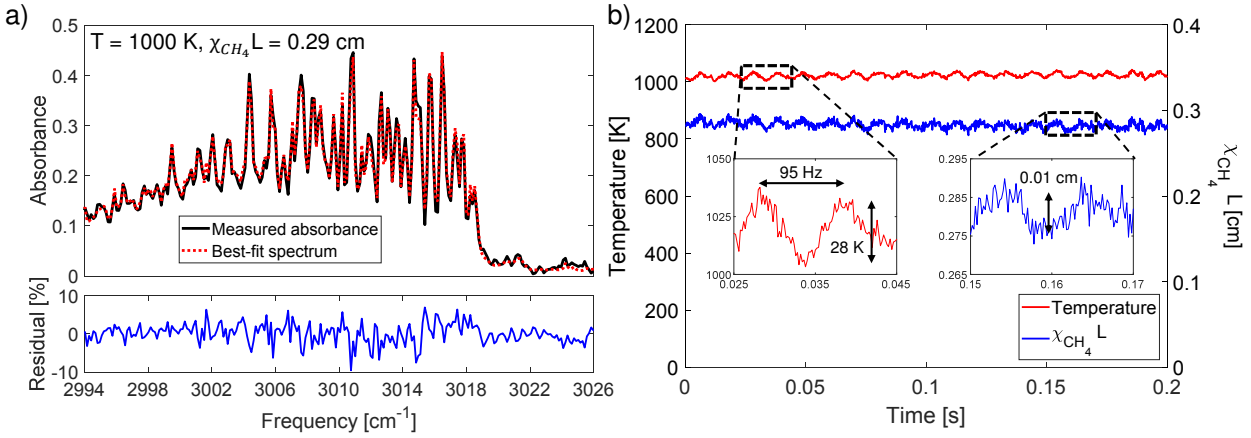

Figure 5.4. Example single-shot measurement and best-fit spectrum of CH_4's Q-branch (a) and corresponding time history of temperature and $\chi_{CH_4}L$ acquired in partially premixed CH_4-air flame (b).

5.2 Refinement of ULAS Measurements and Extension to CO_2

The contents of this section are reprinted from [79].

5.2.1 Introduction

In the previous section, we demonstrated the first (to our knowledge) mid-infrared, single-shot, ultrafast (i.e., femtosecond) laser-absorption measurements of temperature and species in combustion gases. Specifically, measurements of temperature, CO, and CH_4 were acquired in flames with a repetition rate of 5 kHz and time resolution estimated to be less than 1 nanosecond (after accounting for dispersion and time-of-flight of the pulse through the absorbing gas) [62]. This diagnostic offers several advantages compared to alternative broadband LAS diagnostics. Perhaps most significantly, the time resolution of the diagnostic is at minimum 3 orders of magnitude faster than previously reported infrared LAS diagnostics applied to combustion gases, albeit with a lower measurement repetition rate compared to some TDL-, QCL-, and VCSEL-based diagnostics [1]. In addition, by utilizing a high-density, 2D focal plane array as the detector, this diagnostic offers the potential to provide high-resolution 1D measurements of absorbance spectra and, therefore, thermochemical flame structure similar to recently developed scanned-wavelength laser-absorption-imaging diagnostics [7], [55].

The work presented in this section continues to build on our recently developed mid-infrared ultrafast-laser-absorption diagnostic [62], and further demonstrates its unique capabilities. In particular, this work highlights two of the key strengths mentioned in the previous paragraph. (1) The utility of being able to measure various species at different wavelengths with a single lightsource, through extension of the diagnostic to single-shot measurements of temperature and CO_2. Notably, results presented in this section demonstrate how species-specific temperature differences can be leveraged to provide spatial information of flame

structure. (2) Refinements made to the optical setup enabled the first mid-infrared, single-shot, *single-spectrum* (i.e., no spatial averaging of spectra) measurements of temperature and species with ultrafast time resolution. Thus, these measurements present a stepping stone towards realizing single-shot, 1D measurements of T and χ_{abs}. The CO- and CO_2-based diagnostics were applied to acquire measurements of temperature, CO and CO_2 at 5 kHz in laser-ignited HMX (i.e., 1,3,5,7-tetranitro-1,3,5,7-tetrazoctane) flames.

5.2.2 Wavelength and Species Selection

CO and CO_2 were chosen for the application of this diagnostic because they are key combustion products of many propellants and hydrocarbon fuels. Further, they are both often present in concentrations that are sufficient for high-fidelity measurements of temperature in many flames and combustion gases of practical importance. Last, comparing temperature measurements acquired via an intermediate species (e.g., CO) and a complete combustion product (e.g., CO_2) can provide improved insight into the homogeneity of the combustion gas.

For measurements of CO_2 spectra, care was taken to choose a spectral window which has high temperature sensitivity and weak absorbance at ambient temperature, the latter is necessary to avoid strong absorbance from ambient CO_2 since the optical path length through the air was nearly 4 m. As a result, a spectral window centered at 4186 nm (2389 cm^{-1}) was used to measure high lower-state-energy transitions near the bandhead of CO_2's fundamental asymmetric-stretch vibration band. Recent work has shown that this region of CO_2's absorbance spectrum provides high-temperature sensitivity at flame conditions and provides access to well-isolated absorption transitions [80].

For measurements of CO spectra, wavelengths near 4975 nm (2010 cm^{-1}) were used to access strong, well isolated, high lower-state-energy transitions in CO's P-branch which exhibit minimal interference with H_2O and CO_2 transitions [76]. Compared to our prior work in [7], [62] and Chapter 5.1, longer wavelengths were used to access P-branch transitions with even larger lower-state energy. This was done to further desensitize the absorption measurements to boundary layers.

5.2.3 Experimental Details

Fig. 5.5 shows a schematic summarizing the experimental setup and data-processing procedure for the data presented in this section. In the interest of brevity, only the experimental details which differ from that in the Chapter 5.1 will be discussed here in detail. The ultrafast laser system used is identical to that described in Chapter 5.1. In this work, pulses were centered at 4.2 μm and 4.9 μm for measurements of CO_2 and CO respectively. Pulse energies immediately downstream of the OPA were were 14 μJ and 4 μJ at 4.2 μm and 4.9 μm respectively.

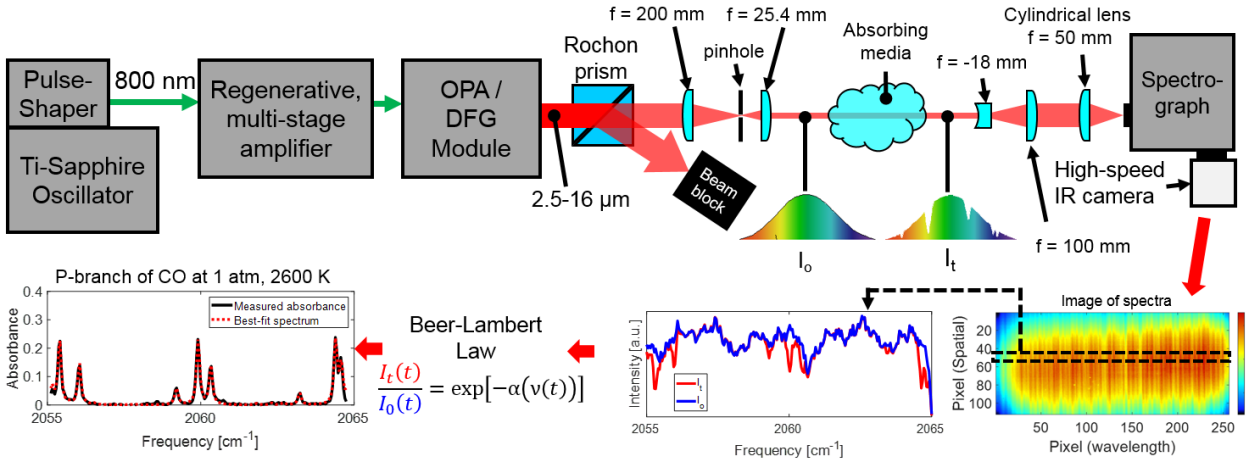

Figure 5.5. Schematic illustrating the ultrafast laser system, optical setup and general data-processing procedures.

Prior to being passed through the test gas, the $1/e^2$ beam diameter was reduced from ≈7 mm to ≈800 μm using a lens telescope consisting of a CaF_2 plano-convex lens ($f = 200$ mm) to focus the beam and a Si plano-convex lens ($f = 25.4$ mm, 2-5 μm AR coating) to collimate the output beam. Since the output beam from the OPA has a relatively low quality factor (e.g., beam was noticeably elliptical), a 200 μm pinhole was placed at the focal point of the $f = 200$ mm lens. This improved the beam quality by acting as a spatial filter (i.e., rejecting the non-gaussian components of the laser beam). In turn, this enabled tighter collimation of the beam and tighter focusing of the beam onto the slit of the spectrograph. This ultimately improved the spatial and spectral resolution of the diagnostic. After passing through the absorbing gas, the beam was expanded using a second lens telescope. The purpose of this

telescope was to increase the laser beam diameter such that the beam could be focused to a smaller waist on the spectrograph slit, ultimately providing improved spectral resolution. This telescope consisted of a CaF_2, plano-concave lens (f = -18 mm, 2-5 μm AR coating) to expand the laser beam and a CaF_2, plano-convex lens (f = 100 mm, 2-5 μm AR coating) to collimate the beam. The input beam to this telescope had a $1/e^2$ diameter of ≈2 mm and an output $1/e^2$ beam diameter of ≈11 mm. A final ZnSe plano-convex cylindrical lens (f = 50 mm) focused the beam in one dimension onto the slit of the spectrograph.

In this work, images of baseline or transmitted laser intensity were acquired by the IR camera using a 44×320 pixel window. The x-dimension (320 pixels) of the recorded images corresponds to wavelength (or frequency) and the y-dimension (44 pixels) corresponds to vertical position within the beam of ultrafast pulses.

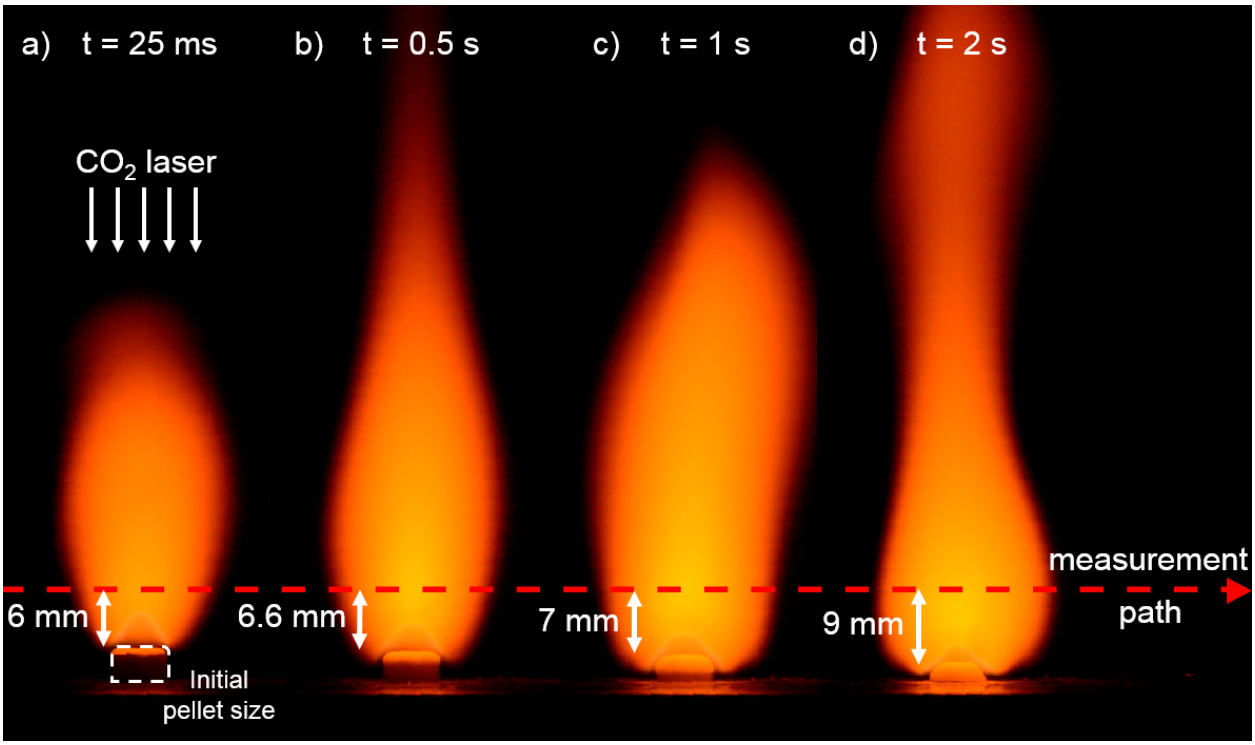

Figure 5.6. Images of CO_2-laser-ignited HMX flames taken with a Nikon D3200 at 60 FPS. The images shown correspond to the results presented in Figure 5.7. Select frames are shown corresponding to a) 25 ms, b) 0.5 s, c) 1 s and d) 2 s after ignition. The images illustrate the variation in flame structure due to the low frequency (≈11 Hz) instability.

All measurements presented in this work were acquired in HMX flames burning in air at atmospheric pressure. Example images (taken with a Nikon D3200 DSLR) of an HMX flame at various times after ignition are shown in Fig. 5.6. Measurements of temperature, CO, and CO_2 were acquired 6 mm above the initial surface location of the HMX pellet. Data acquisition began 100 ms before the CO_2 laser was turned on to allow for the baseline laser intensity to be recorded.

5.2.4 Data Processing Procedure

The data-processing procedure and spectral-fitting routine employed in this work are thoroughly described in [62] and Section 5.1 and only additions or changes to the procedure will be discussed here. The most pertinent details are repeated here for clarity and several minor changes are discussed.

The baseline laser intensity (I_o) was constructed by averaging together 250 images of laser pulses (to mitigate pixel noise) which were recorded in the absence of the test gas. Although the camera records 44 spectra (I_o or I_t) for each laser pulse, only one spectrum of I_t was utilized to demonstrate the single-shot, single-spectrum SNR of the diagnostic and, therefore, demonstrate this diagnostic's potential to provide 1D-resolved measurements of absorbance spectra.

Spectroscopic parameters for simulating absorbance spectra were taken from the HITEMP2010 [35] and HITEMP2019 [77] databases for CO_2 and CO, respectively. Spectra were simulated assuming isolated lines and thus linemixing effects were ignored.

Significant changes to the parameters floated in the spectral fitting routine were applied for the work in this section. The IRF used for this work was modeled as a Gaussian-Lorentzian function. The weighting parameter (which determines the relative strength of Gaussian and Lorentzian compomemts) was floated in the nonlinear fitting routine alongside the IRF FWHM. Additionally, a linear (i.e., 2 parameter) scaling factor on I_0 was floated in the fitting routine, whereas previously only a scalar correction was floated. The linecenter frequencies for several prominent spectral lines was also floated, as previously discussed. However, here the remainder of the frequency axis was filled in using cubic spline interpo-

lation. The frequency axis was a nearly linear function of pixel number (≈0.1 nm/pixel). The linecenter frequencies and parameters governing the shape of the IRF were constant throughout the duration of the test. Once their values were determined by the spectral fitting routine using a reference spectrum, they were held constant throughout the remainder of the data processing.

5.2.5 Results

This section presents ULAS measurements of temperature (from CO and CO_2) and the column density of CO and CO_2 acquired in laser-ignited HMX flames burning in air at 1 atm. Since HMX is fuel rich, HMX flames burning in air exhibit a partially premixed flame structure with a fuel-rich core surrounded by a shroud of combustion products with greater CO_2 concentration due to diffusion of atmospheric oxygen into the flame. Measurements of temperature acquired from path-integrated absorbance spectra of CO and CO_2 are both presented to highlight species-specific differences in the measured temperature which, in the limit of linearly-temperature-dependent linestrengths, is given by an absorbing-species-weighted (partial pressure or number density weighting) path-averaged temperature [48]. As a result, CO-based temperature measurements are expected to be more representative

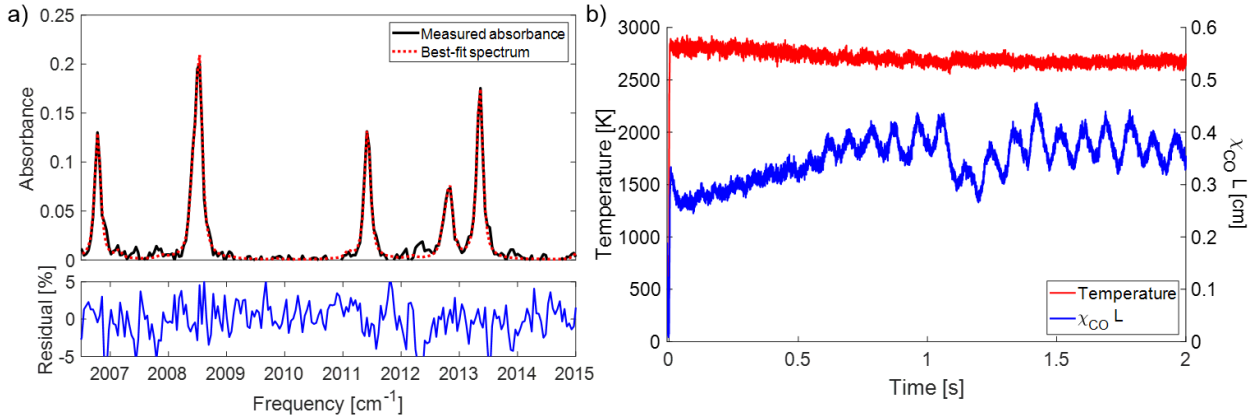

Figure 5.7. (a) A representative, single-shot, single-row measurement of CO's absorbance spectrum and the best-fit spectrum acquired 1.5 s after ignition. (b) Measured time histories of T_{CO} and CO column density ($\chi_{CO}L$) acquired in a laser-ignited HMX flame.

of the flame core (consisting of HMX combustion products), while CO_2-based temperature measurements will be biased more towards the surrounding shroud of HMX-air combustion products. The results presented next support these arguments.

Fig. 5.7(a) shows a representative single-shot measurement of CO's absorbance spectrum near 2010 cm^{-1} and its corresponding best-fit spectrum acquired 1.5 s after ignition. The measured and best-fit spectra exhibit excellent agreement with a peak-normalized residual less than 5%. The baseline 1-σ noise level in absorbance was 0.31% and the measured FWHM of the IRF for this dataset was 0.26 nm.

Fig. 5.7(b) shows measured time histories of CO-based temperature (T_{CO}) and $\chi_{CO}L$. Approximately 0.1 s after ignition, T_{CO} reached a maximum quasi-steady value of approximately 2800 K and as the burning surface regressed, T_{CO} decreased to 2700 K at 2 s after ignition. The 1-σ precision in temperature was 57 K (i.e., 2% of the measurement at 2750 K). The maximum quasi-steady value of T_{CO} is close (within 117 K) to the adiabatic flame temperature of HMX (2917 K at 1 atm) predicted by NASA CEA. While the HMX flames are not adiabatic, this suggests that the CO-based temperature measurement is not heavily influenced by line-of-sight non-uniformities and is representative of conditions in the core of the flame. It should be noted that the maximum T_{CO} is ≈130 K hotter than that previously measured in our lab at similar conditions using CO transitions near 2060 cm^{-1} [62]. This relatively minor difference is likely due to the fact that higher-energy CO transitions were measured in this work, thereby further desensitizing the measured spectra to cooler regions of flame gas that exist closer to the flame perimeter [1], [48].

The measured CO column density was ≈0.26 cm at 0.1 s after ignition and it increased steadily to a time-averaged value of 0.375 cm. The 1-σ precision in column density was 3.7% at a value of 0.375 cm. In addition, an oscillation in CO column density was observed which grew in amplitude until 1 s after ignition where the amplitude reached steady state. The measured frequency and amplitude of the oscillation were 11.1 Hz and 0.07 cm, respectively. This results from a well known and easily observed instability in flame structure [37].

Fig. 5.8(a) shows an example single-shot, single-row measurement of CO_2's absorbance spectrum near 2394 cm^{-1} acquired in the HMX flame 1.5 seconds after ignition. The 1-σ noise level in the measured absorbance spectrum is 0.33% and the FWHM of the IRF was 0.27

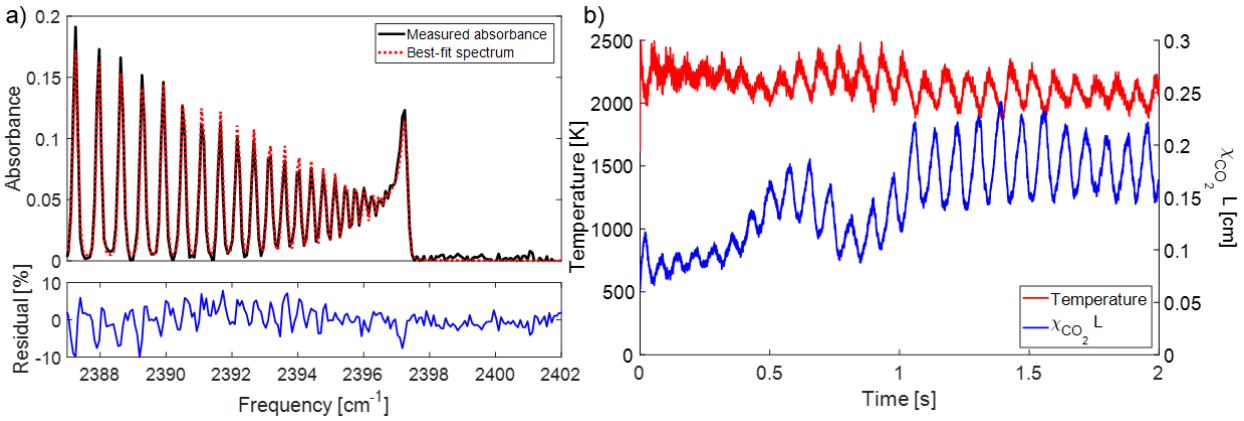

Figure 5.8. (a) A representative, single-shot, single-row measurement of CO_2's absorbance spectrum and the best-fit spectrum acquired 1.5 s after ignition. (b) Measured time histories of T_{CO_2} and CO_2 column density ($\chi_{CO_2}L$) acquired in a laser-ignited HMX flame.

nm for the best-fit spectrum. Interestingly, the best-fit spectrum consistently under-predicts the measured absorbance for the lower-energy transitions and over-predicts the absorbance of the higher-energy transitions located closer to the bandhead, with the exception of the bandhead itself which may result from linemixing effects [81]. These differences likely result primarily from the fact that the measured CO_2 spectra are acquired over a range of temperatures (due to the path-integrated nature of LAS and the partially premixed flame structure of HMX flames in air) while the modelled spectrum is calculated at a single temperature. This suggests that line-of-sight non-uniformities in temperature significantly impact the measurements of CO_2 spectra.

Fig. 5.8(b) shows measured time histories of CO_2-based temperature (T_{CO_2}) and $\chi_{CO_2}L$. The mean value of T_{CO_2} is 2250 K at 0.1 s after ignition and this decreases steadily to 2050 K at 2 s after ignition. The 1-σ precision of T_{CO_2} is 27.4 K (1.2%). Unlike T_{CO}, T_{CO_2} oscillated at 12.2 Hz with an amplitude of 350 K (i.e., 16% at 2200 K). The column density of CO_2 increased from an average value of 0.8 cm shortly after ignition to 0.175 cm at approximately 1 s after ignition, after which the column density reached a plateau. The 1-σ precision of the column density measurement was 1.1% of the measured value. An oscillation in CO_2 column density was also observed at 12.2 Hz, but ≈180 degrees out-of-phase with T_{CO_2}. The

amplitude of the oscillation varied from a minimum of 0.015 cm at 0.25 s after ignition to a maximum of 0.09 cm 1.5 s after ignition.

5.2.6 Discussion

Comparing the results acquired via path-integrated measurements of CO and CO_2 absorbance spectra reveals several interesting observations about the diagnostics presented and the thermochemical structure of HMX flames burning in air. First, the results indicate that the CO-based temperature diagnostic is insensitive to line-of-sight non-uniformities that are encountered in these flames and is therefore capable of providing accurate measurements of the core flame conditions. This is supported by the fact that T_{CO} was within ≈117 K of the adiabatic flame temperature and agrees well with thermocouple measurements presented in the literature [36], especially given the large uncertainty of thermocouple measurements at the temperatures of interest here. Second, the combination of CO- and CO_2-based results suggest that the gas temperature is hottest in the flame core and cooler (on average) in the surrounding shroud of HMX-air combustion products. This is supported, perhaps most clearly, by the fact that T_{CO_2} is nearly 600 K lower than T_{CO}. This can be explained by recognizing that CO should predominantly exist in the flame core since it will be oxidized to CO_2 in regions where oxygen/air have diffused into the flame and, thus, it should also not exist in large quantities in the cold boundary layer surrounding the flame. In contrast, CO_2 should be biased towards the regions where oxygen/air have diffused into the flame (since HMX is fuel rich) and to the colder boundary layer gas surrounding the flame since it is fully oxidized. This is further supported by several key results. 1) The measured column density of CO_2 is consistent with significant diffusion and entrainment of air into the flame. For example, assuming an absorbing path length of 15 mm (as estimated from Fig. 5.6), the measured steady-state mole fraction of CO_2 at the measurement location is 0.12 which is significantly larger than that expected from combustion of pure HMX (i.e., 0.05 at equilibrium) [36]. 2) The column density of CO_2 oscillated ≈180 degrees out-of-phase with T_{CO_2}. This is consistent with CO_2 existing at lower temperatures (on average) when CO_2 is produced in the largest quantities (i.e., when diffusion from atmospheric oxygen into the

flame is most significant). 3) An oscillation was not observed in the measured T_{CO} which is consistent with measuring the equilibrium flame temperature of pure HMX as it should not be affected by the flame instability. 3) Last, the systematic error between the measured and best-fit absorbance spectra of CO_2 strongly suggests that, at the measurement location, CO_2 existed over a wide range of temperatures along the measurement line-of-sight.

5.2.7 Conclusions

The development and application of a mid-infrared ultrafast-laser-absorption diagnostic for measurements of temperature, CO, and CO_2 in combustion gases was presented. The first single-shot, single-spectrum (i.e., no spatial averaging), ultrafast measurements of temperature and species were demonstrated, thereby marking an important step towards acquiring 1D thermometry and concentration measurements with sub-nanosecond time resolution.

This diagnostic was applied to characterize HMX flames burning in air at 1 atm. The results demonstrate that comparing temperature measurements acquired via the path-integrated absorbance spectra of multiple species can provide improved insight into the flame structure. Combining measurements of temperature and column density from CO and CO_2 spectra provided improved insight into the line-of-sight non-uniformities encountered in HMX flames burning in air. The results suggest that the CO-based temperature measurements are representative of the conditions in the flame core, while CO_2-based temperature measurements are heavily biased towards the outer regions of the flame. The results also suggest that the highest temperatures exist in the core of the HMX flame, with temperatures decreasing (on average) towards the boundary layer between air and HMX combustion products.

6. ABSORPTION SPECTROSCOPY MODELING CONSIDERATIONS FOR BROADBAND, SPECTROMETER-BASED ABSORPTION MEASUREMENTS

6.1 Inferring Instrument-Broadening Parameters with a Multi-Spectrum Fitting Routine

6.1.1 Background

Accurate characterization of various line-broadening effects is crucial for accurate modeling of absorption spectra, and hence, for accurate measurement of gas properties when extraction relies on the fitting of an absorption spectroscopy model to measured data [1], [82], [83]. The broadening (or narrowing) of an absorption feature is due to a combination of many broadening sources. Generally, these sources can be separated into 2 categories. (1) Physical broadening effects are those that result from characteristics of the absorbing atom or molecule and the properties of its environment. Some well known examples include natural broadening, collisional broadening, Doppler broadening, and Dicke narrowing. (2) Instrument broadening effects are those which result from the apparatus being used to observe the absorption feature, commonly, the slit-function in the case of spectrometers, spectrographs or monochromators [82] or the laser linewidth in the case of scanned-wavelength spectroscopy (e.g., scanned direct-absorption or WMS techniques) [1]. When instrument broadening is small compared to physical broadening sources (as is often the case in TDLAS) its effects can generally be neglected. However, challenges arise when the FWHM of instrument broadening is similar to, or greater than that of physical broadening and error in one or the other can lead to inaccurate determination of gas properties.

Instrument, doppler and collisional broadening have been the dominant sources of line-broadening in the ULAS measurements acquired thus far [62], [79], [84]. The Doppler-broadening FWHM ($\Delta\nu_D$) has had the least uncertainty for given gas conditions, as it is only a function of molecular weight, temperature and linecenter frequency, which are either measured or already well known. Uncertainty in collisional-broadening FWHM ($\Delta\nu_C$) was much greater, due to uncertainty in both bath gas composition (e.g., in flames) and in

collisional broadening coefficients within databases. Often, this uncertainty is accounted for in spectral-fitting routines by floating either a scalar multiplier on all $\Delta\nu_C$ or floating $\Delta\nu_C$ directly for a small number of lines [1]. Initially, ULAS measurements have been made while floating instrument broadening parameters. However, simultaneously floating the IRF and collisional broadening half-widths in the nonlinear fitting routine can be unsuitable due to the similar effect they have on transition lineshapes, and the high dispersion per data point (i.e., few pixels per absorption transition) which makes measurements insensitive to subtle differences in lineshapes. Likely, the fitting routine would converge on incorrect values for both instrument and collisional broadening parameters and, in some cases yield substantial errors in measured gas properties. For example, collisional broadening is itself dependent on absorbing species concentration and temperature through Eq. 6.1.

$$\Delta\nu_c = 2P\sum_A \chi_A \gamma_{B-A}(T) \tag{6.1}$$

An error in the collisional broadening coefficients can be offset through converging on incorrect values for instrument broadening parameters, while maintaining a low sum-of-squares residual (the optimization parameter used by the fitting routine). Hence, it can be necessary to determine the IRF elsewhere so it can be held fixed in the spectral-fitting routine. This is critical when the measured absorbance spectrum does not possess a wide variety of linewidths, as is the case for the ULAS measurements in CO's P-branch.

There are numerous different methods for determining the IRF of a spectrograph with a given optical setup (i.e., slit width, focal length of lens, etc.). One of the most common is to measure the IRF through fitting measured data of a well known spectra. For CARS (coherent anti-Stokes Raman scattering) spectroscopy measurements, it is common to determine the IRF from measurements of the CARS spectrum of N_2 at atmospheric conditions, which is known to high accuracy [85], [86]. Another technique, is to measure the IRF directly by using a sufficiently narrowband (relative to the IRF FWHM) reference source such as a narrowband laser, low-pressure hollow-cathode lamp or a narrow, well-characterized absorption line [82], [87]. The IRF can be also be inferred in the case of a reference source with a non-negligible

but well-characterized linewidth [88]. That said, these methods were not deemed suitable for or sufficiently robust for the ULAS diagnostics reported here.

6.1.2 Multi-Spectrum Fitting Routine

In this work, the IRF was inferred by applying a multi-spectrum fitting routine to ULAS data acquired at a variety of known gas conditions. The multi-spectrum fitting routine involved simultaneously fitting simulated absorbance spectra to absorbance spectra acquired across multiple pressures while floating a single IRF and correction factor on $\Delta\nu_C$. The latter was done to account for uncertainty in the collisional linewidths. Simultaneously fitting simulated spectra to data acquired at vastly different pressures allows for more accurate and robust determination of instrument and collisional broadening parameters by decreasing the total number of free parameters per spectrum [14], and by decoupling of the effects of instrument and collisional broadening. For example, spectra acquired at sufficiently low pressure are dominated by instrument broadening and are relatively insensitive to errors in collisional broadening, while this effect is reversed at high pressure.

The ULAS data used for the multi-spectrum fitting routine was collected in a high-uniformity, heated-gas cell (described by Schwarm et al. [89]) at pressures of 0.3, 1, 3, 10, 20, and 40 bar. The cell was heated to ≈1000 K and filled with a gas mixture of 2 % CO and 1.8% CO_2 by mole with a balance of nitrogen. The gas pressure was measured using a Unik-5000 pressure transducer with a full-scale range of 0 to 70 bar and an accuracy of ± 0.028 bar. Temperature was measured using three type-K thermocouples with a nominal accuracy of 0.75% (at ≥ 600 K) fixed to the outside of the gas cell in a configuration identical to that described in [89]. The gas cell was equipped with 15 cm long, wedged CaF_2 rods which provided a path length through the test gas of 9.4 cm at room temperature. The lens telescope portion of the corrective optics described in section. 7.2.3 was not used for the validation measurements, since the geometry of the gas cell and tube furnace precluded this. However, the 250 mm focal length lens was used for consistency with the setup used for propellant tests. Datasets were acquired using two gratings with 300 lines/mm or 150 lines/mm and respective theoretical resolutions of 0.21 nm or 0.61 nm.

In the fitting routine, the IRF was modeled by Eq. 6.2, which is a Gaussian-Lorentzian function, with the FWHM and lineshape weighting (proportion of the lineshape which is Gaussian vs Lorentzian) being floated as free parameters. The equation for the IRF is given as Eq. 6.2.

$$\phi_{IRF}(\lambda) = w\phi_L(\lambda) + (w-1)\phi_G(\lambda) \tag{6.2}$$

Here, ϕ_G and ϕ_L are Gaussian and Lorentzian lineshapes, both with integrated areas of unity, w is the lineshape weighting parameter, λ is the wavelength in nm and ϕ_{IRF} is the IRF. Collisional broadening coefficients for CO-CO_2 and CO-N_2 were taken from Hartmann et al. [90]. A global scaling factor for $\Delta\nu_C$ was floated in the fitting routine as well. The frequency axis and a linear baseline correction were floated for each spectrum according to normal data processing procedures, while temperature and absorbing species concentration were held constant at the known values. Spectra corresponding to 0.3 bar, 1 bar, 3 bar and 40 bar were used for the multi-spectrum fitting routine. Spectra acquired at 10 and 20 bar were omitted to prevent biasing the fitting routine towards high pressure cases, with comparatively strong collisional broadening.

The value of peak absorbance for instrument broadened absorbance spectra increases with pressure for otherwise equal gas conditions as illustrated by Fig. 6.1. Therefore, a theoretical 1% difference between measured and best-fit spectra results in a greater absolute difference (i.e., measured spectrum - simulated spectrum) for spectra acquired at higher pressures than those acquired at lower pressures. This could lead the multi-spectrum fitting routine to return a result which is biased toward high-pressure measurements, since the absolute difference is typically used by the fitting routine to determine goodness of fit. To mitigate potential bias, the difference between measured and simulated spectra were normalized to the peak measured absorbance. The measured and best-fit spectra determined by the multi-spectrum fitting routine for data acquired with the 300 lines/mm grating is shown in Fig. 6.1.

For data acquired with the 150 lines/mm grating, the multi-spectrum fitting routine returned a value of 0.5198 nm for the IRF FWHM and an instrument lineshape which

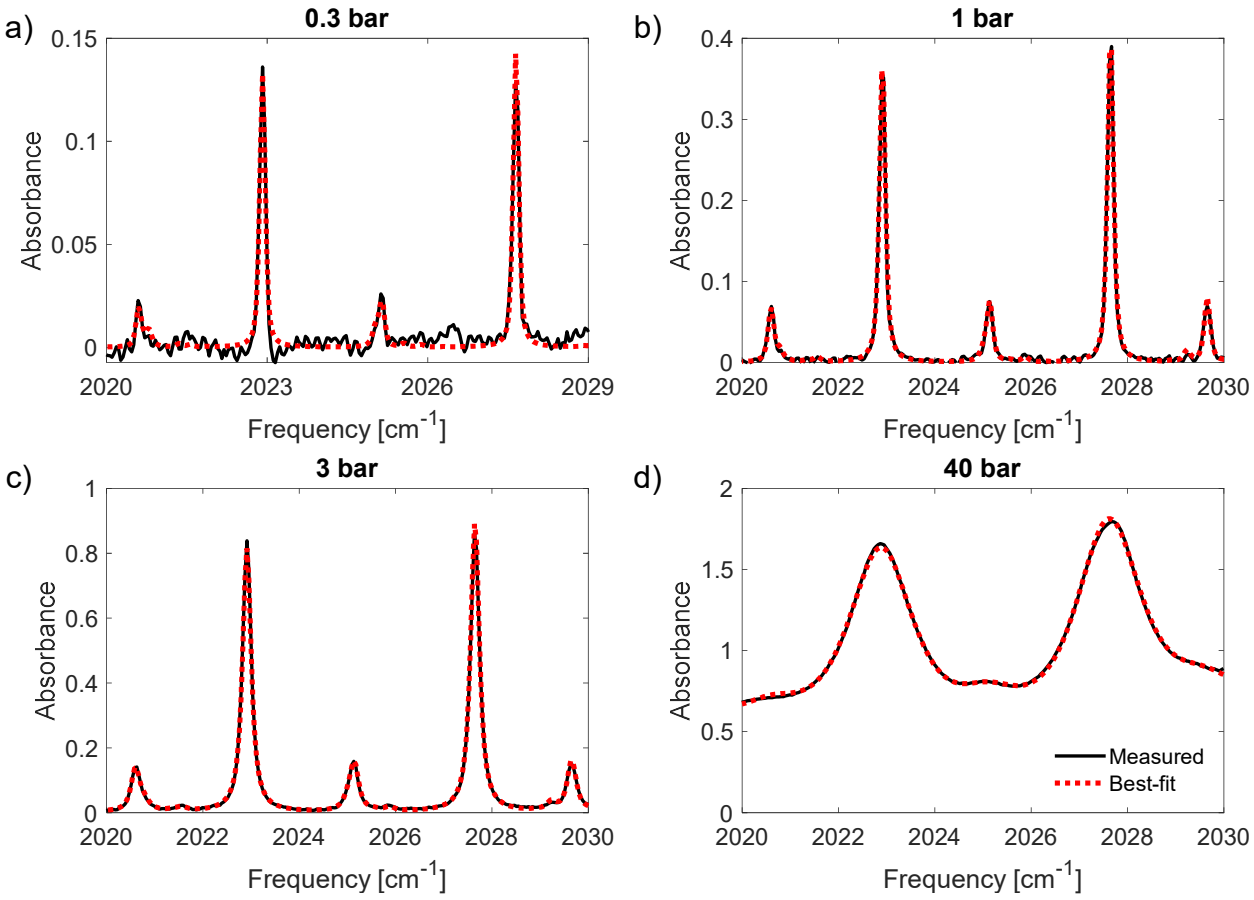

Figure 6.1. Measured and best-fit absorbance spectra of CO in a heated static-gas cell at ≈ 1000 K acquired using a 300 lines/mm grating. Each spectrum was fit simultaneously using the multi-spectrum fitting routine. Spectra were acquired at (a) 0.3 bar, (b) 1 bar, (c) 3 bar, and (d) 40 bar.

was 48.3 % Lorentzian. For the 300 lines/mm grating, the multi-spectrum fitting routine converged on an IRF FWHM of 0.297 nm and an instrument lineshape which was 61.5 % Lorentzian. The value for the scaling factor on $\Delta\nu_C$ was 0.91 for both gratings.

The multi-spectrum fitting technique was validated by processing data taken at each pressure individually according to the standard data processing procedure, though now with instrument broadening parameters held fixed to their respective values determined by the multi-spectrum fitting routine. In addition, the factor on $\Delta\nu_C$ was floated for consistency, because it must be floated when fitting to spectra acquired in flames to account for uncertainty in the collisional broadening FWHM. The results of the validation tests are reported in Fig. 6.2. All measurements were either within 5% of the known value, or within the

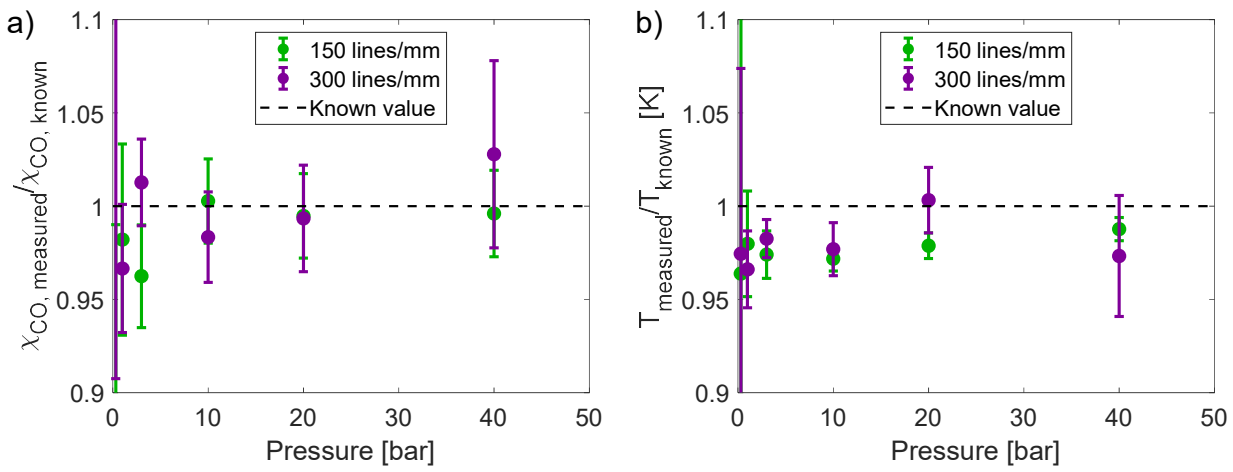

Figure 6.2. Temperature and absorbing species concentration measurements taken in a heated, static-gas cell. Instrument broadening parameters were fixed at those determined by the multi-spectrum fitting routine. A scalar factor for $\Delta\nu_C$ was floated as a free parameter.

bounds of the 95% confidence intervals. Note the poor measurement accuracy and large uncertainty for the 0.3 bar case is due to the low signal levels, indicating that measurements at this combination of resolution and pressure are likely outside the recommended capabilities of this diagnostic.

Uncertainty in the gas cell measurements was analyzed from 3 separate sources: uncertainty in the instrument broadening parameters, uncertainty in the best-fit spectra, and uncertainty in the absorbing path length. Uncertainty in instrument broadening parameters was quantified by calculating the 95% confidence interval for each parameter using the covariance matrix returned by the multi-spectrum fitting routine. The effect of each instrument broadening parameter on the determination of gas properties was nonlinear and coupled with other parameters, so a Monte Carlo method was used to determine their effect on the uncertainty in gas properties. The uncertainty in instrument broadening parameters was assumed to be normally distributed, with the standard deviation determined from the bounds of the 95% confidence interval. The value for IRF FWHM and lineshape weight were set as Gaussian random variables with corresponding means and standard deviations. The fitting routine for each pressure and grating was then run for each random broadening parameter for $n = 100$ trials. The resulting distributions in measured temperature and χ_{CO}

were determined to be normal by the Shapiro-Wilk test with a P-value of 0.05. Hence, the bounds of the 95% confidence intervals due to uncertainty in broadening parameters was determined as ± 1.96 standard deviations from the mean. Uncertainty due to fit for the one-at-a-time fitting routine was calculated in the same manner as from the multi-spectrum fitting routine. Uncertainty in the absorbing path-length was 2%. This value for uncertainty was chosen based on the perceived error in the length of the CaF_2 rods, uncertainty in the thickness of the epoxy seal for the rods, and the uncertainty in thermal expansion of the gas cell and CaF_2 rods at high temperatures. The relative uncertainty from all 3 sources were added in quadrature to yield the total uncertainty for the measured gas properties.

A critical requirement of the fitting routine is to provide a result which is not unique to the exact optical setup which was used to acquire the data for the multi-spectrum fitting routine. That is to say, the same broadening parameters are still valid when the setup is moved from the heated-gas cell to the combustion chamber for flame measurements. To test the robustness of this technique, the same broadening parameters were applied to datasets acquired with different optical setups. Here, different optical setups refers to optical setups which were "built" on different days, but with the same optical components and design (e.g., the same focal length lenses). These data sets were acquired in the same gas cell at identical conditions and gas compositions. Measurements were taken approximately 2 months apart and the entire optical setup was taken apart and rebuilt between measurements. Datasets were validated for both gratings, and instrument broadening parameters were held constant at the same values quoted above (i.e., the multi-spectrum fitting routine was not re-run for this new dataset). Gas properties were once again within 5% of the known values, with the known value falling within the uncertainty bound for most measurements.

The instrument broadening parameters were also measured directly, using a quantum-cascade laser (QCL) as a reference source. The QCL emitted near 4.8 μm and had a negligible linewidth (≈ 1 MHz) compared to the IRF. The laser beam was focused into the spectrograph using the same optical setup as was used for ULAS measurements in static-gas cell and propellant-flame tests. The measured spectrum was assumed to be the IRF. Broadening parameters were then determined by fitting a Gaussian-Lorentzian function to the measured IRF spectrum using a nonlinear fitting routine. Dispersion per pixel was set at the average

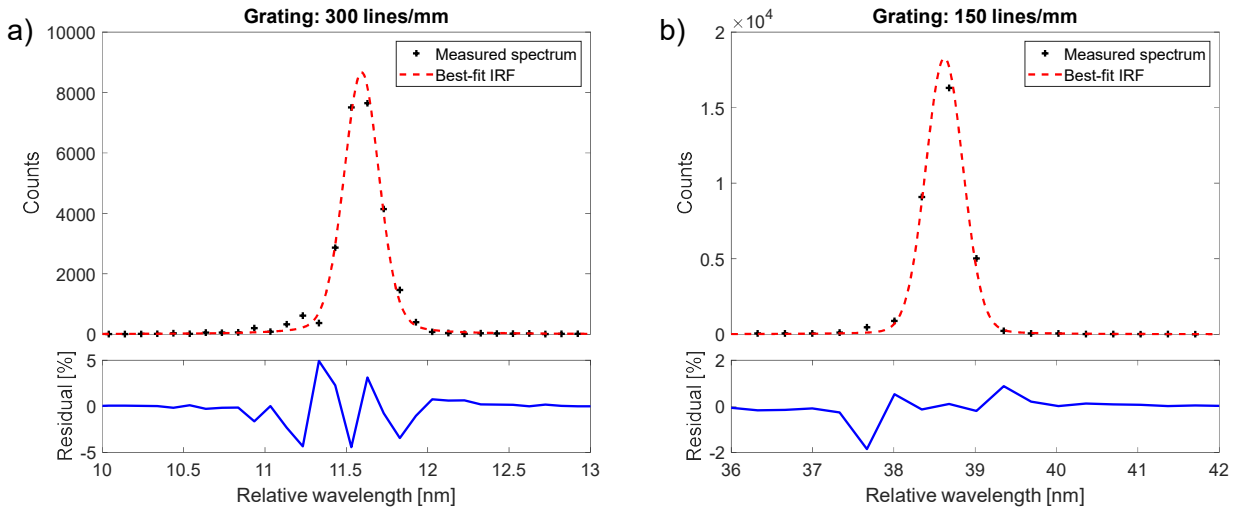

Figure 6.3. Direct measurement of the IRF using a QCL, as well as the best-fit IRF for (a) the 300 line/mm grating and (b) the 150 line/mm grating.

value determined by best-fit spectra from prior ULAS measurements near 4.8 μm. The resulting measured spectra and best-fit IRFs for both gratings are displayed in Fig. 6.3. The IRF FWHMs were measured to be 0.25 nm and 0.54 nm for the 300 line/mm and 150 line/mm gratings, respectively and were 99 % and 94% Lorentzian, respectively. The IRF FWHM values agree with those from the multi-spectrum fitting routine to within 4% and 16% respectively.

6.1.3 Discussion of Results

Using a multi-pressure, multi-spectrum fitting routine was shown to be effective in inferring instrument broadening parameters in the presence of uncertainty in other broadening sources. This is supported by 4 key findings. (1) The broadening parameters determined through the multi-spectrum fitting routine resulted in gas-cell validation measurements which were within 5% of the known value for both temperature and absorbing species concentration across a range of pressures. (2) In addition, this accuracy was shown to be repeatable across different optical setups and days. (3) The scaling factor on collisional broadening was the same for both of the grating resolutions which the multi-spectrum routine was applied on, and the value for the scaling factor is consistent with broadening uncertainties reported in

the literature [91]. Further, the same value for the collisional broadening scaling factor is to be expected since uncertainty in collisional broadening should not vary with measurement resolution, for measurements acquired using the same spectral window. (4) Last, the instrument broadening IRF FWHM agrees with values which were measured directly using a QCL. While the lineshape-weighting parameter did not agree well between the multi-spectrum fitting routine and the empirical measurement, this is thought to be due to the low spectral resolution of the empirical measurements (the IRF was measured on only ≈ 5 data points), making the technique insensitive to the instrument lineshape.

6.2 Effect of Interpolation and Spectral Resolution on Modeling Spectrometer-Based Absorption Measurements

The most common way to extract gas properties from measured LAS data is through the fitting of an absorption spectroscopy model. In addition to capturing the physics of the absorbing molecules or atoms, an absorption spectroscopy model which returns accurate measurements must also faithfully simulate the physical processes which govern the impact of the optical setup and data acquisition system. An important, yet commonly overlooked detail when simulating absorbance spectra for a spectral fitting routine is the spectral resolution used at various stages in the simulation and the methodology of moving between spectral resolutions (i.e., of measured data vs simulated spectra).

Spectral discretization becomes significant when the dispersion per pixel (or data point) is large compared to the linewidth of a measured spectral feature. In this situation, it is generally necessary to initially simulate spectra at a much higher resolution than the measured spectrum, in order to preserve spectral characteristics such as the integrated absorbance or peak absorbance. The interpolation method used to "down sample" a spectrum simulated with a finely spaced frequency axis to the comparatively course frequency axis of the measurement can alter the down sampled spectrum. The correct interpolation method mirrors the physical discretization of the spectrum by the focal plane array (FPA) of the camera.

Fig. 6.4a illustrates the discretization of a transmitted intensity spectrum by the FPA of an IR camera. A laser pulse which has been dispersed by a spectrometer near the FPA has a continuous intensity spectrum which has been broadened by the IRF. When the pulse hits the

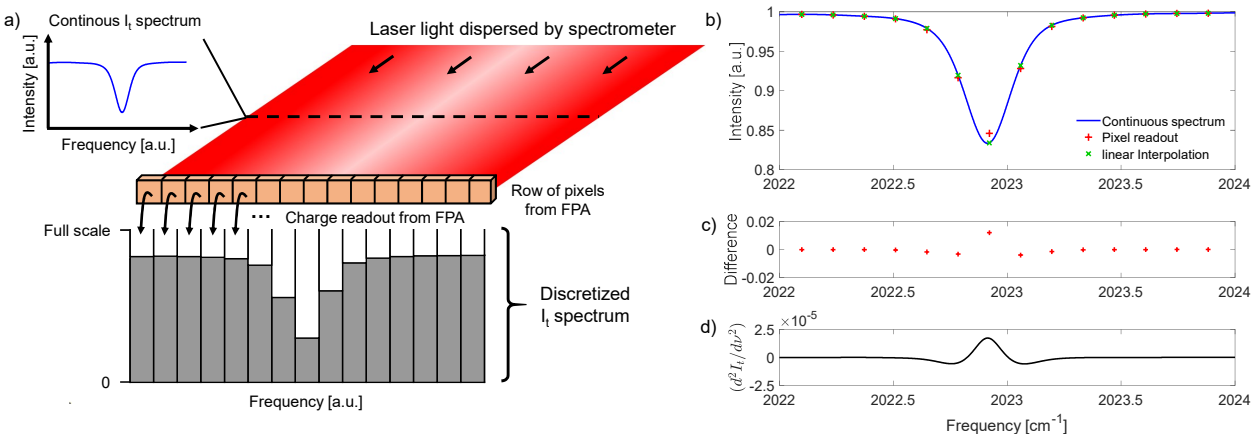

Figure 6.4. A schematic illustrating the discretization process of pixel detectors, and the fidelity of interpolation methods on mirroring this process. a) The discretization of a transmitted intensity spectrum by a row of pixels on the FPA. b) A plot comparing the a continuous spectrum with both a binning and non-binning (linearly-interpolated). c) Error (difference) between the binning and non-binning interpolation methods. d) Second derivative of transmitted intensity spectrum.

FPA, the light is collected by individual pixels, in effect, spatially binning the signal according to the pixel's physical dimensions. At the end of the camera's integration time, the camera reads out a single value for each pixel, which corresponds to the average incident intensity in both space and time. In a spectral fitting routine, the spectrum simulated with fine frequency spacing is the equivalent of the real-world continuous intensity spectrum. When down-sampling this spectrum to the frequency axis of the measured spectrum, each data point of the course spectrum should be calculated as the mean value of the fine spectrum across the width of the bin. The effect this interpolation has on the spectrum, and the difference between "binning interpolation" and traditional linear interpolation is displayed in Fig. 6.4b and Fig. 6.4c respectively. The error between interpolation methods is generally proportional to the second derivative of the spectrum, which is shown for reference in Fig. 6.4d. In essence, the interpolation method becomes significant when the intensity variation across a pixel cannot be assumed to be linear, because for linear variation, both linear interpolations and the mean value will be equivalent.

6.3 Potential Error Due to Uncertainty in the Non-Absorbing Baseline

Measurements of the baseline laser intensity and of the camera background (e.g., of ambient emission) are necessarily acquired post-convolution with the IRF. Hence, the "true baseline" and "true background" (i.e., the baseline or background prior to convolution with the IRF) are typically unknown. Knowledge of the true background is not necessary because the measured background is used only to subtract the likewise instrument broadened background from spectra of I_0 or I_t.

However, knowledge of the true baseline is needed to accurately simulate absorbance spectroscopy measurements. This is explained by the following. Spectral variations in the baseline laser intensity with a comparable period to that of absorption transitions can introduce distortions into measured spectral lineshapes during instrument broadening. Ideally, these distortions are replicated when simulating LAS measurements by simulating a spectrum of transmitted intensity using the Beer-Lambert Law, $I_t = I_0 e^{exp(\alpha(\nu))}$, where I_0 and $\alpha(\nu)$ are the baseline laser intensity and spectral absorbance pre-convolution with the IRF. In essence, this mirrors the sequence of physical events during acquisition of a ULAS measurement, because instrument broadening of I_0 and I_t happens subsequent to absorption in the test gas.

Knowledge of the true baseline is possible through deconvolving the IRF from the measured baseline. However, in practice this is a challenging and complex task due to the ill-posed nature of the problem, and sensitivity of the result to slight errors in inferred instrument broadening parameters. Methods such as Tikanov regularization may be employed to improve solution stability, and should be explored in future work.

For all ULAS measurements presented in this work, transmitted intensity spectra were simulated using a so called "semi-empirical" baseline. This simply means that a spectrum of baseline laser intensity was recorded and used within the spectral model as if it were the true baseline, while acknowledging that it likely lies somewhere in between the true baseline and a flat baseline (i.e., no variation in spectral intensity whatsoever). To illustrate the effects of various ways of handling the baseline laser intensity, three cases are analysed. The first is a flat baseline, the second, an empirically measured baseline (the method used for ULAS

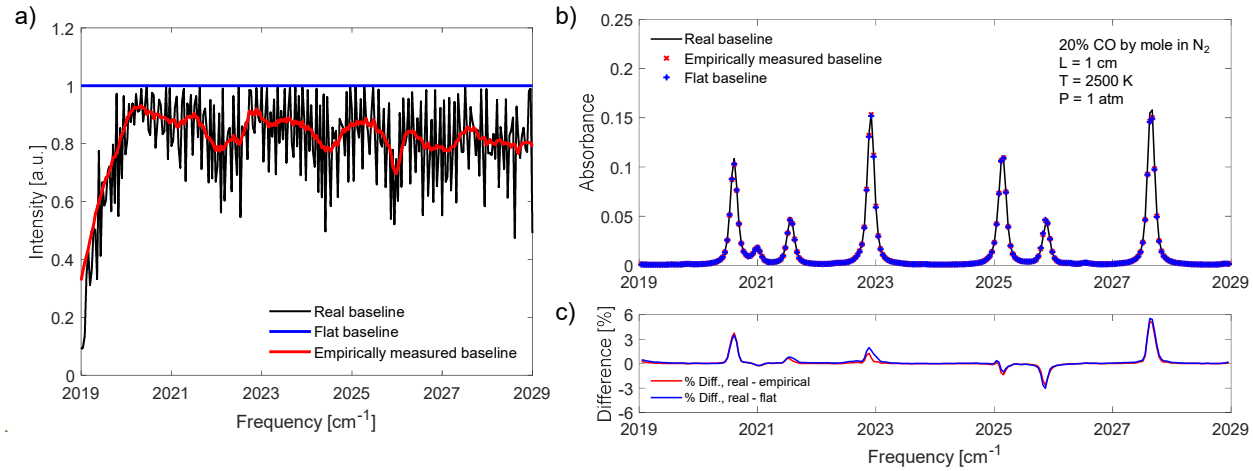

Figure 6.5. The effects of complex baseline variations on measured absorbance spectra. a) Three different baselines used for comparison, a flat baseline, an empirically measured (post IRF convolution) baseline, and a potentially deconvolved baseline. b) Absorbance spectra calculated using each of the 3 baselines. c) The percent difference between the flat and real, and the empirically measured and real baselines.

measurements thus far) and a potential true baseline with high-frequency structure. This potential true baseline was generated by running a non-linear fitting routine which floated each point of the spectrum, and convolved them with the IRF determined by the multi-spectrum fitting routine for the 300 lines/mm grating. The fitting routine converged when the post-convolution spectrum was nearly equal to the empirically measured baseline, and hence can be considered a potential true baseline. Each of these baselines is plotted in Fig. 6.5a. An absorbance spectra was was used to calculate I_t using each of the three baselines, and then both I_0 and I_t were convolved with the IRF for each case. Spectral absorbance was then calculated and plotted in Fig. 6.5b. For this study, the spectra generated with the true baseline was considered the "correct" version, and so the flat baseline and empirically measured baseline are compared against that in Fig 6.5c. As illustrated, there is the potential for non-negligible effects (on the order of 5% deviation) on absorbance spectra due to having incomplete knowledge of the non-absorbing baseline. The empirically measured baseline is shown to be marginally better in this case. Future work should study the potential effect this might have on ULAS measurements through validation tests.

7. APPLYING ULTRAFAST-LASER-ABSORPTION SPECTROSCOPY TO HIGH-PRESSURE PROPELLANT FLAMES

The contents of this section are adapted from [84].

7.1 Introduction

There remains a general need for non-invasive diagnostics capable of measuring gas properties in harsh, high-pressure environments representative of those encountered in practical combustors [1], [92]. Acquiring laser-absorption-spectroscopy (LAS) measurements in such environments, particularly those at elevated pressures, imposes a number of challenges. For example, spectroscopic challenges arise from increased collisional broadening, which can complicate determination of gas properties by, for example, blending lines, reducing levels of differential absorption, and increasing uncertainty in the non-absorbing baseline due to the absence of non-resonant wavelengths [1]. Frequently, the greatest challenge in acquiring LAS measurements in harsh environments is tolerating non-absorbing transmission losses arising from beam steering, window fouling, and scattering and attenuation by particulates and droplets. In addition, pressure-induced reduction of combustion-relevant length- and time-scales can present further difficulties.

Non-absorbing transmission losses can reduce the accuracy and precision of LAS measurements primarily because they complicate the accurate determination of the baseline laser intensity [93], [94] and, secondarily, because they reduce the measurement signal-to-noise ratio (SNR). These challenges can be mitigated through: (1) using wavelength-modulation spectroscopy (WMS) [6], [8], [95], [96] or emerging free-induction-decay-based data-processing techniques [93], [94] to avoid the need to accurately model the baseline laser intensity, (2)

using a broadband light source which facilitates *in situ* determination of the baseline light intensity by collecting more diverse spectral information [62], [97]–[99], or (3) acquiring measurements rapidly such that non-absorbing losses are "frozen" on the timescale of the measurement, which avoids the need for more complex baseline-correction strategies [62], [91], [100]. LAS diagnostics which are successful at making measurements in harsh, high-pressure environments typically employ one or more of these strategies [1].

Diagnostics employing baseline-insensitive or, arguably, baseline-free techniques, most notably WMS-$2f/1f$, have demonstrated the ability to measure gas properties in a variety of harsh, high-pressure combustion environments such as rocket engines [95], rotating-detonation engines (RDEs) [96] and pulse-detonation combustors (PDCs) [8]. For example, three tunable-diode lasers (TDLs) and one quantum-cascade laser (QCL) were used with WMS-$2f/1f$ to measure H_2O (near 1.4 and 2.5 μm), CO (near 4.85 μm), CO_2 (near 2.7 μm), and temperature in an ethlyene-fueled PDC [8]. Measurements were collected at rates between 2 and 20 kHz at pressures ranging from 1 to 50 atm (for T_{CO}, CO and H_2O) and 1 to 12 atm (for CO_2). More recently, Bendana et al. [95] used scanned-WMS-$2f/1f$ to measure temperature and CO within a kerosene-fueled rocket combustor at pressures ranging from 25 to 80 bar, and measurements of CO were acquired up to 106 bar. Measurements were acquired using a TDL near 2.3 μm and a QCL near 4.98 μm.

Diagnostics which exploit broad spectral bandwidth to help overcome non-absorbing transmission losses have utilized both wavelength-tunable lasers with large tuning ranges (e.g., vertical-cavity surface-emitting lasers (VCSELs)) and broadband pulsed light sources (e.g., ultrafast lasers, frequency combs). For example, Sanders et al. [101] used a VCSEL to make measurements of temperature and atomic cesium in a cesium-seeded PDC. The laser was scanned across a 10 cm^{-1} spectral window which enabled measurements to be acquired at pressures as high as 33 atm. Time-division-multiplexed (TDM) Fourier-domain mode-locked (FDML) lasers were utilized by Caswell et al. [97] to acquire measurements of H_2O, temperature, pressure and velocity in an H_2-air fueled PDC. Measurements were acquired near 1.35 μm with greater than 15 cm^{-1} of bandwidth. Most recently, dual frequency-comb spectrometers which rely on a pulsed femtosecond lightsource have been used to acquire broadband absorption measurements. For example, Draper et al. [99] used a dual frequency-comb spec-

trometer with 160 cm^{-1} of bandwidth to make measurements of CH_4 and temperature near 6086 cm^{-1} inside of a rapid compression machine at pressures up to 30 bar.

Lastly, numerous direct absorption and WMS techniques have relied on acquiring measurements rapidly to effectively "freeze" non-absorbing transmission losses on the the timescale of the measurement. For example, a MEMS VCSEL capable of scanning from 1330 to 1365 nm at 100 kHz has been utilized by Rein et al. [100] to acquire high-speed measurements of temperature and H_2O within the annulus of an H_2-air RDE. In addition, Nair et al. [91] performed rapid wavelength scanning of a distributed feedback (DFB) QCL and an interband-cascade laser (ICL) at 5 μm and 4.19 μm, respectively, to measure temperature, pressure, CO and CO_2 at 1 to 3 MHz at the exit of a CH_4-O_2 fueled RDE. Soon after, Mathews et al. [102] utilized a similar QCL-based diagnostic to measure temperature, pressure, and CO at 750 kHz and a pair of TDLs emitting near 1.4 μm to measure temperature and H_2O at 1 MHz in the annulus of the same CH_4-O_2 fueled RDE. The TDLAS diagnostic relied on near-GHz scanned-WMS-$2f/1f$ to improve measurement SNR and achieve measurements at 1 MHz [103].

Recently, we have developed an ultrafast-laser-absorption-spectroscopy (ULAS) diagnostic [62] to provide multi-parameter measurements of gas temperature and species (CO, NO, CO_2, H_2O, CH_4) with sub-nanosecond time resolution [62], [79], [104]. ULAS possesses a number of attributes which make it well suited for characterizing harsh combustion environments. First, it can provide single-shot measurements with sub-nanosecond time resolution [62], [79], which is typically limited by the pulse's time of flight through the test gas. Secondly, it provides broad-bandwidth measurements which facilitates high-dynamic-range thermometry and *in situ* determination of the baseline light intensity despite the absence of non-resonant wavelengths. In this chapter, we demonstrate that these attributes enable ULAS to tolerate pronounced non-absorbing transmission losses encountered in high-pressure, multi-phase propellant flames. More specifically, we demonstrate this through measurements of temperature and χ_{CO} acquired in ammonium perchlorate (AP), hydroxyl-terminated polybutadiene (HTPB) propellant flames, both with and without aluminum, at pressures up to 40 bar.

7.2 Experimental Details

7.2.1 Wavelength Selection

Measurements of temperature and CO concentration were acquired using wavelengths from approximately 4.91 μm (2035 cm^{-1}) to 5 μm (2000 cm^{-1}). This spectral window provides access to high-energy transitions in the P-branch of CO's fundamental vibration bands. This window was chosen for three primary reasons: (1) spectral interference from H_2O, CO_2, and NO is weak at the conditions of interest, (2) it provides near-optimal absorbance levels at equilibrium conditions in lab-scale AP-HTPB flames, and (3) it provides excellent temperature sensitivity due to the presence of high-rotational-energy transitions within numerous vibrational levels [76], [79].

7.2.2 Optical Setup

A schematic of the optical setup is shown in Fig. 7.1. The laser system used in this work utilized a Ti:Sapphire oscillator (Coherent Mantis) which produced ultrashort pulses of light at a repetition rate of 80 MHz. The pulses were centered near 800 nm with an initial pulse duration of approximately 55 fs. The laser pulses were passed to a pulse shaper (FemtoJock) where they were tailored for amplification by a regenerative, multi-stage amplifier (Coherent Legend Elite Duo). The amplifier selectively amplified the pulses to an energy of 2 mJ/pulse at a repetition rate of 5 kHz. Additional amplification and conversion into the mid-IR was achieved through optical parametric amplification (OPA) and non-collinear difference-frequency generation (NDFG) processes inside a Coherent OPerA Solo module. Ultrashort mid-IR pulses with a FWHM bandwidth of 260 cm^{-1} were output from the OPerA Solo. The center wavelength of the pulses can be tuned between 2.5 and 16 μm via computer-controlled manipulation of optical elements inside the OPA module. The pulses were centered at 4.9 μm for the work presented here.

A MgF_2 Rochon-prism polarizer was used to attenuate the laser beam through adjusting the rotational position of the polarizer. Next, a spatial filter was used for the purpose of improving the spatial profile of the laser beam and reducing the beam diameter. The spatial

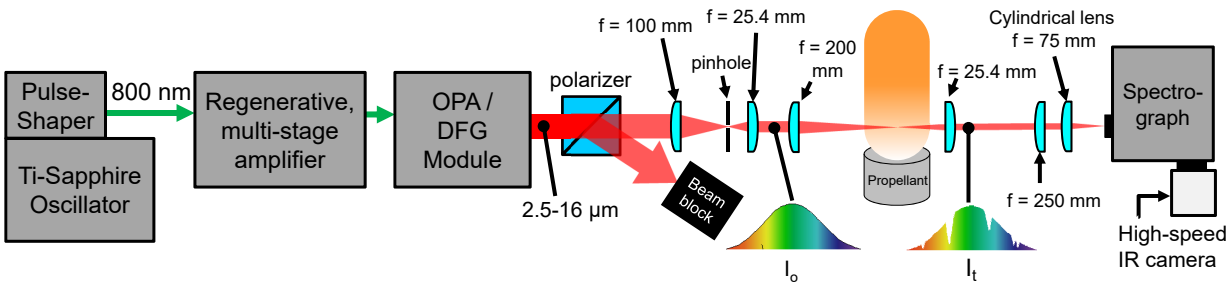

Figure 7.1. Schematic illustrating the optical setup used to characterize propellant flames with ULAS.

filter consisted of an anti-reflection (AR) coated, CaF_2, plano-convex lens with a 100 mm focal length which focused the laser-beam through a 100 μm pinhole. The beam was then re-collimated using an AR coated, Si, plano-convex lens with a 25.4 mm focal length. The $1/e^2$ beam diameter immediately downstream of the spatial filter was approximately 2 mm.

The laser beam was directed through the test gas within either a static-gas cell or propellant flame. Corrective optics (discussed at length in Sect. 7.2.3) were applied here to reduce the impact of beam steering on flame measurements which was particularly important due to the long ($\approx$1 m) path length from the flame to the spectrometer. The transmitted pulses were then focused onto the input slit of an imaging spectrometer (Andor Shamrock 500i) using a CaF_2, plano-convex, cylindrical lens with a focal length of 75 mm. The imaging spectrometer employed a reflective diffraction grating to disperse the light onto the InSb focal plane array of a high-speed, infrared camera (Telops FAST-IR 2K). In this configuration, the IR camera recorded spectral information in the x-dimension and 1D spatial information in the y-dimension. In propellant tests, single-shot spectra were averaged across the spatial dimension to improve the measurement SNR. Two diffraction gratings were used: (1) A comparatively low-resolution grating with 150 lines/mm was used to characterize high-pressure gases and (2) a high-resolution grating with 300 lines/mm was used to characterize gases at atmospheric pressure. The spectral bandwidth and resolution were $\approx$ 35 cm^{-1} and 0.6 nm, respectively, for the low-resolution grating, and 10 cm^{-1} and 0.3 nm, respectively, for the high-resolution grating.

7.2.3 Mitigation of Beam Steering

"Beam steering", refers to angular deflections of the laser beam which result from a non-uniform refractive index. In combustion gases, this results from the laser beam passing through density gradients, typically resulting from temperature varying along the beam path. Beam steering often becomes more pronounced at higher pressures due to the steeper density gradients present. Beam steering is most problematic when the distance between the steering medium and the detector is large, as is the case here. In this case a small angular deflection leads to a large translational displacement in the beam location at the detector location, as is illustrated in Fig. 7.2a. While ULAS can tolerate some non-absorbing transmission losses due to its short measurement time and broad bandwidth, severe beam steering can prevent high-SNR measurements by preventing a sufficient number of photons from being collected. In severe cases, a deflected laser beam may be entirely blocked by an aperture (e.g., the input slit of the spectrometer), thereby precluding measurements.

A lens telescope was employed as shown in Fig. 7.1 and Fig. 7.2b in order to reduce the impact of beam steering. The upstream and downstream lenses were a 200 mm focal length, CaF_2, plano-convex lens and a 25.4 mm focal length, AR-coated, Si, plano-convex lens, respectively. Additionally, a 250 mm focal length, AR-coated, CaF_2 lens was placed directly before the final 75 mm cylindrical lens. By placing the focal point of the lens telescope within the steering medium (i.e., the flame), the re-collimating lens acts to partially correct angular deflections. In this simplified picture, the steered laser beam travels on a path parallel to the original beam path (after passing through the correction lens), albeit with a small offset, which leads to a tolerable transmission loss. These concepts are illustrated in Fig. 7.2b. The smaller the focal length of the collimating lens, the smaller the offset for a given angular deflection. However, short focal-length lenses are more sensitive to beam steering which originates outside the focal point of the lens. Figure 7.2c shows the effect of beam steering on the spectrally averaged transmitted light intensity recorded by the IR camera in tests at various pressures with and without the correcting optics used to mitigate beam steering. The results show that when corrective optics were used, the average light intensity recorded by the IR camera increased by a factor of 6. The lens telescope component of the corrective

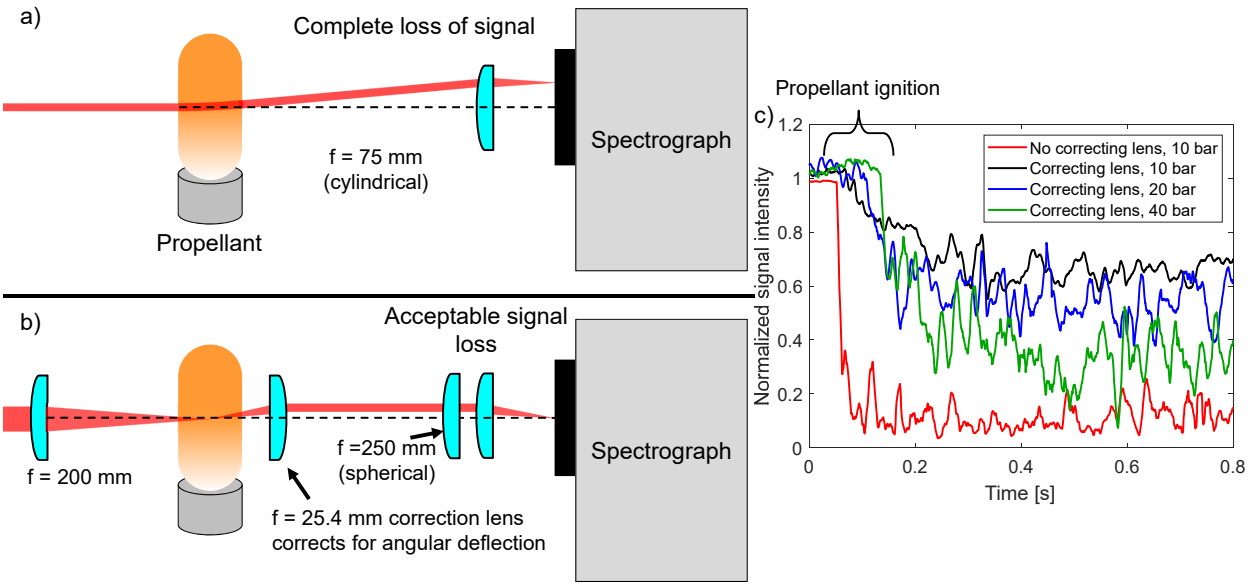

Figure 7.2. (a,b) Concept schematics illustrating the impact of correcting optics on beam steering. (a) When no correcting optics are used, beam steering leads to a large translational offset in the beam location at the measurement location, resulting in total signal loss. (b) When correcting optics are used, the translational offset in beam location at the measurement location is smaller which leads to a tolerable reduction in signal intensity. (c) Normalized, spectrally averaged light intensity as a function of time in propellant tests at various pressures with and without correcting optics. Using correcting optics significantly reduces transmission losses.

optics was only used for flame experiments, whereas the 250 mm focal length lens was used for both flame and gas-cell measurements.

7.3 ULAS Data Processing

Single-shot ULAS measurements of transmission spectra were processed using methods from previous work (described in Chapter 5 and by Tancin et al. [62], [79]) which were improved by incorporating lessons from Chapter 6. In the interest of brevity only the most pertinent details and those which differ from our prior work will be discussed here.

The measured spectral absorbance ($\alpha(\nu)_{measured}$) was obtained using Beer's law with single-shot measurements of I_t and a time-averaged measurement of I_0. Gas properties were then determined from the measured spectra by least-squares fitting simulated absorbance

spectra to measured spectra using a nonlinear least-squares fitting routine employing the Levenberg–Marquardt algorithm. The fitting routine used the following free parameters: (1) gas properties (T_{CO}, χ_{CO} and χ_{H_2O}), (2) a first-order baseline correction which accounted for shot-to-shot fluctuations in the laser intensity and broadband transmission losses, (3) the frequency of several prominent spectral features (to align the measured and simulated frequency axes), and (4) a single scaling factor on all $\Delta\nu_C$ for CO lines. The instrument broadening parameters (IRF FWHM and weight) were held fixed at the respective values determined by the multi-spectrum fitting routine described in Chapter 6 for the high-resolution and low-resolution gratings, respectively. In addition, it should be noted that a small spectral window (≈ 2.5 cm^{-1} wide) near 2017 cm^{-1} was ignored by the least-squares fitting routine due to the fact that pronounced absorption by atmospheric water precluded high-SNR measurements in this window.

Absorbance spectra of CO and H_2O were simulated using the methods described by Goldenstein et al. [16]. H_2O was included in the spectral simulations to account for weak interference within this wavelength band. Spectroscopic data for CO and H_2O were taken from the HITEMP 2019 [77] and HITEMP 2010[35] databases, respectively. The collisional FWHM of each CO transition was modeled assuming each transition was broadened by CO, CO_2, H_2O, N_2 and a single pseudo-species representing all of the remaining bath-gas species. Self-broadening by CO was modeled using the parameters (γ and n) provided by the HITEMP2019 database. The parameters describing CO_2-, N_2- and H_2O-broadening of CO were taken from Hartmann et al. [90]. Collisional-broadening by the remaining species in the flame bath gas was modeled using the parameters provided by the HITEMP 2019 database for air broadening. This approximation is justified for CO since the majority of the remaining bath-gas species are diatomics which are not expected to posses radically different broadening coefficients [91]. Calculations of collisional FWHM were performed assuming that the mole fractions of CO_2, N_2 and H_2O were equal to those predicted by HP equilibrium calculations performed using NASA Chemical Equilibrium and Applications (NASA-CEA) [105]. Broadening of H_2O lines was modeled using only air and self broadening parameters supplied by HITEMP 2010 due to their minor contribution to the spectra.

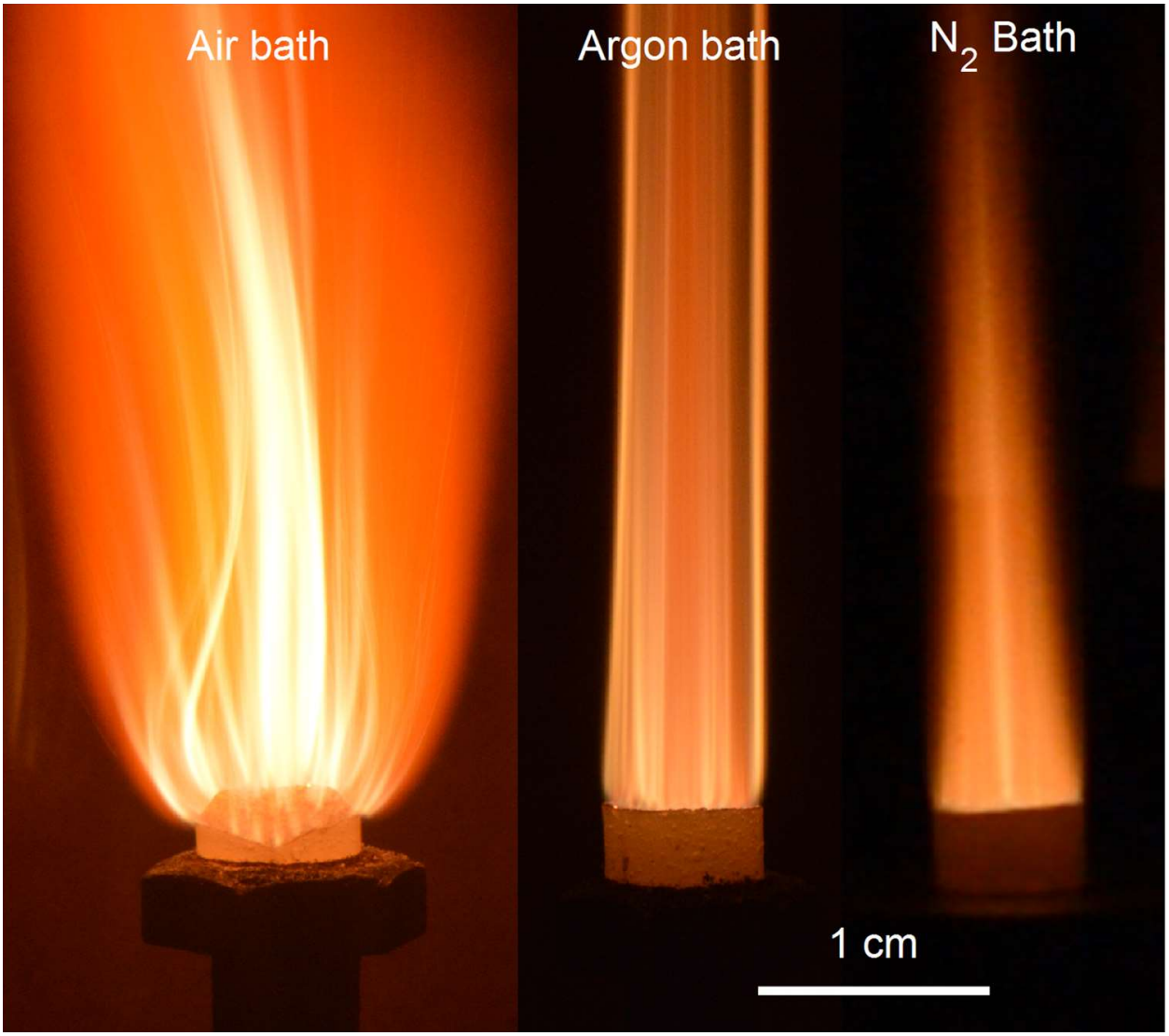

Figure 7.3. DSLR images of laser-ignited AP-HTPB propellant flames burning in air, argon and nitrogen bath gases. Images were taken with identical exposure settings to allow for comparison of flame luminosity at different conditions.

7.4 Propellant Tests

The ULAS diagnostic was used to characterize AP-HTPB propellant flames both with and without aluminum. The particle size of AP was distributed bimodally with mean diameters of 200 μm and 20 μm in a coarse-to-fine ratio of 4:1. On a mass basis, the binder consisted of 76.33% HTPB with 15.05% isodecyl pelargonate as the plasticizer, and 8.62%

modified MDI isocyanate as the curative. In cases where aluminum was added, Valimet H-30 aluminum with a mean particle diameter of 31 μm was used. The AP-HTPB propellant consisted of 80% AP by mass, whereas the AP-HTPB-Al propellant was 68% AP, 15% aluminum and 17% binder by mass. The propellant was cast into plastic tubes and cured for a minimum of 3 days at room temperature. Tests were performed using 4 to 6 mm tall propellant strands with a 7 mm diameter.

The strands were ignited using a CO_2 laser emitting near 10.6 μm. The laser delivered an optical intensity of 38 W/cm^2 to the surface of the strand. The data acquisition system was triggered 100 ms prior to the CO_2 laser turning on, to allow for I_0 to be recorded. The CO_2 laser was turned on for 200 ms (400 ms was used at 1 bar) to ignite the strand. Video of each test was recorded with the DSLR camera, to ensure that ignition and burning of each strand was uniform, and to provide an estimate of the absorbing path-length. The propellant flames reached a quasi-steady state approximately 100 ms after ignition. Figure 7.4 shows images of the propellant flames acquired using a Nikon D3200 DSLR camera. With the exception of the 1 bar case, each image was taken with identical exposure settings (1/4000 s shutter speed, ISO 200 and F22 f-stop) to allow for direct comparison between different conditions. At 1 bar, the propellant flames were less luminous so the following camera settings were used to maintain proper exposure: 1/200 s shutter speed, ISO 800 and F22 f-stop.

All propellant tests were conducted using a high-pressure combustion chamber, the design of which is described in detail by Tancin et al. [6] and in Chapter 3. Optical access for the ULAS diagnostic and DSLR camera was provided by a pair of slot-shaped sapphire windows with a clear aperture of 10 cm x 4 cm in the vertical and horizontal dimensions, respectively. The CO_2 laser beam was directed into the vessel through a ZnSe window at the top of the chamber. The propellant was placed on a small vertical-translation stage located in the center of the chamber so that the measurement location relative to the strand surface could be accurately controlled. The laser beam was aligned through the center line of the flame for all tests. For the characterization of bath gas effects, measurements were acquired at vertical locations of 2 mm, 2 cm and 4 cm relative to initial surface location of the propellant strand. For data acquired at higher than atmospheric pressures, measurements were collected at a vertical location 2 mm above the initial surface of the propellant in the case of non-aluminized

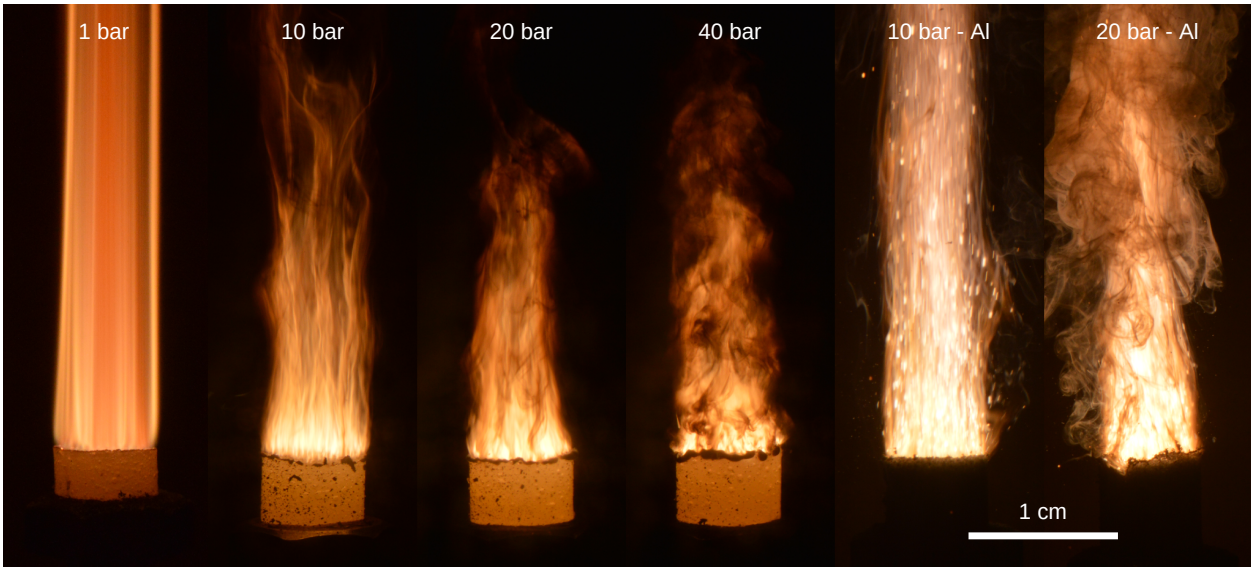

Figure 7.4. DSLR images of laser-ignited AP-HTPB propellant flames, both without (left four panels) and with (right two panels) aluminum. Images were taken with identical exposure settings (except for the test at 1 bar) to allow for comparison of flame luminosity at different conditions.

propellant strands, and 1 cm in the case of aluminized propellant strands. Prior to each test, the chamber was evacuated using a vacuum roughing pump before being pressurized with the appropriate bath gas. AP-HTPB propellant was characterized at atmospheric pressures in air, argon and nitrogen baths. All tests at above-atmospheric pressures were conducted in argon bath gases. The pressure during each test was measured using the same Unik-5000 pressure transducer as was used for the static-gas cell measurements. A time history of pressure was recorded during each test so that a linear regression could be fitted to each pressure trace allowing the data processing routine to use an updated pressure for each subsequent laser shot. The gas pressure increased by ≈0.6 bar during each test. For tests at atmospheric pressure, the HPCC vent valve was partially opened immediately prior to the test, such that no pressure rise was observed during the test.

7.5 Results and Discussion

7.5.1 Characterization of Bath Gas Effects on Propellant Combustion

The improved ULAS diagnostic incorporating the results of the multi-spectrum fitting routine were first applied to characterize the effect of bath gas on laser-ignited propellant flames. As previously mentioned, T_{CO} and $\chi_{CO}L_{abs}$ (or χ_{CO}) were measured at locations of 2 mm, 2 cm, and 4 cm relative to propellant surface. Time-histories of single-shot T_{CO} and $\chi_{CO}L_{abs}$ measurements acquired at 2 mm above the surface of the propellant strand in an argon bath gas are shown in Fig. 7.5a. Further, representative measured and best-fit absorbance spectra from the same data set are displayed in Fig. 7.5b. The best-fit spectrum agrees well with the measured data, with no observable systematic disagreements between the measured- and best-fit spectra. The baseline level of noise in absorbance had a 1-σ value of 0.00287, which was consistent across bath gas and measurement location.

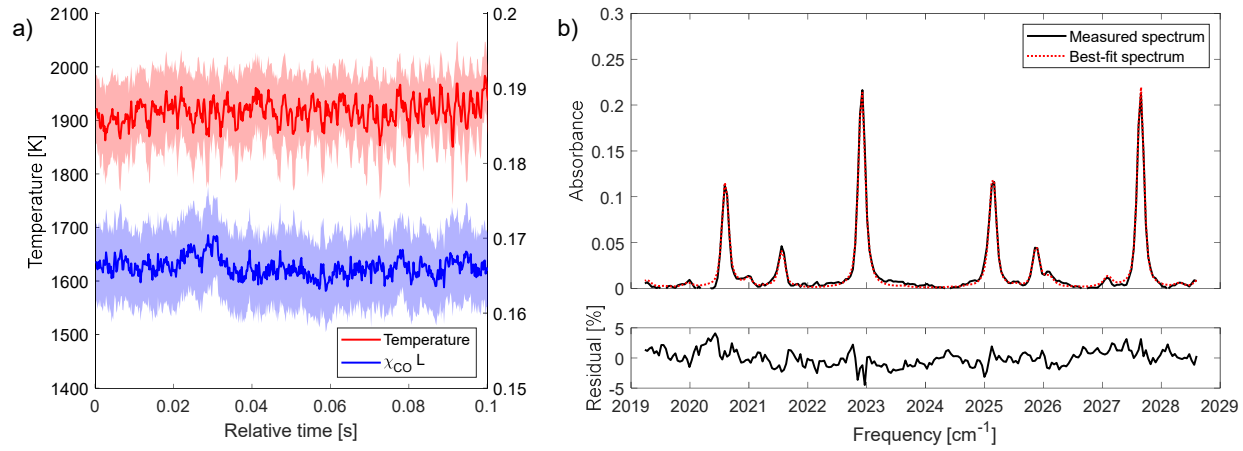

Figure 7.5. Measurement time-histories and measured and best-fit absorbance spectra acquired in an AP-HTPB propellant flame in an argon bath at 1 bar. The measurement line-of-sight was 2 mm above the surface of the propellant prior to ignition. (a) A sample of the measurement time histories for temperature and column density ($\chi_{CO}L_{abs}$) acquired during steady state burning, with shaded regions representing the respective 95% confidence intervals for temperature and $\chi_{CO}L_{abs}$. (b) Representative measured and best-fit absorbance spectra acquired in the AP-HTPB propellant flame.

There existed some unstructured variation in measured gas properties with time, likely due to a combination of the diagnostics's precision and real variations in gas properties along

the measurement line-of-sight. The 1-σ variation of temperature measurements exhibited no significant correlation between tests of the same bath gas or measurement location. The average 1-σ variation across tests was 28.5 K with high and low values of 43.8 K (air bath at 2 cm) and 19.3 K (nitrogen bath at 2 cm), respectively. Likewise, no correlation in 1-σ variation was observed between bath gases or measurement location when normalized by the mean value. On average, temperature measurements exhibited 1-σ variations of 1.5% of the measured value. 95% confidence intervals for temperature measurements (calculated by adding relative uncertainty in fit to relative uncertainty in instrument broadening in quadrature) were consistent across tests, with 95% confidence that the true temperature, on average, lies within 75 K of the measured value.

The measured time histories for $\chi_{CO}L_{abs}$ were observed to have low frequency variations, which increased with measurement height, for all bath gases. This is likely due to flame "wagging" which becomes more pronounced with height. The low-frequency instabilities were accounted for by subtracting off a 10-point moving average from the measurement time-histories, allowing for the 1-σ precision to be calculated. The observed 1-σ precisions in $\chi_{CO}L_{abs}$ were consistent across both of the inert bath gases, for all measurement heights with an average value of 0.0015. This corresponded to $\approx$ 0.9% of the measured value. 1-σ precisions for the air-bath-gas case were consistently higher than the other bath gases, but didn't vary significantly with height, with a mean 1-σ precision of 0.0034, corresponding to $\approx$ 1.84 % of the measured value. On average, the 95% confidence intervals for $\chi_{CO}L_{abs}$ (calculated in the same manner as the temperature time histories) were larger for air, than for the inert bath gases, with values of 0.008 in air and 0.004 in argon or N_2.

Time-averaged values for temperature are shown in Fig. 7.6a. The value for T_{CO} in air at 2 mm agrees well with the predicted equilibrium value of $\approx$ 2400 K [106] and with prior work in our lab [107]. Measurements of T_{CO} in air report much greater temperatures than for either of the cases in inert bath gases. An explanation for this, is that CO is being continuously oxidized in the boundary layer of the product gas plume.

Time averaged values for $\chi_{CO}L_{abs}$, χ_{CO} and T_{CO} are presented in Fig. 7.6. The absorbing path length for χ_{CO} measurements presented in 7.6c was determined from DSLR videos which were synchronized with the measurement time histories. The error in path length determined

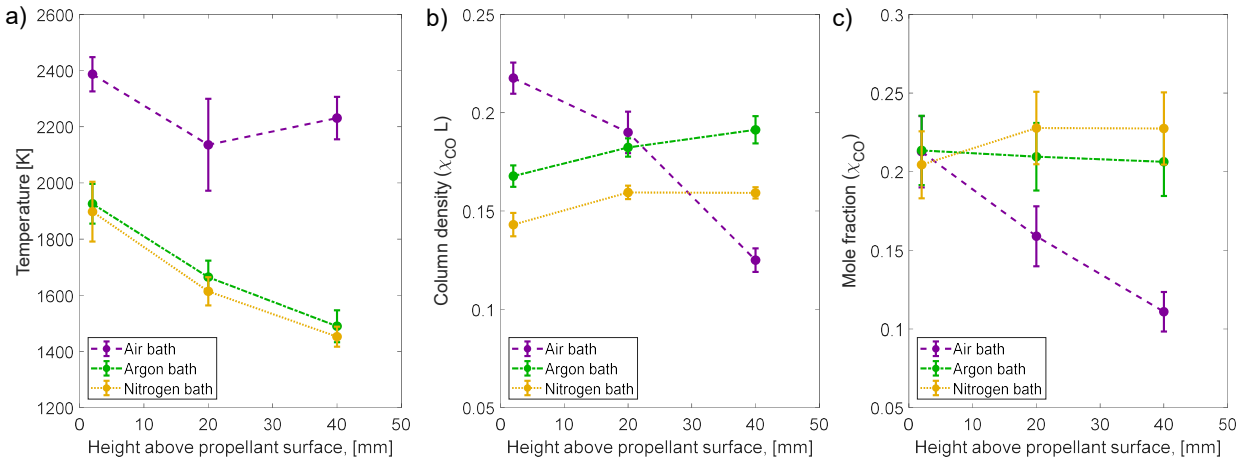

Figure 7.6. Time-averaged temperature (a), column density (b), and mole fraction (c) measured at 2 mm, 2 cm and 4 cm above the propellant surface in AP-HTPB flames. Data was acquired for air, argon and nitrogen bath gases, all at 1 bar of pressure. The measurement location relative to the propellant surface was determined prior to ignition.

though this method was assumed to be 10%, and accounted for the majority of uncertainty for the χ_{CO} measurements. Values of χ_{CO} acquired 2 mm above the burning surface agree well with the predicted equilibrium value of 0.22 [106]. χ_{CO} in nitrogen bath gas was higher than the predicted value for measurements 2 cm and 4 cm above the burning surface. This is likely due to under-predicting L_{abs} due to the low luminosity of the flame's periphery for these tests, which is illustrated in Fig. 7.3.

Time-averaged column density as a function of height is reported in Fig. 7.6b. Measurements (shown in Fig. 7.6b) were significantly higher for air, 2 mm above the measurement location compared to the inert bath gas cases. This was likely the result of edge burning, resulting in a thicker flame (i.e., larger L_{abs}). This is supported by DSLR images from the tests seen in Fig. 7.3 which show edge burning for the air bath gas test, and planar burns for both of the inert bath gas tests. As height increases, $\chi_{CO}L_{abs}$ decreases sharply in the air case, due to oxidation of CO in the boundary layer. With inert bath gases, $\chi_{CO}L_{abs}$ increases slightly, which is likely due to the flame becoming slightly thicker as the product gases slow.

The hypothesis that CO is being oxidized in the periphery of the product gas plume is supported by the literature ([79], [107]–[110]), work discussed in Chapter 5 and the analysis of this dataset discussed next.

1. The temperature measurements presented here are obtained from path-integrated spectra and, thus, are susceptible to the influence of non-uniform temperature distributions. As the bath gas mixes and diffuses with product gases in the flames periphery, incomplete combustion products (e.g., CO) are further oxidized by air, releasing additional energy, but more importantly, consuming the CO which would otherwise be present in this relatively cooler area of the flame. Hence, it would be expected that in the air bath gas case that the temperature would be hotter and vary less with height compared to the inert bath gas cases, which is what is shown in Fig 7.6a, and is further supported from prior work presented in Chapter 5.2 and the literature [79].

2. The consistently higher temperatures measured in argon compared to nitrogen (seen in Fig. 7.6a) are consistent with the fact that the bath gas is mixing with and cooling the flame's periphery. It is expected that a nitrogen would quench product gases more efficiently, and thus yield a lower flame temperature because nitrogen has a higher specific heat capacity compared to argon.

3. The luminosity of AP-HTPB flames was observed to be greatest in air bath gases and lowest in nitrogen bath gases which is shown by the DSLR images in Fig. 7.3. The reduced luminosity of the nitrogen case compared to the argon case is consistent with a larger quenching effect. The greater luminosity in the tests conducted in air is likely due to the greater flame thicknesses caused by edge burning.

4. Oxidation of CO in tests conducted in an air bath gas is directly observable by the downward trend in χ_{CO} with height reported Fig. 7.6c. As expected, χ_{CO} is stable with height for tests in inert bath gases.

7.5.2 Characterization of AP-HTPB Propellant Flames at High-Pressures

This section presents results acquired in laser-ignited AP-HTPB flames both with and without aluminum. Figure 7.7 shows measured time histories of T_{CO} and χ_{CO} as well as representative examples of measured and best-fit spectra. The spectra illustrate the high SNR of the measurements and, for all data sets, significant wavelength-dependent structure was not observed in the residuals between measured and best-fit spectra, thereby supporting the accuracy of the spectroscopic model employed. The 1-σ precision of the baseline noise level in absorbance was 0.006, 0.007 and 0.01 for the results shown in Fig. 7.7b, 7.7d and 7.7f, respectively.

All of the time histories (see Fig. 7.7a,c,e) exhibit some unstructured variation in time, consistent with mild to moderate unsteadiness in general flame structure which was observed in visual imaging of the flames (e.g., see Fig. 7.4). In the non-aluminized propellant flames, there is a strong correlation between the amplitude of the time variation and the nominal pressure. For example, measurements of temperature exhibited a 1-σ variation of 22 K, 75 K, 73 K and 100 K at pressures of 1, 10, 20, and 40 bar, respectively. Similarly, the 1-σ variation in $\chi_{CO}L_{abs}$ was 0.0012, 0.011, 0.015, and 0.017 for pressures of 1, 10, 20, and 40 bar, respectively. When accounting for the time-variation in gas properties (through subtracting the data from a 10-point moving average), the 1-σ precision in T_{CO} at 1, 10, 20 and 40 bar were found to be 0.9%, 0.4%, 0.6%, and 1.6% of the measured value, respectively. Likewise, the 1-σ precision values for $\chi_{CO}L_{abs}$ were, 0.45%, 0.9%, 1.3%, and 3.65% at 1, 10, 20, and 40 bar, respectively. In the aluminized propellant flames, the temporal variation of gas properties was more pronounced. The 1-σ variation in temperature was 93 K and 127 K at 10 and 20 bar, respectively. Similarly, the 1-σ variation in $\chi_{CO}L_{abs}$ was 0.015 and 0.022 at 10 and 20 bar, respectively. Like the non-aluminized cases, these measurements were also obtained with high precision. For temperature, the 1-σ precision after accounting for time-variation in gas properties was 0.83% and 0.91% at 10 and 20 bar, respectively. The 1-σ precision for $\chi_{CO}L_{abs}$ was 1.38% and 2.0%. These trends are consistent with the development of increasingly stratified flames as pressure was increased which was observed through visible imaging. Encouragingly, non-absorbing transmission losses did not appear to be exacerbated

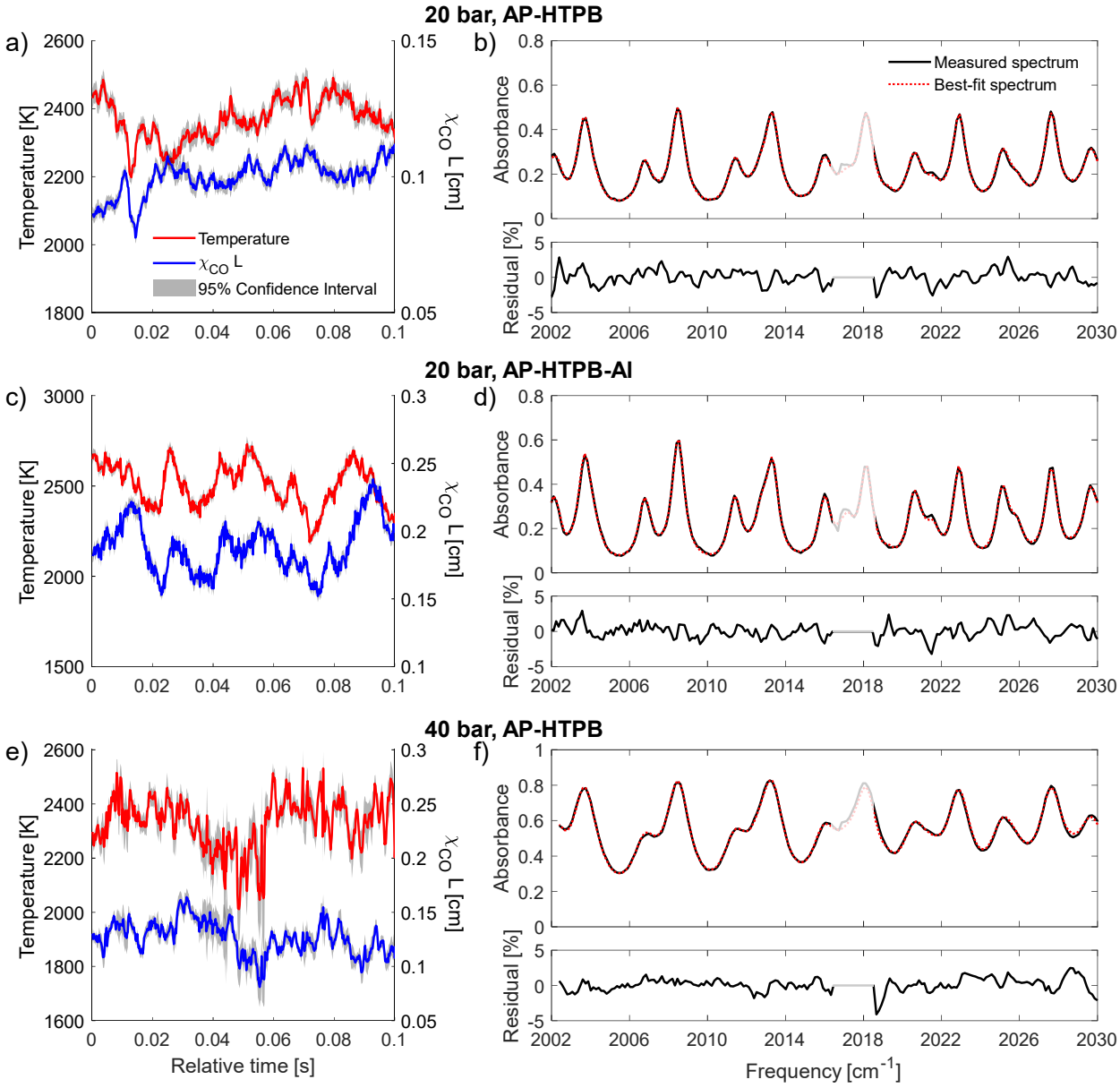

Figure 7.7. Samples of measured time histories of temperature and χ_{CO} (a, c, e) as well as representative measured and best-fit absorbance spectra of CO with residuals (b, d, f) acquired in propellant tests. Panels a) and b) display results acquired 2 mm above the burning surface of the AP-HTPB propellant at 20 bar. Panels c) and d) display results acquired 1 cm above the burning surface of the Al-AP-HTPB propellant at 20 bar. Panels e) and f) display results acquired 2 mm above the burning surface of the AP-HTPB propellant at 40 bar. The shaded out portion of the spectra was ignored by the spectral-fitting routine due interfering absorption by H_2O in the ambient air outside the combustion chamber.

by the addition of aluminum into the propellant. This suggests that particle scattering and attenuation does not have a significant impact on the transmitted light intensity in these flames.

A notable result is that the time variation in both temperature and χ_{CO} increased with pressure as is illustrated by Fig. 7.7a and 7.7e. A likely cause for this is the increased burning rate of the propellant at elevated pressures [106], [111] along with the increased gas density which may lead to rapidly changing gas conditions along the measurement line-of-sight. This is supported by Fig. 7.4 which shows that as pressure increases, the flames appear more heterogeneous. This effect is exacerbated through the addition of aluminum into the propellant. Product gas plumes of aluminized propellants are inherently heterogeneous environments, with widely varying gas properties due to burning droplets of molten aluminum [107], [109]. As such, these effects are likely responsible for the increased time-variations in T_{CO} and χ_{CO}.

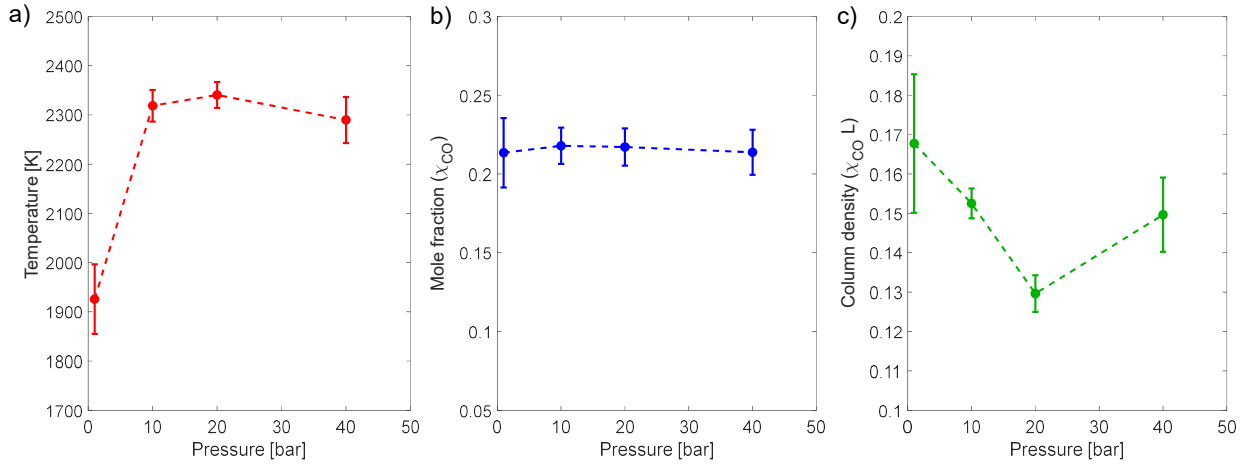

Figure 7.8. Time-averaged temperature (a) and χ_{CO} (b) and $\chi_{CO}L_{abs}$ measured 2 mm above the propellant surface in AP-HTPB flames. The uncertainty bars represent the 95% confidence interval, which took into account uncertainty in instrument broadening parameters and uncertainty of the best fit spectra due to measurement noise. Additionally, 5% uncertainty was used for the estimation of absorbing path length for χ_{CO} measurements.

Figure 7.8 shows results for the time-averaged values of temperature and χ_{CO} at a measurement location 2 mm above the burning surface of the AP-HTPB propellant at each test condition. The measured temperature generally increased with increasing pressure, with the

largest temperature rise occurring between 1 and 10 bar which is consistent with predictions from HP equilibrium calculations. In comparison, pressure did not have a detectable impact (i.e., greater than measurement uncertainty) on CO concentration. The average value of χ_{CO} was near 0.22 for all cases. This trend, or more accurately lack thereof, in CO concentration with pressure is also supported by HP equilibrium calculations.

It is interesting to note that HP equilibrium calculations predict a 50 K increase from 2417 K to 2468 K in the equilibrium flame temperature between 1 and 10 bar, and an approximately 15 K increase between 10 and 40 bar. In contrast, the measurements indicate that the flame temperature increases by a larger amount, ≈375 K, between 1 and 10 bar. This may result from the fact that at 1 bar the flame gas (originating from AP-HTPB diffusion flames) may not have fully reached equilibrium by 2 mm above the burning surface. Further, it is important to note that the measurements are path-integrated which may partially explain why the measured temperatures at 10 to 40 bar are ≈150 K below that predicted by HP equilibrium [107]. Incomplete combustion (as evidenced by significant soot production, see Fig. 7.4) and heat loss to the surrounding bath gas may also partially explain this difference.

7.6 Conclusions

This section presented the first application of ULAS for studying high-pressure combustion gases. ULAS measurements of T_{CO} and χ_{CO} were acquired in AP-HTPB composite-propellant flames at pressures up to 40 bar. Additionally, measurements of T_{CO} and χ_{CO} were acquired in aluminized, AP-HTPB propellant flames, representing some of the first ULAS measurements in multi-phase combustion gases. These propellant flames, both with and without aluminum, represented a challenging test environment for the application of LAS due to the high pressures and long optical path lengths (order of 1 m to spectrometer) required. Ultimately, this led to non-absorbing transmission losses of up to 90%, however, ULAS was still able to provide high-fidelity measurements due to its broad spectral bandwidth and short (sub-nanosecond) measurement time. The results suggests that the addition of 15% aluminum and, presumably, other metals into the propellant mixture does not sig-

nificantly effect the performance of the diagnostic, thereby paving the way for future studies of metallized-propellant flames at rocket-motor-relevant pressures.

8. PURDUE HIGH-PRESSURE SHOCK TUBE

8.1 Introduction

Shock tubes are useful tools for studying spectroscopy, chemistry and fluid dynamics as well as aiding in the development of optical diagnostics. A shock tube is a device that consists of a long, enclosed tube which is divided into a driver and driven section by a diaphragm (see Fig. 8.1). The driver section is filled with a high-pressure gas and the driven side with a comparatively low-pressure gas which is to be studied. The pressure in the driver section is raised until the diaphragm bursts, creating a shock wave which propagates down the driven section and reflects off the endwall creating a region of stagnant, high-temperature, high-pressure gas, which is often the condition of interest.

The advantages of shock tubes will be discussed in this chapter from the vantage point of LAS-based diagnostics and the study of combustion and high-temperature non-equilibrium. There are two key benefits shock tubes can provide towards the development of LAS diagnostics which will be discussed. (1) Shock tubes enable validation measurements at a wide range of temperatures, pressures and gas compositions which are not possible with other experimental apparatus (e.g., heated gas cells). (2) Shock tubes offer the ability to acquire absorption cross sections at a wider range of gas conditions. (3) The near instantaneous creation of test conditions mitigates many of the challenges associated with characterizing ignition delay times, reaction rate coefficients, non-equilibrium, chemistry or, more generally, gases at extreme temperatures [112]–[116].

Shock tubes are ideal for validation of LAS diagnostics because they are capable of generating a wide range of uniform gas conditions not possible with rapid-compression machines or heated gas cells (i.e., high temperatures) due to material limitations [1], [117], [118]. High uniformity of gas conditions can be expected, given a sufficiently large internal diameter (i.e., > 10 cm), minimizing the influence of LOS non-uniformities on LAS measurements. Further, the temperature of the gas mixture can be reliably predicted to within $\pm$ 1% through shock jump equations employing measured shock speeds. Temperatures in excess of 3000 K are routinely created [4], [115], [116] with temperatures at some facilities reaching as high as 20,000 K [119] at a variety of pressures.

Shock tubes facilitate measurement of absorption cross sections at a variety of temperatures, pressures and mixtures which are vital for high-temperature spectroscopic measurements. While many combustion relevant molecules (e.g., H_2O, CO, CO_2, NO, OH) have existing spectroscopic databases for line parameters, many larger molecules do not. Further, existing databases often have shortcomings, especially at extremely high temperatures (e.g., $T > 5000$ K). Hence, a lookup table of absorption cross sections is often fitted to measured data to extract gas properties in laser-absorption experiments. One of the reasons larger molecules lack spectroscopic databases is that the highly "crowded" lines yield a blended spectra making the measurement of spectroscopic parameters difficult. The absorption cross sections of many large molecules are available, such as those archived by NIST [120] and PNNL [121]. These cross sections, which were acquired using FTIR, are limited to relatively low temperatures because the absorbing molecules begin to break down at high-temperatures. Shock tubes mitigate this challenge through heating the gas near instantaneously, allowing for measurement of an absorption cross section before the molecules begin to decompose [67], [122]–[124]. While many existing databases are extensive, there are countless combinations of cross sections for different molecules, gas conditions, spectral ranges and collision partners, so the appropriate cross-section may be difficult to find or not currently exist [1], [125].Thus, a shock tube in the lab can enable the creation of new absorption cross section databases when needed, making them crucial in enabling measurement of large molecules in flames.

Lastly, shock tubes enable the study of interesting physical phenomena which would be otherwise be difficult or impossible to study. For example, the ability of shock tubes to generate high-temperature conditions near instantaneously makes them ideal for measuring reaction rate constants [112], [113] and ignition-delay times [117], [126], [127]. Heated-gas cells, and to some extent rapid compression machines, create high temperatures relatively slowly, allowing time for reactions to progress before reaching the target temperature and therefore introducing uncertainty into the measurements [1]. Further, gases can be studied at extreme conditions (e.g., 1000 atm and/or 10,000 K) in shock tubes [114], [115], [128]–[130] which facilitates the study of, chemical dissociation, non-equilibrium spectroscopy and

radiative heat transfer at conditions relevant to atmospheric entry or behind strong blast waves.

8.2 Shock-Tube Fundamentals

A schematic of a typical shock tube experiment is shown in Fig. 8.1a-d. A typical experimental sequence is as follows:

1. A diaphragm is placed between the driver and driven sections, and the two sections are sealed together. The tube is then evacuated with a vacuum pump. (Fig. 8.1a)

2. The driven section is filled with the test gas of interest. The driver is filled with a relatively high-pressure gas (commonly helium). (Fig. 8.1b)

3. The pressure differential across the diaphragm causes it to burst, sending an incident shock wave down the driven end of the tube towards the test section, and an expansion

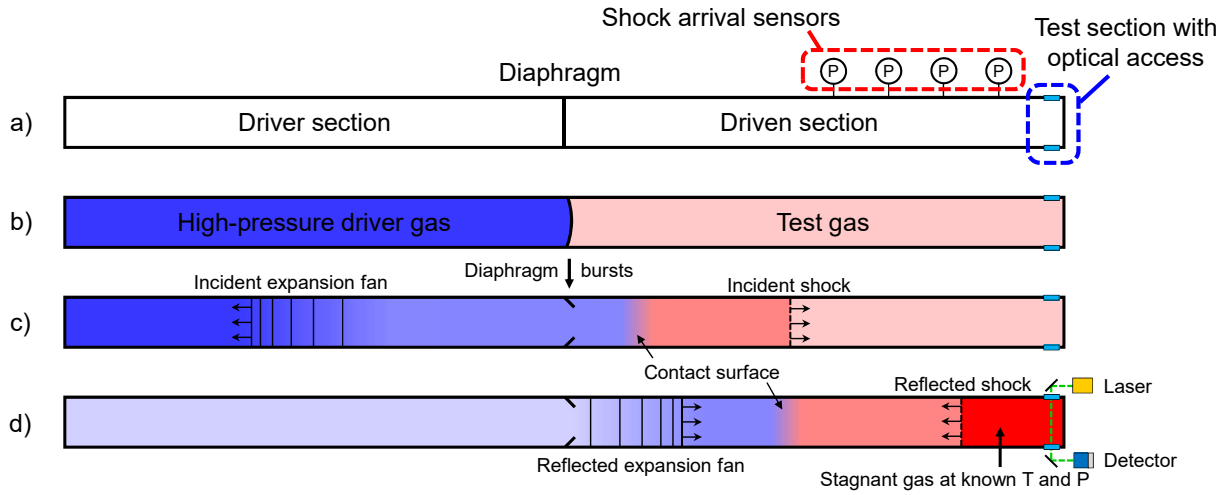

Figure 8.1. Overview of the stages of a typical shock tube experiment. a) The driver and driven sections are evacuated. b) The driven section is filled with a test gas and the driver is pressurized until the diaphragm bursts. c) The bursting diaphragm sends an incident shockwave towards the driven endwall , and an expansion fan towards the driver endwall. d) The incident shock wave hits the driven endwall and reflects, leaving stagnant, high-temperature and high-pressure gas in its wake.

fan down the driver towards the driver endwall. Shock arrival sensors are used to calculate the shock speed, allowing for calculation of gas properties behind the shock wave. (Fig. 8.1c)

4. The expansion fan and the incident shock wave reflect off the driver and driven endwalls, respectively. The reflected shock heats, compresses, and stagnates the driven gas. The test time usually begins when the reflected shock passes the measurement location. (Fig. 8.1d)

5. The test-time often ends when the leading edge of the reflected expansion fan arrives at the measurement location (determined by a pressure transducer), as the temperature can no longer be precisely known.

A useful way to visualize the spatiotemporal evolution of gas properties during a shock tube experiment is with an x-t diagram. An x-t diagram, such as shown in Fig. 8.2, illustrates the position (x-axis) of important test elements (e.g., shock wave locations) or gas properties as a function of time (y-axis). Fig. 8.2 also labels important nomenclature, notably, gas states. The most relevant states are defined as follows:

State 1: Condition of the driven gas prior to bursting of the diaphragm or arrival of the incident shock.

State 2: Condition of the driven gas behind the incident shock.

State 3: Condition of the driver gas behind the incident expansion fan.

State 4: Condition of the driver gas prior to arrival of the expansion fan or prior to the bursting of the diaphragm.

State 5: Condition of the driven gas behind the reflected shock. In most cases, this is the condition of interest, and the duration of state 5 at the measurement location defines the test time.

State 6: Condition of the driver gas behind the reflected expansion fan.

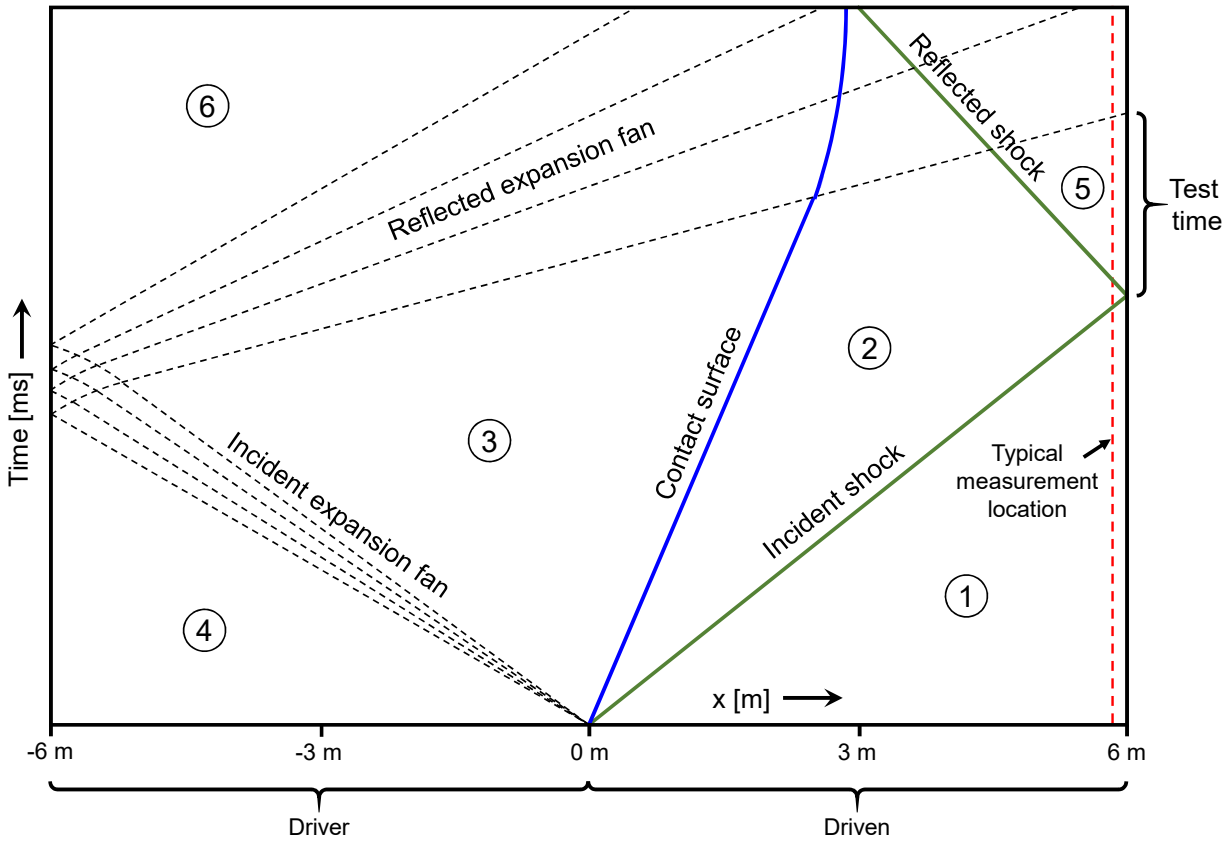

Figure 8.2. An example of an x-t diagram for a typical shock-tube experiment. The driver and driven lengths are representative of the Purdue HPST. The notation for the various gas states are labeled throughout the diagram, as is the test time.

8.3 Facility Overview

The Purdue high-pressure shock tube (HPST) is 12.6 m in total length, consisting of a 6.6 m driven section, a 3 m driver and an additional 3 m driver extension for extended test times. When extended test times are not needed, shorter drivers are typically used to reduce the consumption, and therefore cost, of driver gas. It is capable of pressures of 280 bar and temperatures exceeding 10,000 K. The tube has an internal diameter of 10.3 cm which enables line-of-sight measurements to be conducted with minimal influence from boundary layer effects [4]. Optical access is provided by 6 ×2.5 cm diameter windows with a clear aperture of 2 cm (i.e., 3 ×LOS) located 8.5 mm from the test-section endwall. A pair of 2.5 cm ×6.4 cm slot shaped windows provide a 1.9 cm ×5.7 cm clear aperture line-of-sight

at the same axial location as the round windows. An additional pair of 1.3 cm diameter windows provide a 1 cm clear aperture LOS located 0.28 m from the test-section endwall. An injection port is located 1 m from the test section which can be used to seed the flow with powdered materials (e.g., energetic materials) or aerosols to enable their study at high temperatures and pressures.

8.4 Shock Tube Design

8.4.1 Tube Sections

Sections of the shock tube were fabricated from 5.5 inch OD tube made from 304 (also known as A2 or 18-8) stainless steel. Making the tube sections from commercially available tubing, greatly reduced machining time and therefore cost. Tubing was chosen over pipe of a similar size, because tubing is typically manufactured to tighter ID and OD tolerances, making the final dimensions less dependent on manufacturing variability. The tubing needed to be sized according to two design criteria. (1) The entire tube should be capable of pressures ≥ 250 bar to allow for either high-pressure test conditions (P_5) or high driver pressures (P_4) for generating strong shock waves. The tubing should be able to handle these pressures while maintaining a minimum safety factor of 2. (2) The internal diameter of the tube should be ≥ 10 cm, to allow for high-fidelity line-of-sight measurements which are minimally affected by boundary layer effects.

While the Lamé Equations for thick walled pressure vessels are commonly used to design shock tubes [131], they were not in this case because the stresses these equations calculate (hoop, radial, and axial) were not the limiting factor of the design. Stress concentrations due to access ports or other connections determined the pressure rating of the tube, and these are best determined using FEA software due to their comparatively complex geometry. Tubing with a 5.5" OD and a wall thickness of 0.75" satisfied the design requirements, allowing for a maximum pressure capability of 280 bar with a 10.3 cm ID after honing and polishing of the tube bore. The length of the tube sections were maximized in order to minimize the number of connections needed, thus reducing the number of components and seals. Tube

lengths were constrained to a maximum length of 3.05 m (120 in), set by the dimensions of the freight elevator in the mechanical engineering building.

The surface finish of the internal diameter of the tubes is critical to minimizing the thickness of the boundary layer, and thus minimizing non-ideal effects on the measurements. To minimize friction between the gas and the tube wall, the inside of all tube sections was honed to a surface roughness of 32 μin (0.8 μm or ISO grade N6). This was done with all components assembled (e.g., access ports, window holders, etc.) so that the honing process could smooth any mismatches between a component and the tube's inner bore. To further refine the inner surface, the components were electropolished.

8.4.2 Tube Connections

Flanged connections are typically used to join shock tube sections and other inline components (those which are concentric, or inline, with the shock tube bore, e.g., test section, poppet valve, etc.). Most shock tubes employ standardized flanges such as those in the ASME/ANSI B16.5 Pipe Flanges and Flanged Fittings standard. However, the HPST employs a custom weldless flange design. Similar designs have been employed by other shock tube facilities [132], [133], which inspired the design for the flanges of the HPST.

Using standardized flanges reduces the engineering design time, and eliminates the time and cost of machining a custom part since they are commercially available. However, standardized flanges have a number of drawbacks. First, they typically need to be welded to the tube sections which risks warping the tubes due to the high heat involved. Additionally, some type of weld inspection may be needed to ensure proper weld penetration. Standardized flanges also tend to be massive and bulky. This is best illustrated with a simple analysis of the blind-flange connection at the end of the driver. A standard 5" nominal, class-1500 blind flange and weld neck flange would have a diameter of 37.5 cm, weigh $\approx$ 124 kg, and require 8 $\times$1.5" diameter bolts. Using the custom weldless flange design, the same is achieved with a diameter of 20.3 cm, a mass of 16 kg and 12 $\times$5/8" diameter bolts. The standard flange design was rejected because the increased weight meant that heavier equipment would be needed to install the tube sections, and mechanical assistance would be needed to open the

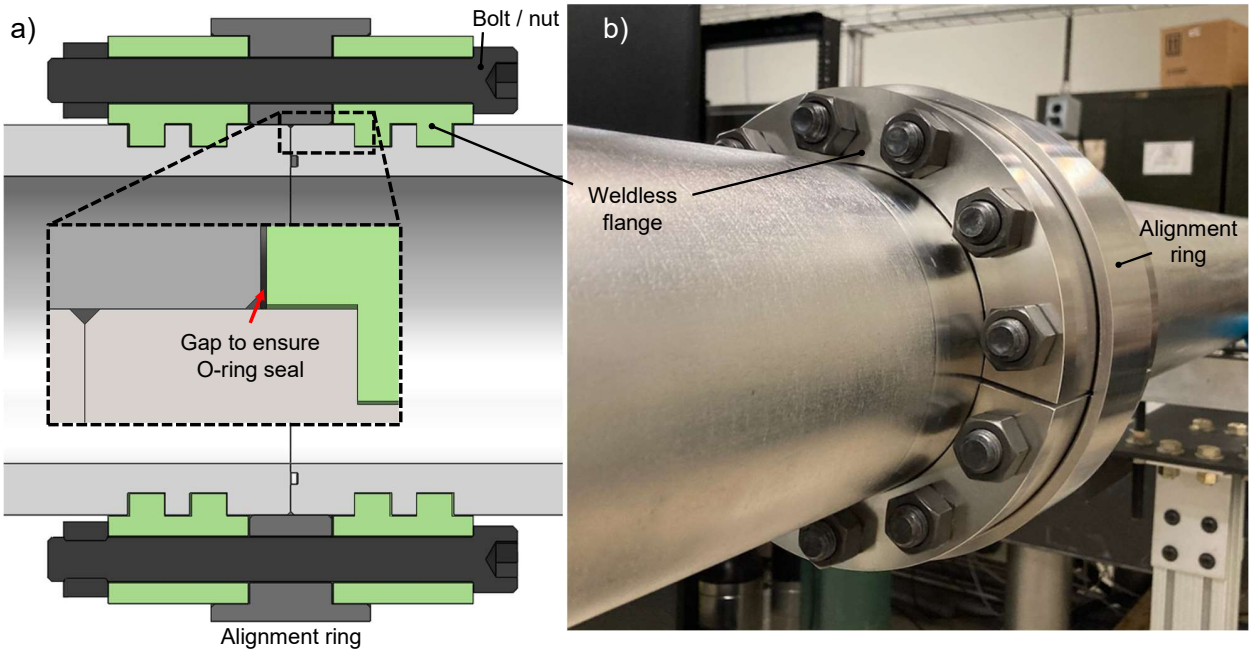

Figure 8.3. Weldless flanges connecting the driver to the driver extension of the HPST. a) CAD cross section along the shock tube's axis, detailing the weldless flanges. b) View of the weldless flange connection showing the split flange design which allows for assembly of the bolted connection.

tube to change diaphragms between tests. In addition, the increased cost of machining for custom flanges is offset by the decreased material mass compared to standard sized flanges, making both designs approximately equal in price.

The final design of the custom weldless flanges is detailed in Fig. 8.3. Each flanged connection consists of a pair of grooves machined into the OD of the tube section which mate with a pair of "teeth" machined on the ID of the flange. Each flange consists of 2 halves (visible in Fig. 8.3b, such that each half can be slipped on and off a section of tube, thus, requiring no welding. Sufficient clamping force must be exerted by the bolted connection to ensure that O-ring seals between adjacent tube section or componens are fully compressed during tube operation. To achieve this, the flanges were dimensioned and toleranced such that there will always be a gap between the flange and adjacent component (see detail in Fig. 8.3a). This ensures that the clamping force provided by the bolts is fully transferred to the butt of the tube and not pressing the face of the flange into the adjacent component.

Concentricity must be maintained between all inline components of the shock tube to ensure the smoothness of the tube's bore. Any "steps" created by non-concentric components can significantly thicken the boundary layer or, in extreme cases, lead to the propagation of transverse waves within the tube. In order to maintain concentricity, the OD of each tube end is dimensioned to achieve a tight tolerance clearance fit into a matching socket machined into inline components (socket seen on test section in Fig. 8.4). In connections with no inline components (e.g., between the driver and driver extension), the function of the socket is replaced by an alignment ring with a similarly tight tolerance (see Fig. 8.3). The OD of each tube section was specified at a dimension and plus/minus tolerance of 5.5" $\frac{+0.000}{-0.002}$, and the sockets or alignment rings to an ID dimension of 5.503", $\frac{+0.002}{-0.000}$.

8.5 Test Section and Optical Access

The test section is located at the extreme end of the driven section of the shock tube, where optical and pressure measurements are typically acquired in shock-tube experiments. Hence, careful design of the test section helps to maximize a shock tube's utility by facilitating the application of a wide range of optical diagnostics, and improving the ergonomics of optical access.

A section view of the HPST's test section is shown in Fig. 8.4. Optical access consists of four primary lines-of-sight located ≈15 mm from the driven endwall and an additional line of sight located 295 mm upstream of the endwall. Three lines-of-sight are designed to accept standard circular, 25.4 mm diameter windows, with a maximum clear aperture of 20 mm. All windows are installed in plug-shaped window holders which can be removed and installed between experiments, allowing the user to quickly change window material or replace broken windows. This design is similar to that of many other shock tubes [129], [131], [133], [134]. One of the round window ports will be used to house a high-speed pressure transducer (Kistler 601B1, 0-1034 bar range) such that the pressure will be measured at the same axial location as the optical access. This will allow for the synchronization of optical diagnostics with the arrival of the incident or reflected shock wave. However, this precludes use of the opposite window port for line-of-sight measurements, and as such, some shock tubes designs have

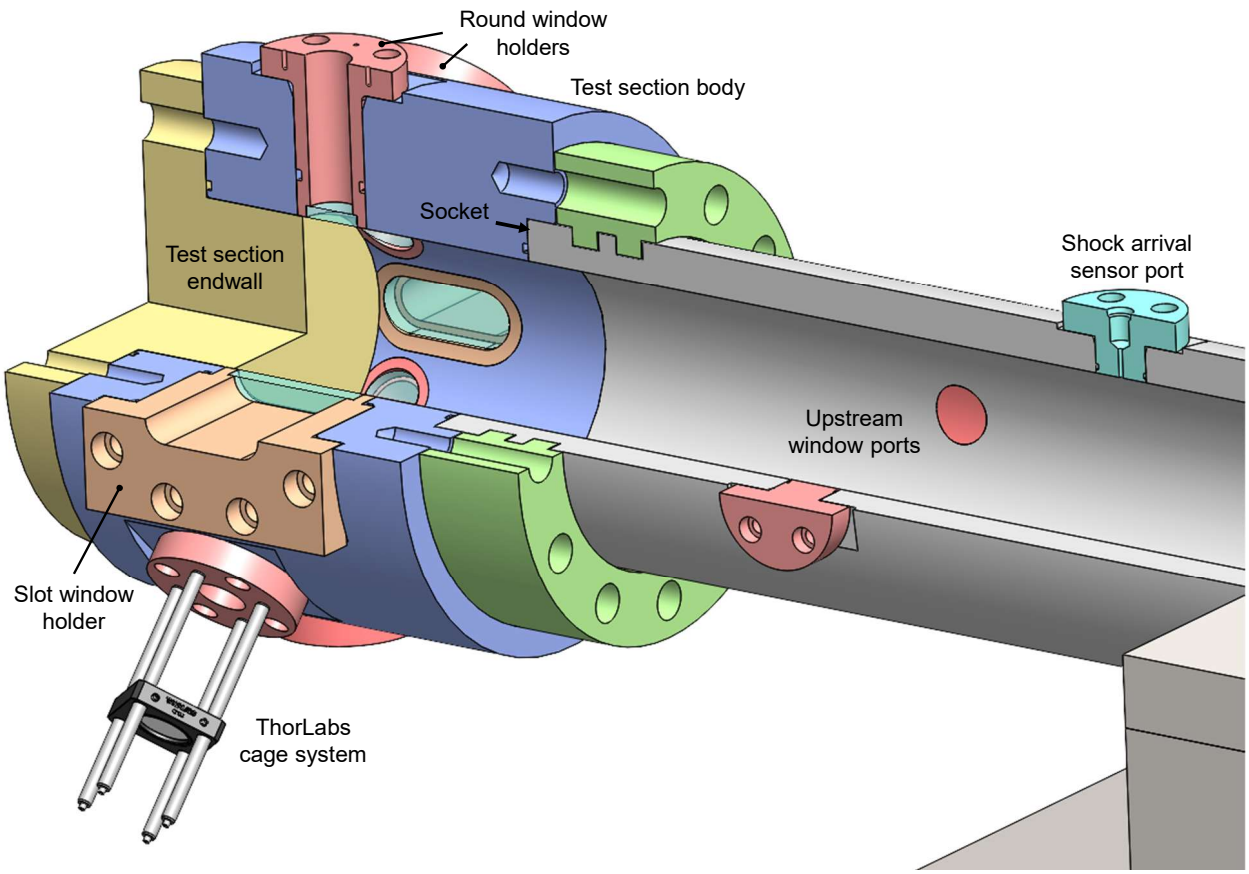

Figure 8.4. Half section of a CAD model of the HPST's test section. Of note is the designed compatibility of the round window ports with ThorLabs 30 mm cage system hardware. The upstream window ports are shown with blank access-port plugs installed.

removed the opposite port entirely [134]. However, it was decided to keep the opposite port to allow for flexibility in line-of-sight choice (window ports are interchangeable) or for use in imaging-based [135] or florescence-based [136] diagnostic techniques. For convenience, the round window holders were machined with threaded holes, to accept cage rods for ThorLabs' 30 mm optical cage system. The endwall of the test section can be swapped out with a modified version to change the effective location of the window ports with respect to the driven endwall.

The final primary line-of-sight is slot-shaped, to facilitate 1D studies of highly transient processes behind incident or reflected shock waves (e.g., fast chemical-kinetics, non-equilibrium relaxation) using laser-absorption measurements or imaging diagnostics. The

design of these window holders was based on the design of similar, but larger slot window holders by Tancin et al. [6]. The slot windows holders accept custom-made windows with a width of 25.4 mm and a distance between centers of 38.1 mm, yielding a maximum axial (relative to the tube bore) clear aperture of 57 mm. An upstream line-of-sight facilitates studies of high speed flows behind the incident shock wave. These window holders are modified access ports which are bored out to accept standard 12.7 mm diameter windows, yielding a maximum clear aperture of 10 mm.

The final noteworthy design aspect of the test section is an access-port on the underside of the tube, located 1 m upstream of the primary lines-of-sight. This port is designed to accommodate injection of powders or aerosols upstream of the measurement location, a widely used technique for studying combustion of powders, dusts or aerosols in a controlled environment [137], [138]. In an experiment studying powders, a piston-powered injector is typically used to inject the powder with a carrier gas into the shock tube ≈1-1.5 m upstream of the measurement location immediately prior to the bursting of the diaphragm. The high velocity gas behind the incident shock wave then carries the particles to the measurement location. The reflected shock wave stagnates the multi-phase flow, allowing for combustion studies in environments with known pressure, temperature and composition.

8.6 Diaphragm and Diaphragm Holder

The bursting of the diaphragm is responsible for creating the shock wave which generate precise gas conditions in the test section. A properly designed diaphragm holder maximizes the repeatability of experiments, and can mitigate effects which are detrimental to experiment quality [129], [139], [140]. A diaphragm holder which allows for rapid diaphragm changing expedites studies involving a wide range of test conditions or many repeated trials. Due to the importance and complexity of the diaphragm bursting there have been numerous studies devoted to characterizing their physics and optimizing their performance. For that reason, a literature review was conducted to identify the desirable performance characteristics for a diaphragm holder, and which design decisions can promote these qualities. Desirable

characteristics of diaphragm rupture are as follows: fast opening time, large opening area, symmetric opening and no fragmentation.

8.6.1 Shock Tube Diaphragm Design Considerations

While simplified analysis may assume instantaneous diaphragm opening and shock formation, opening times are finite and typically on the order of 100s of μs [139], [141]–[143]. As such, the opening time has a great deal on influence on shock formation and its spatiotemporal evolution as it propagates along the driven section [139], [141], [142], [144]–[146]. Importantly, reducing the diaphragm opening time reduces the shock formation distance (the distance between the diaphragm location and where the incident shock wave reaches its maximum value) and the slope of shock attenuation thereafter. Formation distance increases with shock strength (i.e., with pressure ratio across the diaphragm) [139], [143], [145], and is inversely related to sound speed of the driver gas. Reducing the formation distance in experiments involving strong shocks can be crucial. For example, White observed the shock wave still accelerating at the end of a 42 ft (12.8 m) long driver for experiments generating Mach 15 shock waves, meaning that a higher P_4 was needed to achieve the target conditions for state 5.

In addition to increased shock formation distances, slow opening times also yield higher peak mach numbers than that predicted by ideal shock tube theory [141], [145]. As the diaphragm opens, compression waves compress and adiabatically heat the driven gas. The compression waves coalesce, forming a weak shock wave which gradually strengthens (accelerates) as further compression waves catch up to the shock [139]. After the shock strength peaks, rarefaction waves catch up to the shock, decelerating it until the speed converges with that predicted by ideal theory [146]. This leads to a faster deceleration than that predicted by viscous and boundary layer effects alone [141], [146]. This can lead to a steeper or more complex shock attenuation profile at the test section, thus, complicating accurate extrapolation of shock speed at the driven endwall and introducing uncertainty into state 2 and state 5 gas conditions. Further, in cases with severe shock attenuation, higher diaphragm pressure ratios (P_4/P_1) may be needed to achieve target test conditions.

Similarly, the opening area (i.e., the area of a fully opened diaphragm) also effects the formation and propagation of the incident shock wave. Two area-related effects will be discussed here. The first is incomplete opening of the diaphragm, effectively creating an aperture-like constriction, and the second discusses the effects of shock tubes with different cross-sectional areas for the driver and driven sections. Incomplete opening of the diaphragm generates a weaker shock for a given P_4/P_1 [147], [148]. Shock tubes with square or rectangular diaphragm mounts typically have opening areas near 100%. This is due to the fact that as the diaphragm tears (typically in an X-shaped pattern [129], [149], [150]) the "hinges" of each diaphragm petal line up with the walls of the tube. For a circular cross section, opening area is expected to be similar to an inscribed square, yielding 64% open, though experimentally this has been observed to be as low as 50%. This results in reduced post-shock pressures of $\approx 5\%$ and $\approx 10\%$ respectively [151]. Though, some researchers have observed little affect in final shock strength stemming from diaphragm shape alone [148].

Shock tubes are sometimes built with unequal driver and driven cross sectional ratios. So called "converging shock tubes" are built with larger driver cross section areas than driven cross section areas (that is, $A_4 > A_1$) experience stronger shockwaves for the same P_4/P_1 [152], [153] and driver/driven gas compositions. Further, there is some evidence that it takes more time for the expansion wave to reach the driven end-wall, thus improving test times [152]. Diverging shock tubes typically see the opposite effects, though need less gas to pressurize the driver section to achieve a given P_4/P_1. Other types of shock tube diaphragm sections exist, such as those with a converging-diverging nozzle [152] at the diaphragm location or those with more than one diaphragm [154], though, they were not considered here.

Fragmentation of diaphragms when bursting is detrimental to the operation of shock tubes. Ideally, bursting diaphragms form petal-like flaps, which open to allow driver gas to rush through. Fragmentation occurs when pieces of the diaphragm are torn off completely, often resulting from an asymmetrical/ragged opening and is more common for brittle or thin diaphragms. Diaphragm fragments are sent down the driven end of the tube at high velocities, often marring the inner bore of the tube (contributes to enhanced boundary layer effects for future experiments), generating non-ideal flow effects, scratching or breaking windows and instrumentation or obscuring the line-of-sight of various diagnostics. Additionally,

fragments may not be able to be easily removed from the driven section without partially disassembling the tube.

Last, asymmetric opening is undesirable, due to its tendency to generate transverse waves, which leads to unsteady pressure traces at downstream locations, and uncertainty in post-shock temperatures [140].

8.6.2 Design of the Diaphragm Section

The diaphragm section of the HPST was designed to facilitate quick changing of diaphragms, minimize diaphragm opening time, have an opening area equal to the area of the driver and driven cross sections, and promote clean, symmetric bursting to generate a planar shock wave with no diaphragm fragments. A cross-section of the diaphragm section is shown in Fig. 8.5, and an image of the completed diaphragm holder is shown in Fig. 8.6. In order to facilitate fast changing of diaphragms between tests, the diaphragm section was designed in a canister-like configuration. The diaphragm is sandwiched between a pair of plates (driven-end diaphragm plate and driver-end diaphragm plate), which are then slid into the male diaphragm breech. Sealing is achieved with O-rings between each of the plates and diaphragm, and the stack of plates is then compressed as the female diaphragm breech is threaded onto the male diaphragm breech. This design, similar to that of the High-Enthalpy Shock Tube (HEST) at UCLA [134], allows for fast changing of the diaphragm in comparison to designs where bolt-circle type flanges are used, hence, requiring multiple bolts to be removed and re-installed between each test [131].

The diaphragm aperture (the area of unsupported diaphragm) was designed as a square. Square diaphragm apertures have faster opening times compared to round apertures for a given bursting area, because the diaphragm petals naturally tend to hinge along the edges of a square [142]. In contrast, for round diaphragms to open completely, there needs to be extra tearing near the base of the petals to allow the petal to hinge properly, likely increasing the opening time [151]. Further, tearing at the base of the petals increases the risk for diaphragm fragmentation. The driven diaphragm plate has a fillet machined onto it, to limit the bending radius of a diaphragm petal as the petals hinge open. The radius should be $\geq \frac{1}{2}t$ where t

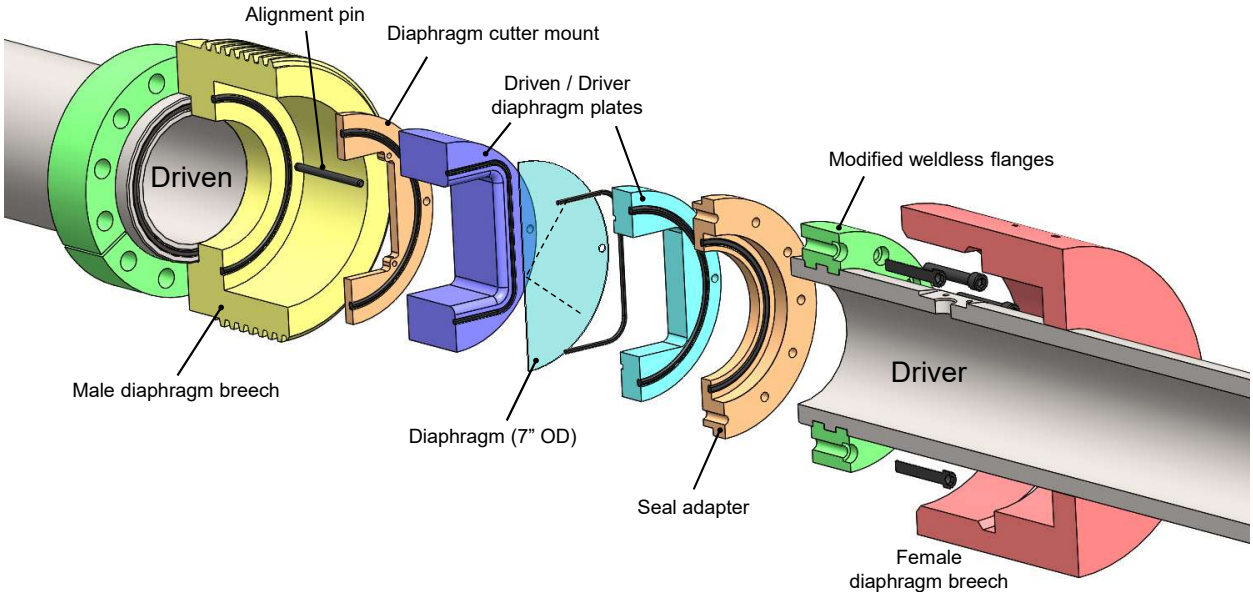

Figure 8.5. An exploded view of a CAD cross-section of the diaphragm section of the HPST. The clamping force to hold all of the components together and provide adequate force to seat the O-ring seals is provided by the large male and female diaphragm breech halves.

is the diaphragm thickness, in order to limit the stress at the hinge and prevent diaphragm petals from breaking [155]. A radius of 0.25 in (6.4 mm) was chosen, limiting the maximum diaphragm thickness to 0.125 in (3.2 mm). The thickness of the driven-end diaphragm plate was chosen to provide adequate clearance for the diaphragm petals to hinge open. Alignment pins which are threaded into the male diaphragm breech keep each component aligned as the diaphragm section is assembled prior to an experiment. The driven diaphragm plate is 1.25 times as thicker than 1/2 the dimension of the square, to provide unobstructed space for the diaphragm petals to fully hinge open.

The unsupported area of the diaphragm is slightly larger than the cross-sectional area of both the driver and driven section, to ensure that the diaphragm is not an impediment towards achieving maximum shock strength. The dimension of the square and that of the tube ID are nearly equal so that flow through the diaphragm section is relatively unimpeded. Optimally, a gradual transition between square and round sections would be used to minimize flow disturbances [156], though the area near the diaphragm is thought to be non-critical in terms of forming a boundary layer because the shock has not formed yet (e.g., diaphragm

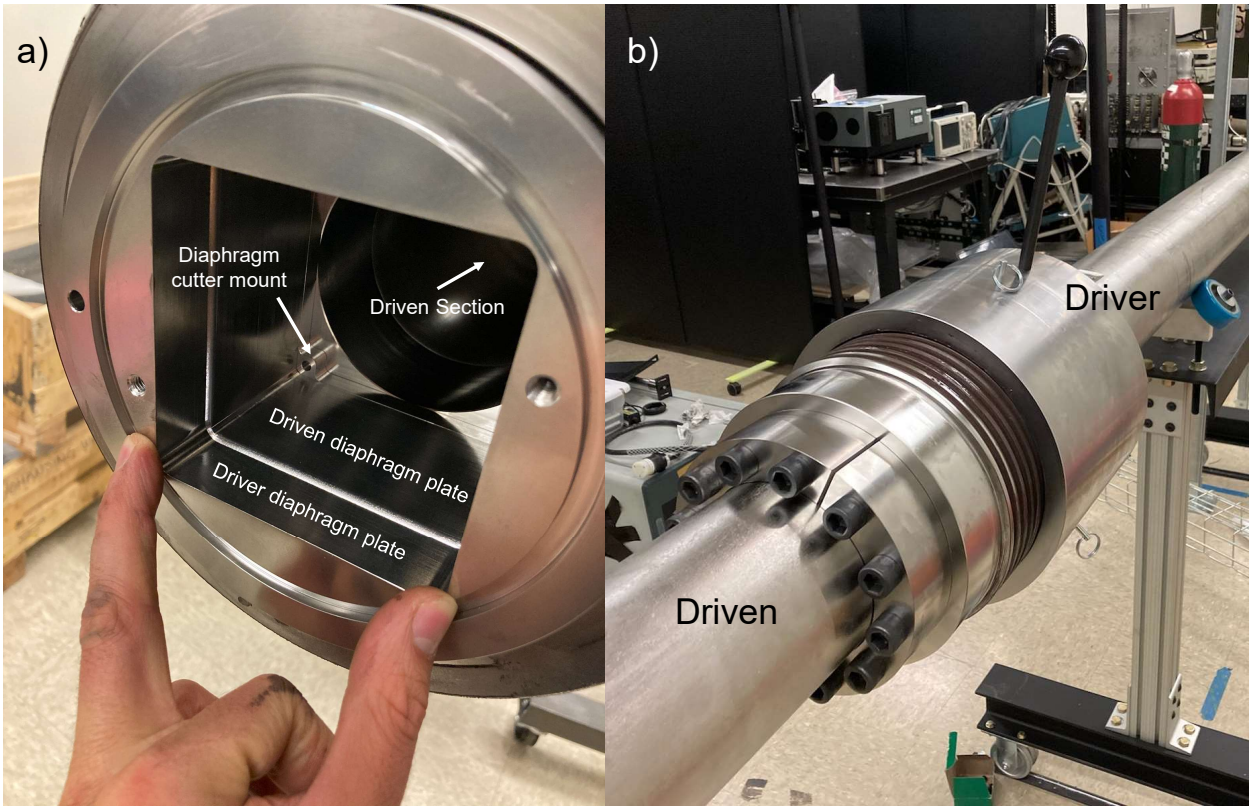

Figure 8.6. Photographs of the diaphragm section of the HPST. a) Inside of the male diaphragm breech showing the diaphragm plates and the diaphragm cutter holder. b) The assembled diaphragm section, looking towards the driver.

cutters places here interfere with the flow path, and do not have noticeable effects on test conditions). Hence, a step change is tolerated here in order to reduce machining costs.

In addition to the driven and driver diaphragm plates and the diaphragm itself, a diaphragm cutter mounting plate is also accommodated for in the design. This plate has 4 bolting locations where a variety of apparatus such as diaphragm cutter blades or other bursting initiators can be installed. Diaphragm cutters are widely used for initiating or guiding the bursting process [129], [149], [150], [157] and have been observed to reduce the opening time [149], prevent fragmentation [157], calibrate the burst pressure and prevent asymmetrical bursting [149]. They are particularly useful for very thin diaphragms ($t/D \leq 0.001$) where X-pattern scoring of the diaphragm is difficult or not possible, for improving the consistency of the burst pressure (P_4), and for reducing diaphragm fragmentation. For these reasons, accommodations for a future diaphragm cutter were made in the design.

8.7 Instrumentation and Tube Access

8.7.1 Poppet Valve

A dedicated valve for pulling vacuum on the driven section is necessary due to the low pressures needed for creating state 5 conditions with high temperature and low pressure or for tests requiring high levels of precision in gas composition. The requirement for low-pressure capability becomes apparent when analyzing conditions needed for a theoretical experiment. Consider an experiment with a test gas of argon, and target T_5 and P_5 of 3000 K and 0.5 bar respectively. In order to achieve these conditions, a P_1 of 5.1 Torr is needed. In order to control the composition of the gas to within 1%, the driven section must be pumped down to a pressure of 51 mTorr or lower. These vacuum requirements rapidly intensify when looking at higher temperatures and/or lower pressures (e.g., for studying gases or plasmas at conditions present during atmospheric entry) [158] or when the requirements for compositional purity are increased (e.g., for chemical kinetics experiments) [159]. Vacuum requirements for shock tubes often extend past 10^{-6} Torr.

Despite careful engineering and design, all vacuum vessels leak. The minimum pressure achievable will be determined by the leak rate of the vessel and the rate at which gas molecules can be removed by the vacuum pump, which has a pumping speed specified in units of L/s. In order to achieve adequately low pressures, gas molecules need to be able to flow towards the inlet of a vacuum pump with minimal impedance, thus, maximizing the pump throughput and minimizing pressure within the vessel. The impedance to flow, or lack thereof, between the vessel and pump inlet is customarily quantified by conductance (C), with units of L/s. Higher values are beneficial for achieving lower pressure. The shock tube will operate in both continuum and free molecular flow regimes, and the poppet valve will be analyzed as such. Summing the conductivities for continuum and free molecular flows gives a crude approximation for the transition flow regime in which the tube will most often operate. In continuum flow, conductivity for a pipe is given as Eq. 8.1 [160].

$$C_{continuum} = \frac{\pi d^4}{256 \eta l}(P_{upstream} + P_{downstream}) \tag{8.1}$$

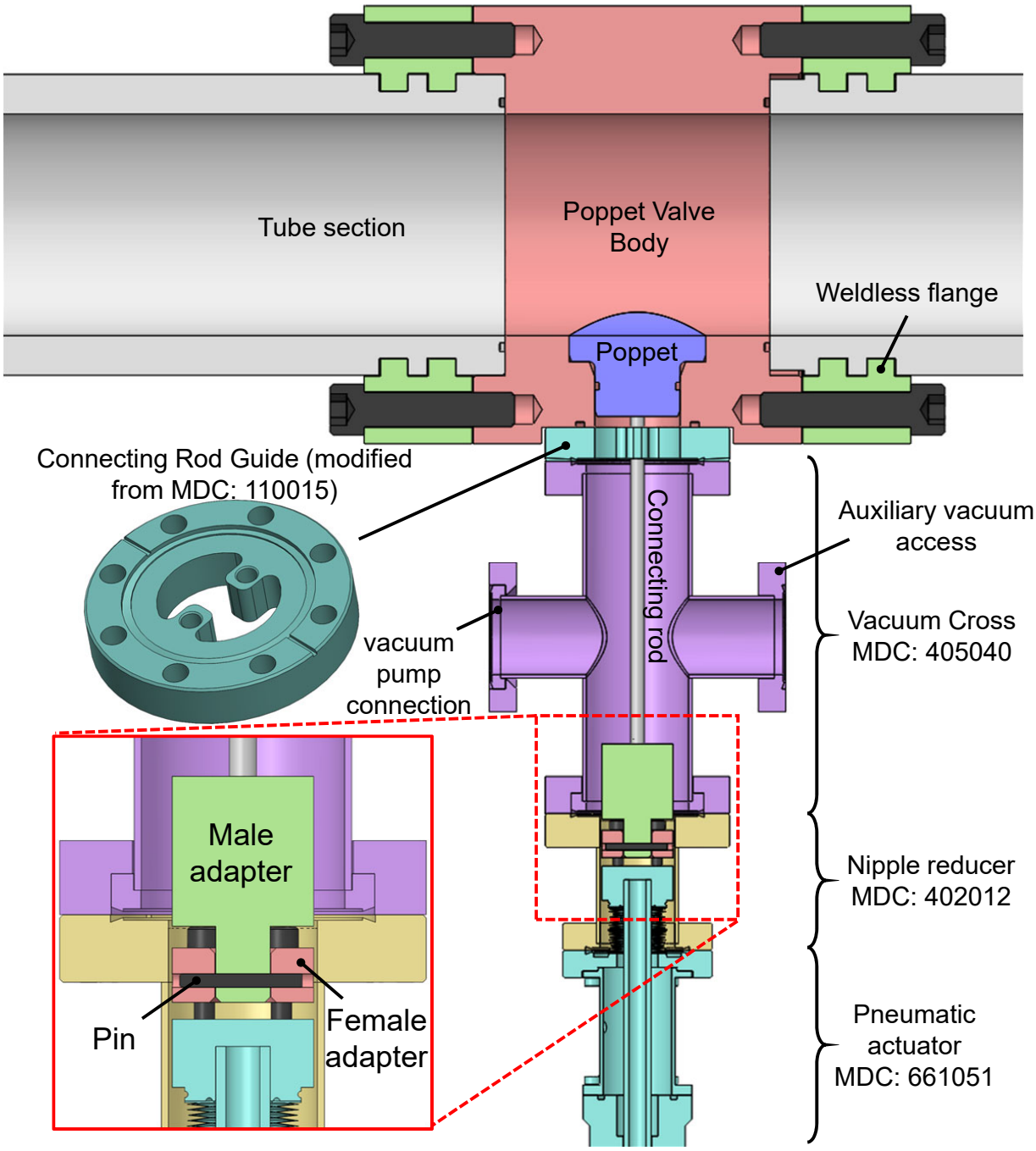

Figure 8.7. Cross-section of a CAD model illustrating the design and operation of a custom poppet valve for the HPST. Some valve components were commercially sourced or modified from commercially sourced components. These parts are labeled with their corresponding vendor and part numbers.

where d is the pipe internal diameter, η is the dynamic viscosity, l is the pipe length and $P_{upstream}$ and $P_{downstream}$ are the pressures on either end of the pipe. Further, it is known that continuum flow through an orifice is proportional to d^2. Thus, it is shown that maximizing the diameter of any pipes or orifices, and minimizing the distance between the pump and vessel has a large effect on the minimum pressure obtainable, as well as the time needed to pump down to this pressure (facilitating rapid repetition of experiments). Likewise, the free molecular flow regime ($<$ 1 mTorr) equations for pipes and orifices are given by Eq. 8.2 and Eq. 8.3, respectively [160].

$$C_{molecular} = \frac{\pi d^3}{12l}\sqrt{\frac{k_B T}{m_0}} \tag{8.2}$$

$$C_{molecular} = \frac{\pi d^2}{4}\sqrt{\frac{k_B T}{2\pi m_0}} \tag{8.3}$$

The same conclusions can be made from the free molecular flow equations regarding the design of the vacuum system. However, a large diameter port cannot simply be drilled into the wall of the tube, since this would cause intolerable disturbances to the incident shock wave. Hence, the valve has to be made integral with the driven section's inner bore in such a way that when the valve is closed, there are no obstructions or edges on the tube bore. One of the most common solutions for this is an integral poppet valve [156], [161], [162].

The custom poppet valve designed for the HPST is shown in Fig. 8.7. The valve consists of the poppet which is contoured to match the shock tube's bore, and the poppet valve body which seals against the poppet when the valve is closed. The valve seals using a piston seal O-ring located on the poppet. The O-ring seats against a small bore in the poppet valve body, which is contoured to minimize the force needed to seal the valve. The valve's moving parts and seals are lubricated with vacuum grease to further reduce friction. A piston seal O-ring design was used instead of a face seal design, because it can be ensured that the seal is completely seated as long as the valve is closed. A face seal design is only seated as long as continual force is applied by an actuator, allowing for potential damage to downstream equipment in the event the actuator fails. The valve is actuated by a double-acting pneumatic actuator from MDC Vacuum (part No. 661051) which was selected due to its high-vacuum

compatibility and adequate force for actuating the valve with a 1 atm pressure differential across it.

Other components of the valve are used for interfacing with the vacuum system. A guide (made from a modified blind flange from MDC vacuum) ensures that the poppet is held in the proper orientation relative to the shock tube bore. In order to attach the poppet's connecting rods to the actuator, a pair of adaptors needed to be made. These allow for bolted connections between the poppet and connecting rods to be made while the valve is dissembled. During final assembly of the valve, a pin is inserted into the two adaptors, locking the actuator to the poppet.

8.7.2 Access ports

Access for gas (fill, venting, and vacuum) and instrumentation (pressure transducers, shock sensors, and thermocouples) is achieved through 9 flanged access ports. The geometry of the access ports is displayed by a cross-section in Fig. 8.8. The ports consist of a plug-like design, with a top flange for bolting to the outer diameter of the shock tube. A 25 mm diameter hole is bored in the wall of the shock tube, and the access port fits into it, sealing with a piston-seal O-ring. A $\approx$ 2.5 mm deep flat, is milled onto the surface of the tube to provide a flat surface for a pattern of threaded bolt holes, which mirror the bolt pattern on the access port flange. The access ports can then be drilled or bored as needed to interface with any instrumentation or gas delivery system.

A flanged port design, as opposed to a threaded design (e.g., NPT or O-ring boss port) is desirable because it allows for repeatable and accurate positioning of the fitting. Therefore, the access port can be honed while installed in the tube wall (eliminating mismatch between port and tube bore) and later reassembled in the exact same position. The upstream window ports, and particle injection port described in section 8.5 utilize the same port design, but are bored to accept windows or a particle seeding system respectively.

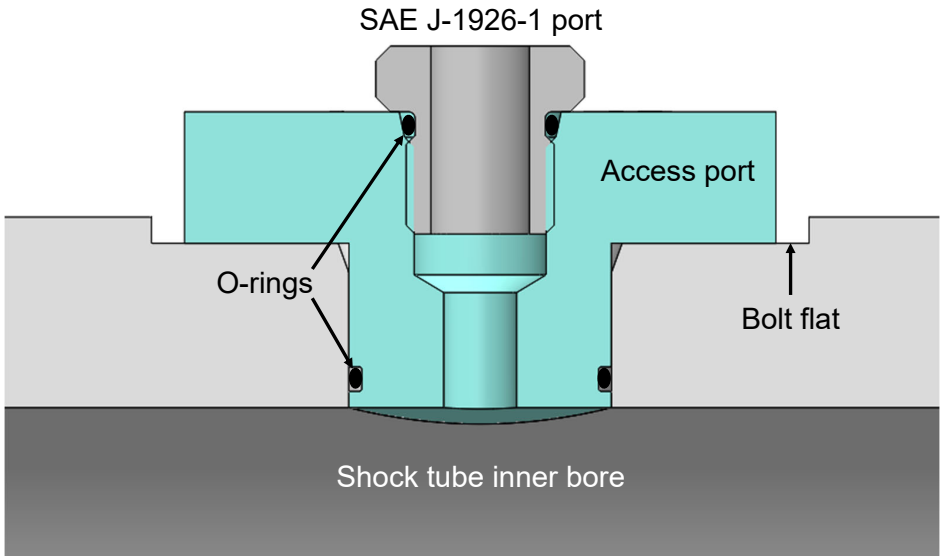

Figure 8.8. CAD cross-section of an access port, with an example of an SAE J-1926-1 strait threaded port installed.

8.7.3 Pressure and Shock Arrival Sensors

Gas conditions in the test section are determined from the normal shock-jump equation. Requisite inputs for determining post-shock conditions in state 2 and state 5 are the driven gas properties (e.g., specific heat ratio), the initial gas conditions, T_1 and P_1, (known from a lab thermometer and pressure transducer respectively), and the velocity of the incident shockwave. The incident shock velocity is determined through four shock arrival sensors and the high-speed Kistler pressure transducer. Shock velocity is determined by dividing the known distance between each shock sensor/pressure transducer by the difference in time of the shock's arrival. The velocity as a function of location along the driven section is then plotted, and a curve is fit to the data, allowing for extrapolation to estimate the shock velocity at the measurement location. Dynasen CA-1135 TOADs (Time Of Arrival Detectors) piezoelectric pins, were used as shock arrival sensors due to their substantially decreased cost ($\approx$ 30x cheaper) and complexity (no supporting electronics needed) compared to high-speed pressure transducers. These pins have been proven through testing to be accurate and repeatable with a standard deviation of $>$ 200 ps and pin-to-pin variation of $>$ 1 ns [163]. More recently these pins were also successfully used for accurate determination of

shock wave speed in the HEST at UCLA [134]. The four shock arrival sensors are installed into access ports spaced at 0.5 m intervals, beginning 0.5 m upstream from the measurement location.

Pressure at the measurement location is measured by a high-speed Kistler 601B1, 0-1034 bar range piezoelectric pressure transducer. The transducer is mounted in one of the round window ports, described in section 8.5, and is shown in Fig. 8.4. This was done to ensure that the pressure measurement is acquired at the exact same location as any optical diagnostics, and due to the fact that there was no additional room in the test section for a dedicated port.

The pressure in the driver section is monitored by a Setra Model 206 high-pressure transducer with a full scale, absolute-pressure range of 0-250 bar and an accuracy of 0.13% full scale.

REFERENCES

[1] C. S. Goldenstein, R. M. Spearrin, J. B. Jeffries, and R. K. Hanson, "Infrared laser-absorption sensing for combustion gases," *Progress in Energy and Combustion Science*, vol. 60, pp. 132–176, 2017, ISSN: 03601285. DOI: 10.1016/j.pecs.2016.12.002. [Online]. Available: http://dx.doi.org/10.1016/j.pecs.2016.12.002.

[2] "Measurements of multiple gas parameters in a pulsed-detonation combustor using time-division-multiplexed Fourier-domain mode-locked lasers," *Applied Optics*, vol. 52, no. 12, pp. 2893–2904, 2013, ISSN: 15394522. DOI: 10.1364/AO.52.002893.

[3] K. Kohse-Höinghaus, R. S. Barlow, M. Aldén, and J. Wolfrum, "Combustion at the focus: Laser diagnostics and control," *Proceedings of the Combustion Institute*, vol. 30, no. 1, pp. 89–123, 2005.

[4] R. Hanson and D. Davidson, "Recent advances in laser absorption and shock tube methods for studies of combustion chemistry," *Progress in Energy and Combustion Science*, vol. 44, pp. 103–114, 2014.

[5] T. Dreier, R. Chrystie, T. Endres, and C. Schulz, "Laser-based combustion diagnostics," *Encyclopedia of Analytical Chemistry*, pp. 1–44, 2016, ISSN: 10476938. DOI: 10.1002/9780470027318.a0715.pub3. [Online]. Available: http://doi.wiley.com/10.1002/9780470027318.a0715.pub3.

[6] R. J. Tancin, G. C. Mathews, and C. S. Goldenstein, "Design and application of a high-pressure combustion chamber for studying propellant flames with laser diagnostics," *Review of Scientific Instruments*, vol. 90, no. 4, p. 045 111, 2019. DOI: https://doi.org/10.1063/1.5081671.

[7] R. J. Tancin, R. M. Spearrin, and C. S. Goldenstein, "2D mid-infrared laser-absorption imaging for tomographic reconstruction of temperature and carbon monoxide in laminar flames," *Optics Express*, vol. 27, no. 10, p. 14 184, 2019. DOI: https://doi.org/10.1364/OE.27.014184.

[8] C. S. Goldenstein, R. M. Spearrin, J. B. Jeffries, and R. K. Hanson, "Infrared laser absorption sensors for multiple performance parameters in a detonation combustor," *Proceedings of the Combustion Institute*, vol. 35, no. 3, pp. 3739–3747, 2015.

[9] C. Wei, D. I. Pineda, L. Paxton, F. N. Egolfopoulos, and R. M. Spearrin, "Mid-infrared laser absorption tomography for quantitative 2D thermochemistry measurements in premixed jet flames," *Applied Physics B: Lasers and Optics*, vol. 124, no. 6, p. 123, 2018.

[10] R. Carro, M. Stephens, J. Arvanetes, A. Powell, E. Petersen, and C. Smith, "High-pressure testing of composite solid propellant mixtures: Burner facility characterization," in *41st AIAA/ASME/SAE/ASEE Joint Propulsion Conference and Exhibit*, 2005, ISBN: 978-1-62410-063-5. DOI: 10.2514/6.2005-3617. [Online]. Available: http://arc.aiaa.org/doi/abs/10.2514/6.2005-3617.

[11] F. A. Bendana, D. D. Lee, R. M. Spearrin, S. A. Schumaker, and S. A. Danczyk, "Infrared laser absorption thermometry and CO sensing in high-pressure rocket combustion flows from 25 to 105 bar," *AIAA Scitech 2019 Forum*, no. January, pp. 1–8, 2019. DOI: 10.2514/6.2019-1610.

[12] "High-pressure and high-temperature gas cell for absorption spectroscopy studies at wavelengths up to 8 μm," *Journal of Quantitative Spectroscopy and Radiative Transfer*, vol. 227, pp. 145–151, 2019, ISSN: 00224073. DOI: 10.1016/j.jqsrt.2019.01.029. [Online]. Available: https://doi.org/10.1016/j.jqsrt.2019.01.029.

[13] R. K. Hanson, R. M. Spearrin, and C. S. Goldenstein, *Spectroscopy and Optical Diagnostics for Gases*. Springer International Publishing Switzerland, 2016, ISBN: 9783319232515.

[14] C. S. Goldenstein and R. K. Hanson, "Diode-laser measurements of linestrength and temperature-dependent lineshape parameters for H_2O transitions near 1.4 μm using Voigt, Rautian, Galatry, and speed-dependent Voigt profiles," *Journal of Quantitative Spectroscopy and Radiative Transfer*, vol. 152, pp. 127–139, 2015.

[15] C. S. Goldenstein, J. B. Jeffries, and R. K. Hanson, "Diode laser measurements of linestrength and temperature-dependent lineshape parameters of H_2O-, CO_2-, and N_2-perturbed H_2O transitions near 2474 and 2482 nm," *Journal of Quantitative Spectroscopy and Radiative Transfer*, vol. 130, pp. 100–111, 2013.

[16] C. S. Goldenstein, V. A. Miller, R. M. Spearrin, and C. L. Strand, "Spectraplot.com: Integrated spectroscopic modeling of atomic and molecular gases," *Journal of Quantitative Spectroscopy and Radiative Transfer*, vol. 200, pp. 249–257, 2017.

[17] M. Donovan, X. He, B. Zigler, T. Palmer, M. Wooldridge, and A. Atreya, "Demonstration of a free-piston rapid compression facility for the study of high temperature combustion phenomena," *Combustion and Flame*, vol. 137, no. 3, pp. 351–365, 2004. DOI: 10.1016/j.combustflame.2004.02.006.

[18] E. F. Nasir and A. Farooq, "Time-resolved temperature measurements in a rapid compression machine using quantum cascade laser absorption in the intrapulse mode," *Proceedings of the Combustion Institute*, vol. 36, no. 3, pp. 4453–4460, 2017, ISSN: 15407489. DOI: 10.1016/j.proci.2016.07.010. [Online]. Available: http://dx.doi.org/10.1016/j.proci.2016.07.010.

[19] S. Burke and T. Schumann, "Diffusion flames," *Industrial and Engineering Chemistry*, vol. 20, no. 10, pp. 998–1004, 1928, ISSN: 00197866. DOI: 10.1021/ie50226a005.

[20] C. D. Carter, G. B. King, and N. M. Laurendeau, "A combustion facility for high-pressure flame studies by spectroscopic methods," *Review of Scientific Instruments*, vol. 60, no. 8, pp. 2606–2609, 1989, ISSN: 00346748. DOI: 10.1063/1.1140679.

[21] K. Thomson, O. Gulder, E. Weckman, R. Fraser, and D. Snelling, "A new diffusion flame burner and pressure vessel for high pressure soot formation study," in *Canadian Section, Spring Technical Meetings*, Windsor, ON: Combustion Institute, 2002.

[22] H. I. Joo and Ö. L. Gülder, "Soot formation and temperature structure in small methane-oxygen diffusion flames at subcritical and supercritical pressures," *Combustion and Flame*, vol. 157, no. 6, pp. 1194–1201, 2010, ISSN: 00102180. DOI: 10.1016/j.combustflame.2009.11.003. [Online]. Available: http://dx.doi.org/10.1016/j.combustflame.2009.11.003.

[23] A. M. Vargas and Ö. L. Gülder, "A multi-probe thermophoretic soot sampling system for high-pressure diffusion flames," *Review of Scientific Instruments*, vol. 87, no. 5, p. 055 101, 2016, ISSN: 10897623. DOI: 10.1063/1.4947509.

[24] L. L. McCrain and W. L. Roberts, "Measurements of the soot volume field in laminar diffusion flames at elevated pressures," *Combustion and Flame*, vol. 140, no. 1-2, pp. 60–69, 2005, ISSN: 00102180. DOI: 10.1016/j.combustflame.2004.10.005.

[25] Y. Li, "Applications of transient grating spectroscopy to temperature and transport properties measurements in high-pressure environments," PhD thesis, North Carolina State University, 2001.

[26] P. H. Joo, J. Gao, Z. Li, and M. Aldén, "Experimental apparatus with full optical access for combustion experiments with laminar flames from a single circular nozzle at elevated pressures," *Review of Scientific Instruments*, vol. 86, no. 3, pp. 1–8, 2015, ISSN: 10897623. DOI: 10.1063/1.4915624.

[27] J. W. Taylor, "A melting stage in the burning of solid secondary explosives," *Combustion and Flame*, vol. 6, pp. 103–107, 1962, ISSN: 00102180.

[28] B. L. Crawford, C. Huggett, F. Daniels, and R. E. Wilfong, "Direct determination of burning rates of propellant powders," *Analytical Chemistry*, vol. 19, no. 9, pp. 630–633, 1947, ISSN: 15206882. DOI: 10.1021/ac60009a004.

[29] W. McBratney and J. Vanderhoff, "High pressure windowed chamber burn rate determination of liquid propellant XM46," Army Research Laboratory, Tech. Rep., 1994, ARL–TR–442.

[30] E. Boyer and K. Kuo, "High-pressure combustion behavior of nitromethane," in *35th AIAA/ASME/SAE/ASEE Joint Propulsion Conference and Exhibit*, 1999, p. 2358. DOI: 10.2514/6.1999-2358. [Online]. Available: http://arc.aiaa.org/doi/10.2514/6.1999-2358.

[31] C. Schulz and V. Sick, "Tracer-LIF diagnostics: Quantitative measurement of fuel concentration, temperature and fuel/air ratio in practical combustion systems," *Progress in Energy and Combustion Science*, vol. 31, pp. 75–121, 2005, ISSN: 03601285. DOI: 10.1016/j.pecs.2004.08.002.

[32] C. H. Smith, C. S. Goldenstein, and R. K. Hanson, "A scanned-wavelength-modulation absorption-spectroscopy sensor for temperature and H_2O in low-pressure flames," *Measurement Science and Technology*, vol. 25, p. 115 501, 2014. DOI: 10.1088/0957-0233/25/11/115501.

[33] J. Girard, R. Spearrin, C. Goldenstein, and R. Hanson, "Compact optical probe for flame temperature and carbon dioxide using interband cascade laser absorption near 4.2 μm," *Combustion and Flame*, vol. 178, pp. 158–167, 2017, ISSN: 00102180. DOI: 10.1016/j.combustflame.2017.01.007. [Online]. Available: http://dx.doi.org/10.1016/j.combustflame.2017.01.007.

[34] R. M. Spearrin, C. S. Goldenstein, I. A. Schultz, J. B. Jeffries, and R. K. Hanson, "Simultaneous sensing of temperature, CO, and CO_2 in a scramjet combustor using quantum cascade laser absorption spectroscopy," *Applied Physics B: Lasers and Optics*, vol. 117, pp. 689–698, 2014. DOI: 10.1007/s00340-014-5884-0.

[35] L. Rothman, I. Gordon, R. Barber, H. Dothe, R. Gamache, A. Goldman, V. Perevalov, S. Tashkun, and J. Tennyson, "HITEMP, the high-temperature molecular spectroscopic database," *Journal of Quantitative Spectroscopy and Radiative Transfer*, vol. 111, no. 15, pp. 2139–2150, 2010.

[36] C. J. Tang, Y. J. Lee, G. Kudva, and T. A. Litzinger, "A study of the gas-phase chemical structure during CO_2 laser assisted combustion of HMX," *Combustion and Flame*, vol. 117, no. 1-2, pp. 170–188, 1999, ISSN: 00102180. DOI: 10.1016/S0010-2180(98)00094-7.

[37] J. C. Finlinson, T. Parr, and D. Hanson-Parr, "Laser recoil, plume emission, and flame height combustion response of HMX and RDX at atmospheric pressure," *Symposium (International) on Combustion*, vol. 25, no. 1, pp. 1645–1650, 1994.

[38] I. A. Schultz, C. S. Goldenstein, C. L. Strand, J. B. Jeffries, R. K. Hanson, and C. P. Goyne, "Hypersonic scramjet testing via diode laser absorption in a reflected shock tunnel," *Propulsion and Power*, vol. 30, no. 6, pp. 1586–1594, 2014. DOI: 10.2514/1.B35220.

[39] C. S. Goldenstein, R. M. Spearrin, J. B. Jeffries, and R. K. Hanson, "Infrared laser absorption sensors for multiple performance parameters in a detonation combustor," *Proceedings of the Combustion Institute*, vol. 35, no. 3, pp. 3739–3747, 2015, ISSN: 1540-7489. DOI: 10.1016/j.proci.2014.05.027. [Online]. Available: http://dx.doi.org/10.1016/j.proci.2014.05.027.

[40] C. L. Strand and R. K. Hanson, "Quantification of supersonic impulse flow conditions via high-bandwidth wavelength modulation absorption spectroscopy," *AIAA Journal*, vol. 53, no. 10, pp. 2978–2987, 2015, ISSN: 0001-1452. DOI: 10.2514/1.J053842. [Online]. Available: http://arc.aiaa.org/doi/10.2514/1.J053842.

[41] L. Ma, X. Li, S. T. Sanders, A. W. Caswell, S. Roy, D. H. Plemmons, and J. R. Gord, "50-kHz-rate 2D imaging of temperature and H_2O concentration at the exhaust plane of a J85 engine using hyperspectral tomography," *Optics express*, vol. 21, no. 1, pp. 1152–1162, 2013.

[42] F. Stritzke, O. Diemel, and S. Wagner, "TDLAS-based NH_3 mole fraction measurement for exhaust diagnostics during selective catalytic reduction using a fiber-coupled 2.2-μm DFB diode laser," *Applied Physics B: Lasers and Optics*, vol. 119, no. 1, pp. 143–152, 2015.

[43] N. Terzija, S. Karagiannopoulos, S. Begg, P. Wright, K. Ozanyan, and H. McCann, "Tomographic imaging of the liquid and vapour fuel distributions in a single-cylinder direct-injection gasoline engine," *International Journal of Engine Research*, vol. 16, no. 4, pp. 565–579, 2015, ISSN: 1468-0874. DOI: 10.1177/1468087414544178. [Online]. Available: http://jer.sagepub.com/lookup/doi/10.1177/1468087414544178.

[44] C. Liu, L. Xu, J. Chen, Z. Cao, and Y. Lin, "Development of a fan-beam TDLAS-based tomographic sensor for rapid imaging of temperature and gas concentration," *Optics Express*, vol. 23, no. 17, pp. 4827–4842, 2015. DOI: 10.1364/OE.23.022494.

[45] C. S. Goldenstein, I. A. Schultz, R. M. Spearrin, J. B. Jeffries, and R. K. Hanson, "Scanned-wavelength-modulation spectroscopy near 2.5 μm for H_2O and temperature in a hydrocarbon-fueled scramjet combustor," *Applied Physics B: Lasers and Optics*, vol. 116, pp. 717–727, 2014. DOI: 10.1007/s00340-013-5755-0.

[46] X. An, M. S. Brittelle, P. T. Lauzier, J. R. Gord, S. Roy, G.-H. Chen, and S. T. Sanders, "Demonstration of temperature imaging by H_2O absorption spectroscopy using compressed sensing tomography," *Applied Optics*, vol. 54, no. 31, p. 9190, 2015, ISSN: 0003-6935. DOI: 10.1364/AO.54.009190. [Online]. Available: https://www.osapublishing.org/abstract.cfm?URI=ao-54-31-9190.

[47] K. M. Busa, B. Rice, J. C. McDaniel, C. P. Goyne, R. D. Rockwell, J. A. Fulton, J. R. Edwards, and G. S. Diskin, "Direct measurement of combustion efficiency of a dual-mode scramjet via TDLAT and SPIV," in *53rd AIAA Aerospace Sciences Meeting*, 2015, AIAA 2015–0357, ISBN: 978-1-62410-343-8. DOI: 10.2514/6.2015-0357. [Online]. Available: http://arc.aiaa.org/doi/10.2514/6.2015-0357.

[48] C. S. Goldenstein, I. A. Schultz, J. B. Jeffries, and R. K. Hanson, "Two-color absorption spectroscopy strategy for measuring the column density and path average temperature of the absorbing species in nonuniform gases," *Applied Optics*, vol. 52, no. 33, pp. 7950–7962, 2013.

[49] W. Cai and C. F. Kaminski, "Tomographic absorption spectroscopy for the study of gas dynamics and reactive flows," *Progress in Energy and Combustion Science*, vol. 59, pp. 1–42, 2017, ISSN: 03601285. DOI: 10.1016/j.pecs.2016.11.002. [Online]. Available: http://dx.doi.org/10.1016/j.pecs.2016.11.002.

[50] H. McCann, P. Wright, and K. Daun, "Chemical species tomography," in *Industrial Tomography: Systems and Applications*, M. Wang, Ed., Elsevier, 2015, ch. 5.

[51] R. Villarreal and P. L. Varghese, "Frequency-resolved absorption tomography with tunable diode lasers.," *Applied Optics*, vol. 44, no. 31, pp. 6786–6795, 2005, ISSN: 0003-6935. DOI: 10.1364/AO.44.006786.

[52] P. Nau, J. Koppmann, A. Lackner, K. Kohse-Höinghaus, and A. Brockhinke, "Quantum cascade laser-based MIR spectrometer for the determination of CO and CO_2 concentrations and temperature in flames," *Applied Physics B: Lasers and Optics*, vol. 118, no. 3, pp. 361–368, 2015, ISSN: 09462171. DOI: 10.1007/s00340-014-5992-x.

[53] X. Liu, G. Zhang, Y. Huang, Y. Wang, and F. Qi, "Two-dimensional temperature and carbon dioxide concentration profiles in atmospheric laminar diffusion flames measured by mid-infrared direct absorption spectroscopy at 4.2 μm," *Applied Physics B: Lasers and Optics*, vol. 124, no. 61, pp. 1–10, 2018, ISSN: 09462171. DOI: 10.1007/s00340-018-6930-0. [Online]. Available: http://dx.doi.org/10.1007/s00340-018-6930-0.

[54] F. Wang, K. F. Cen, N. Li, J. B. Jeffries, Q. X. Huang, J. H. Yan, and Y. Chi, "Two-dimensional tomography for gas concentration and temperature distributions based on tunable diode laser absorption spectroscopy," *Measurement Science and Technology*, vol. 21, no. 4, 2010, ISSN: 13616501. DOI: 10.1088/0957-0233/21/4/045301.

[55] C. Wei, D. I. Pineda, C. S. Goldenstein, and R. M. Spearrin, "Tomographic laser absorption imaging of combustion species and temperature in the mid-wave infrared," *Optics express*, vol. 26, no. 16, pp. 20 944–20 951, 2018.

[56] P. S. Greenberg and J. C. Ku, "Soot volume fraction imaging," *Applied Optics*, vol. 36, no. 22, p. 5514, 1997, ISSN: 0003-6935. DOI: 10.1364/AO.36.005514. [Online]. Available: https://www.osapublishing.org/abstract.cfm?URI=ao-36-22-5514.

[57] C. Y. Chen, W. C. Su, C. H. Lin, M. D. Ke, Q. L. Deng, and K. Y. Chiu, "Reduction of speckles and distortion in projection system by using a rotating diffuser," *Optical Review*, vol. 19, no. 6, pp. 440–443, 2012, ISSN: 13406000. DOI: 10.1007/s10043-012-0075-x.

[58] T. Stangner, H. Zhang, T. Dahlberg, K. Wiklund, and M. Andersson, "A step-by-step guide to reduce spatial coherence of laser light using a rotating ground glass diffuser," *Applied Optics*, vol. 56, no. 19, pp. 5427–5435, May 2017, ISSN: 0938-1287. DOI: 10.1364/ao.56.005427. [Online]. Available: http://dx.doi.org/10.1364/ao.56.005427.

[59] L. S. Rothman, I. Gordon, Y. Babikov, A. Barbe, D. Chris Benner, P. Bernath, M. Birk, L. Bizzocchi, V. Boudon, L. Brown, A. Campargue, K. Chance, E. Cohen, L. Coudert, V. Devi, B. Drouin, A. Fayt, J.-M. Flaud, R. R. Gamache, J. Harrison, J.-M. Hartmann, C. Hill, J. Hodges, D. Jacquemart, A. Jolly, J. Lamouroux, R. Le Roy, G. Li, D. Long, O. Lyulin, C. Mackie, S. Massie, S. Mikhailenko, H. Müller, O. Naumenko, A. Nikitin, J. Orphal, V. Perevalov, A. Perrin, E. Polovtseva, C. Richard, M. Smith, E. Starikova, K. Sung, S. Tashkun, J. Tennyson, G. Toon, V. G. Tyuterev, and G. Wagner, "The HITRAN2012 molecular spectroscopic database," *Journal of Quantitative Spectroscopy and Radiative Transfer*, vol. 130, pp. 4–50, Nov. 2013, ISSN: 00224073. DOI: 10.1016/j.jqsrt.2013.07.002. [Online]. Available: http://linkinghub.elsevier.com/retrieve/pii/S0022407313002859.

[60] K. J. Daun, K. A. Thomson, F. Liu, and G. J. Smallwood, "Deconvolution of axisymmetric flame properties using Tikhonov regularization," *Applied Optics*, vol. 45, no. 19, pp. 4638–4646, Jul. 2006, ISSN: 0003-6935. DOI: 10.1364/AO.45.004638. [Online]. Available: https://www.osapublishing.org/abstract.cfm?URI=ao-45-19-4638.

[61] P. C. Hansen, *Rank-Deficient and Discrete Ill-Posed Problems: Numerical Aspects of Linear Inversion*. Philadelphia: SIAM, 1998. DOI: 10.1137/1.9780898719697.

[62] R. J. Tancin, Z. Chang, M. Gu, V. Radhakrishna, R. P. Lucht, and C. S. Goldenstein, "Ultrafast laser-absorption spectroscopy for single-shot, mid-infrared measurements of temperature, CO, and CH_4 in flames," *Optics Letters*, vol. 45, no. 2, pp. 583–586, 2020.

[63] D. I. Pineda, F. A. Bendana, K. K. Schwarm, and R. M. Spearrin, "Multi-isotopologue laser absorption spectroscopy of carbon monoxide for high-temperature chemical kinetic studies of fuel mixtures," *Combustion and Flame*, vol. 207, pp. 379–390, 2019, ISSN: 15562921. DOI: 10.1016/j.combustflame.2019.05.030. [Online]. Available: https://doi.org/10.1016/j.combustflame.2019.05.030.

[64] X. An, A. W. Caswell, and S. T. Sanders, "Quantifying the temperature sensitivity of practical spectra using a new spectroscopic quantity: Frequency-dependent lower-state energy," *Journal of Quantitative Spectroscopy and Radiative Transfer*, vol. 112, no. 5, pp. 779–785, 2011, ISSN: 00224073. DOI: 10.1016/j.jqsrt.2010.10.014. [Online]. Available: http://dx.doi.org/10.1016/j.jqsrt.2010.10.014.

[65] S. T. Sanders, J. Wang, J. B. Jeffries, and R. K. Hanson, "Diode-laser absorption sensor for line-of-sight gas temperature distributions," *Applied Optics*, vol. 40, no. 24, pp. 4404–4415, Aug. 2001. DOI: 10.1364/AO.40.004404. [Online]. Available: http://ao.osa.org/abstract.cfm?URI=ao-40-24-4404.

[66] K. D. Rein, S. Roy, S. T. Sanders, A. W. Caswell, F. R. Schauer, and J. R. Gord, "Measurements of gas temperatures at 100 kHz within the annulus of a rotating detonation engine," *Applied Physics B: Lasers and Optics*, vol. 123, no. 3, p. 88, 2017.

[67] C. L. Strand, Y. Ding, S. E. Johnson, and R. K. Hanson, "Measurement of the mid-infrared absorption spectra of ethylene (C_2H_4) and other molecules at high temperatures and pressures," *Journal of Quantitative Spectroscopy and Radiative Transfer*, vol. 222, pp. 122–129, 2019, ISSN: 00224073. DOI: 10.1016/j.jqsrt.2018.10.030. [Online]. Available: https://doi.org/10.1016/j.jqsrt.2018.10.030.

[68] S. T. Sanders, "Wavelength-agile fiber laser using group-velocity dispersion of pulsed super-continua and application to broadband absorption spectroscopy," *Applied Physics B: Lasers and Optics*, vol. 75, no. 6-7, pp. 799–802, 2002, ISSN: 09462171. DOI: 10.1007/s00340-002-1044-z.

[69] N. Göran Blume and S. Wagner, "Broadband supercontinuum laser absorption spectrometer for multiparameter gas phase combustion diagnostics," *Optics Letters*, vol. 40, no. 13, p. 3141, 2015, ISSN: 0146-9592. DOI: 10.1364/ol.40.003141.

[70] P. J. Schroeder, R. J. Wright, S. Coburn, B. Sodergren, K. C. Cossel, S. Droste, G. W. Truong, E. Baumann, F. R. Giorgetta, I. Coddington, N. R. Newbury, and G. B. Rieker, "Dual frequency comb laser absorption spectroscopy in a 16 MW gas turbine exhaust," *Proceedings of the Combustion Institute*, vol. 36, no. 3, pp. 4565–4573, 2017, ISSN: 15407489. DOI: 10.1016/j.proci.2016.06.032. [Online]. Available: http://dx.doi.org/10.1016/j.proci.2016.06.032.

[71] A. D. Draper, R. K. Cole, A. S. Makowiecki, A. Zdanawicz, J. Mohr, A. Marchese, N. Hoghoogi, and G. B. Rieker, "Progress toward dual frequency comb spectroscopy in a rapid compression machine," *Optics Express*, vol. 27, no. 8, pp. 10 814–10 825, 2019. DOI: 10.2514/6.2019-0026.

[72] H. U. Stauffer, P. S. Walsh, S. Roy, and J. R. Gord, "Time-resolved optically gated absorption (TOGA) spectroscopy: A background-free, single-shot broadband absorption method for combusting flows," *AIAA Scitech 2019 Forum*, no. January, p. 1607, 2019. DOI: 10.2514/6.2019-1607.

[73] T. Werblinski, P. Fendt, L. Zigan, and S. Will, "High-speed combustion diagnostics in a rapid compression machine by broadband supercontinuum absorption spectroscopy," *Applied Optics*, vol. 56, no. 15, pp. 4443–4453, 2017.

[74] N. Cezard, A. Dobroc, G. Canat, M. Duhant, W. Renard, C. Alhenc-Gelas, S. Lefebvre, and J. Fade, "Supercontinuum laser absorption spectroscopy in the mid-infrared range for identification and concentration estimation of a multi-component atmospheric gas mixture," in *Lidar Technologies, Techniques, and Measurements for Atmospheric Remote Sensing VII*, International Society for Optics and Photonics, vol. 8182, 2011, p. 81820V.

[75] R. M. Spearrin, C. S. Goldenstein, I. A. Schultz, J. B. Jeffries, and R. K. Hanson, "Simultaneous sensing of temperature, CO, and CO_2 in a scramjet combustor using quantum cascade laser absorption spectroscopy," *Applied Physics B: Lasers and Optics*, vol. 117, no. 2, pp. 689–698, 2014, ISSN: 09462171. DOI: 10.1007/s00340-014-5884-0.

[76] D. D. Lee, F. A. Bendana, S. A. Schumaker, and R. M. Spearrin, "Wavelength modulation spectroscopy near 5 μm for carbon monoxide sensing in a high-pressure kerosene-fueled liquid rocket combustor," *Applied Physics B: Lasers and Optics*, vol. 124, no. 5, p. 77, 2018.

[77] R. Hargreaves, I. Gordon, R. Kochanov, and L. Rothman, "HITEMP: extensive molecular line lists for high-temperature exoplanet atmospheres," *EPSC*, vol. 2019, EPSC–DPS2019, 2019.

[78] R. J. Hargreaves, I. E. Gordon, M. Rey, A. V. Nikitin, V. G. Tyuterev, R. V. Kochanov, and L. S. Rothman, "An accurate, extensive, and practical line list of methane for the HITEMP database," *The Astrophysical Journal Supplement Series*, vol. 247, no. 2, p. 55, 2020.

[79] R. J. Tancin, Z. Chang, V. Radhakrishna, M. Gu, R. P. Lucht, and C. S. Goldenstein, "Ultrafast laser absorption spectroscopy in the mid-infrared for measuring temperature and species in combustion gases," in *AIAA Scitech 2020 Forum*, 2020, p. 0517.

[80] J. Girard and R. Hanson, "Minimally intrusive optical probe for in situ shock tube measurements of temperature and species via tunable IR laser absorption," *Applied Physics B: Lasers and Optics*, vol. 123, no. 11, pp. 1–11, 2017.

[81] D. D. Lee, F. A. Bendana, A. P. Nair, R. M. Spearrin, S. A. Danczyk, and W. A. Hargus, "Laser absorption of carbon dioxide at the vibrational bandhead near 4.2 μm in high-pressure rocket combustion environments," in *AIAA Scitech 2020 Forum*, 2020, pp. 298–305.

[82] D. W. Hahn and N. Omenetto, "Laser-induced breakdown spectroscopy (libs), part i: Review of basic diagnostics and plasma–particle interactions: Still-challenging issues within the analytical plasma community," *Applied Spectroscopy*, vol. 64, no. 12, 335A–366A, 2010.

[83] S. N. Park, J. W. Hahn, and C. Rhee, "Effect of the slit function of the detection system and a fast-fitting algorithm on accuracy of CARS temperature," *Applied Spectroscopy*, vol. 48, no. 6, pp. 737–741, 1994.

[84] R. J. Tancin, M. Ruesch, S. F. Son, R. P. Lucht, and C. S. Goldenstein, "Ultrafast-laser-absorption-spectroscopy measurements of gas temperature in multi-phase, high-pressure combustion gases," in *AIAA Scitech 2021 Forum*, 2021, p. 0719. DOI: https://doi.org/10.2514/6.2021-0719.

[85] R. P. Lucht, V. Velur-Natarajan, C. D. Carter, K. D. Grinstead Jr, J. R. Gord, P. M. Danehy, G. Fiechtner, and R. L. Farrow, "Dual-pump coherent anti-stokes raman scattering temperature and CO concentration measurements," *AIAA Journal*, vol. 41, no. 4, pp. 679–686, 2003.

[86] R. D. Hancock, F. R. Schauer, R. P. Lucht, and R. L. Farrow, "Dual-pump coherent anti-stokes raman scattering measurements of nitrogen and oxygen in a laminar jet diffusion flame," *Applied Optics*, vol. 36, no. 15, pp. 3217–3226, 1997.

[87] L. De Galan and J. Winefordner, "Slit function effects in atomic spectroscopy," *Spectrochimica Acta Part B: Atomic Spectroscopy*, vol. 23, no. 4, pp. 277–289, 1968.

[88] U. Heitmann, M. Schütz, H. Becker-Roß, and S. Florek, "Measurements on the zeeman-splitting of analytical lines by means of a continuum source graphite furnace atomic absorption spectrometer with a linear charge coupled device array," *Spectrochimica Acta Part B: Atomic Spectroscopy*, vol. 51, no. 9-10, pp. 1095–1105, 1996.

[89] K. K. Schwarm, H. Q. Dinh, C. S. Goldenstein, D. I. Pineda, and R. M. Spearrin, "High-pressure and high-temperature gas cell for absorption spectroscopy studies at wavelengths up to 8 μm," *Journal of Quantitative Spectroscopy and Radiative Transfer*, vol. 227, pp. 145–151, 2019.

[90] J.-M. Hartmann, L. Rosenmann, M.-Y. Perrin, and J. Taine, "Accurate calculated tabulations of CO line broadening by H_2O, N_2, O_2, and CO_2 in the 200-3000 K temperature range," *Applied Optics*, vol. 27, no. 15, pp. 3063–3065, 1988.

[91] A. P. Nair, D. D. Lee, D. I. Pineda, J. Kriesel, W. A. Hargus, J. W. Bennewitz, S. A. Danczyk, and R. M. Spearrin, "MHz laser absorption spectroscopy via diplexed RF modulation for pressure, temperature, and species in rotating detonation rocket flows," *Applied Physics B: Lasers and Optics*, vol. 126, no. 8, pp. 126–138, 2020.

[92] D. R. Richardson, S. P. Kearney, and D. R. Guildenbecher, "Post-detonation fireball thermometry via femtosecond-picosecond coherent anti-stokes raman scattering (CARS)," *Proceedings of the Combustion Institute*, 2020.

[93] R. K. Cole, A. S. Makowiecki, N. Hoghooghi, and G. B. Rieker, "Baseline-free quantitative absorption spectroscopy based on cepstral analysis," *Optics Express*, vol. 27, no. 26, pp. 37 920–37 939, 2019.

[94] C. S. Goldenstein, G. C. Mathews, R. K. Cole, A. S. Makowiecki, and G. B. Rieker, "Cepstral analysis for baseline-insensitive absorption spectroscopy using light sources with pronounced intensity variations," *Applied Optics*, vol. 59, no. 26, pp. 7865–7875, 2020.

[95] F. A. Bendana, D. D. Lee, S. A. Schumaker, S. A. Danczyk, and R. M. Spearrin, "Cross-band infrared laser absorption of carbon monoxide for thermometry and species sensing in high-pressure rocket flows," *Applied Physics B: Lasers and Optics*, vol. 125, no. 11, p. 204, 2019.

[96] C. S. Goldenstein, C. A. Almodóvar, J. B. Jeffries, R. K. Hanson, and C. M. Brophy, "High-bandwidth scanned-wavelength-modulation spectroscopy sensors for temperature and H_2O in a rotating detonation engine," *Measurement Science and Technology*, vol. 25, no. 10, p. 105 104, 2014.

[97] A. W. Caswell, S. Roy, X. An, S. T. Sanders, F. R. Schauer, and J. R. Gord, "Measurements of multiple gas parameters in a pulsed-detonation combustor using time-division-multiplexed fourier-domain mode-locked lasers," *Applied Optics*, vol. 52, no. 12, pp. 2893–2904, 2013.

[98] E. Schlosser, T. Fernholz, H. Teichert, and V. Ebert, "In situ detection of potassium atoms in high-temperature coal-combustion systems using near-infrared-diode lasers," *Spectrochimica Acta Part A: Molecular and Biomolecular Spectroscopy*, vol. 58, no. 11, pp. 2347–2359, 2002.

[99] A. D. Draper, R. K. Cole, A. S. Makowiecki, J. Mohr, A. Zdanowicz, A. Marchese, N. Hoghooghi, and G. B. Rieker, "Broadband dual-frequency comb spectroscopy in a rapid compression machine," *Optics Express*, vol. 27, no. 8, pp. 10 814–10 825, 2019.

[100] K. D. Rein, S. Roy, S. T. Sanders, A. W. Caswell, F. R. Schauer, and J. R. Gord, "Measurements of gas temperatures at 100 kHz within the annulus of a rotating detonation engine," *Applied Physics B: Lasers and Optics*, vol. 123, no. 3, p. 88, 2017.

[101] S. T. Sanders, D. W. Mattison, L. Ma, J. B. Jeffries, and R. K. Hanson, "Wavelength-agile diode-laser sensing strategies for monitoring gas properties in optically harsh flows: Application in cesium-seeded pulse detonation engine," *Optics Express*, vol. 10, no. 12, pp. 505–514, 2002.

[102] G. C. Mathews, M. G. Blaisdell, C. D. Lemcherfi Aaron I. Slabaugh, and C. S. Goldenstein, "High-bandwidth laser-absorption measurements of temperature, pressure, CO, and H_2O in the annulus of a rotating detonation rocket engine," 2021, p. 1.

[103] G. C. Mathews and C. S. Goldenstein, "Near-GHz scanned-wavelength-modulation spectroscopy for MHz thermometry and H_2O measurements in aluminized fireballs of energetic materials," *Applied Physics B: Lasers and Optics*, vol. 126, no. 11, pp. 1–17, 2020.

[104] V. Radhakrishna, R. J. Tancin, G. C. Mathews, R. P. Lucht, and C. S. Goldenstein, "Single-shot ultrafast-laser-absorption measurements of temperature, CO, NO, and H_2O in HMX fireballs," in *AIAA Scitech 2021 Forum*, 2021, p. 1.

[105] B. J. McBride, *Computer program for calculation of complex chemical equilibrium compositions and applications*. NASA Lewis Research Center, 1996, vol. 2.

[106] W. Cai, P. Thakre, and V. Yang, "A model of AP/HTPB composite propellant combustion in rocket-motor environments," *Combustion Science and Technology*, vol. 180, no. 12, pp. 2143–2169, 2008.

[107] M. D. Ruesch, A. J. McDonald, G. C. Mathews, S. F. Son, and C. S. Goldenstein, "Characterization of the influence of aluminum particle size on the temperature of composite-propellant flames using CO absorption and AlO emission spectroscopy," *Proceedings of the Combustion Institute*, 2020.

[108] A. McDonald, R. J. Tancin, M. Ruesch, and C. S. Goldenstein, "Spectrally resolved, 1D, mid-infrared imaging of temperature, CO_2, and HCl in AP-HTPB propellant flames," in *AIAA Scitech 2021 Forum*, 2021, p. 0723.

[109] S. P. Kearney and D. R. Guildenbecher, "Temperature measurements in metalized propellant combustion using hybrid fs/ps coherent anti-stokes raman scattering," *Applied Optics*, vol. 55, no. 18, pp. 4958–4966, 2016.

[110] M. Ruesch, G. C. Mathews, M. G. Blaisdell, S. F. Son, and C. S. Goldenstein, "Scanned-wavelength-modulation spectroscopy in the mid-infrared for measurements of temperature and CO in aluminized composite propellant flames," in *AIAA Scitech 2020 Forum*, 2020, p. 0527.

[111] C. Dennis and B. Bojko, "On the combustion of heterogeneous AP/HTPB composite propellants: A review," *Fuel*, vol. 254, p. 115 646, 2019.

[112] S. Wang, D. F. Davidson, and R. K. Hanson, "High temperature measurements for the rate constants of C_1–C_4 aldehydes with OH in a shock tube," *Proceedings of the Combustion Institute*, vol. 35, no. 1, pp. 473–480, 2015.

[113] R. Sivaramakrishnan, M.-C. Su, J. Michael, S. Klippenstein, L. Harding, and B. Ruscic, "Rate constants for the thermal decomposition of ethanol and its bimolecular reactions with OH and D: reflected shock tube and theoretical studies," *The Journal of Physical Chemistry A*, vol. 114, no. 35, pp. 9425–9439, 2010.

[114] S. M. Bogdonoff and A. G. Hammitt, "Fluid dynamic effects at speeds from M = 11 to 15," *Journal of the Aeronautical Sciences*, vol. 23, no. 2, pp. 108–116, 1956.

[115] J. C. Breeze and C. Ferriso, "Integrated intensity measurements on the fundamental and first overtone band systems of CO between 2500° and 5000° K," *The Journal of Chemical Physics*, vol. 43, no. 9, pp. 3253–3258, 1965.

[116] L. Rothhardt, J. Mastovsky, and J. Blaha, "Breakdown experiments in diluted SF_6 at elevated temperatures," *Journal of Physics D: Applied Physics*, vol. 18, no. 10, p. L155, 1985.

[117] M. F. Campbell, D. F. Davidson, R. K. Hanson, and C. K. Westbrook, "Ignition delay times of methyl oleate and methyl linoleate behind reflected shock waves," *Proceedings of the Combustion Institute*, vol. 34, no. 1, pp. 419–425, 2013.

[118] Z. E. Loparo, E. Ninnemann, K. Thurmond, A. Laich, A. Azim, A. Lyakh, and S. S. Vasu, "Acousto-optically modulated quantum cascade laser for high-temperature reacting systems thermometry," *Optics Letters*, vol. 44, no. 6, pp. 1435–1438, 2019.

[119] D. V. Kotov, H. C. Yee, M. Panesi, D. K. Prabhu, and A. A. Wray, "Computational challenges for simulations related to the NASA electric arc shock tube (EAST) experiments," *Journal of Computational Physics*, vol. 269, pp. 215–233, 2014.

[120] P. M. Chu, F. R. Guenther, G. C. Rhoderick, and W. J. Lafferty, "The NIST quantitative infrared database," *Journal of Research of the National Institute of Standards and Technology*, vol. 104, no. 1, p. 59, 1999.

[121] S. W. Sharpe, T. J. Johnson, R. L. Sams, P. M. Chu, G. C. Rhoderick, and P. A. Johnson, "Gas-phase databases for quantitative infrared spectroscopy," *Applied Spectroscopy*, vol. 58, no. 12, pp. 1452–1461, 2004.

[122] Y. Ding, C. L. Strand, and R. K. Hanson, "High-temperature mid-infrared absorption spectra of methanol (CH_3OH) and ethanol (C_2H_5OH) between 930 and 1170 cm^{-1}," *Journal of Quantitative Spectroscopy and Radiative Transfer*, vol. 224, pp. 396–402, 2019.

[123] Y. Ding, W. Peng, C. Strand, and R. Hanson, "Quantitative measurements of broadband mid-infrared absorption spectra of formaldehyde, acetaldehyde, and acetone at combustion-relevant temperatures near 5.7 μm," *Journal of Quantitative Spectroscopy and Radiative Transfer*, vol. 248, p. 106 981, 2020.

[124] Y. Ding, W.-W. Su, S. E. Johnson, C. L. Strand, and R. K. Hanson, "Temperature-dependent absorption cross section measurements for propene, 1-butene, cis-/trans-2-butene, isobutene and 1, 3-butadiene in the spectral region 8.4–11.7 μm," *Journal of Quantitative Spectroscopy and Radiative Transfer*, vol. 255, p. 107 240, 2020.

[125] R. Sur, R. M. Spearrin, W. Y. Peng, C. L. Strand, J. B. Jeffries, G. M. Enns, and R. K. Hanson, "Line intensities and temperature-dependent line broadening coefficients of q-branch transitions in the v_2 band of ammonia near 10.4 μm," *Journal of Quantitative Spectroscopy and Radiative Transfer*, vol. 175, pp. 90–99, 2016.

[126] G. Pang, D. Davidson, and R. Hanson, "Experimental study and modeling of shock tube ignition delay times for hydrogen–oxygen–argon mixtures at low temperatures," *Proceedings of the Combustion Institute*, vol. 32, no. 1, pp. 181–188, 2009.

[127] M. Chaos and F. L. Dryer, "Chemical-kinetic modeling of ignition delay: Considerations in interpreting shock tube data," *International Journal of Chemical Kinetics*, vol. 42, no. 3, pp. 143–150, 2010.

[128] K. L. Wray and J. D. Teare, "Shock-tube study of the kinetics of nitric oxide at high temperatures," *The Journal of Chemical Physics*, vol. 36, no. 10, pp. 2582–2596, 1962.

[129] E. L. Petersen and R. K. Hanson, "Nonideal effects behind reflected shock waves in a high-pressure shock tube," *Shock Waves*, vol. 10, no. 6, pp. 405–420, 2001.

[130] K. Bensassi and A. M. Brandis, "Time accurate simulation of nonequilibrium flow inside the NASA Ames electric arc shock tube," in *AIAA Scitech 2019 Forum*, 2019, p. 0798.

[131] M. F. Campbell, "Studies of biodiesel surrogates using novel shock tube techniques," PhD thesis, Stanford University, 2014.

[132] D. I. Pineda, F. A. Bendana, and R. M. Spearrin, "Competitive oxidation of methane and C2 hydrocarbons discerned by isotopic labeling and laser absorption spectroscopy of CO isotopologues in shock-heated mixtures," *Combustion and Flame*, vol. 224, pp. 54–65, 2021.

[133] J. W. Hargis, B. Guo, and E. L. Petersen, "A new high-pressure aerosol shock tube for the study of liquid fuels with low vapor pressures," *Review of Scientific Instruments*, vol. 91, no. 12, p. 124 102, 2020.

[134] F. A. Bendana, D. D. Lee, C. Wei, D. I. Pineda, and R. M. Spearrin, "Line mixing and broadening in the v(1→3) first overtone bandhead of carbon monoxide at high temperatures and high pressures," *Journal of Quantitative Spectroscopy and Radiative Transfer*, vol. 239, p. 106 636, 2019.

[135] M. Figueroa-Labastida, J. Badra, A. M. Elbaz, and A. Farooq, "Shock tube studies of ethanol preignition," *Combustion and Flame*, vol. 198, pp. 176–185, 2018.

[136] J. Yoo, D. Mitchell, D. Davidson, and R. Hanson, "Near-wall imaging using toluene-based planar laser-induced fluorescence in shock tube flow," *Shock Waves*, vol. 21, no. 6, p. 523, 2011.

[137] T. Parker, R. Foutter, and W. Rawlins, "A pulsed particle injection system for shock tube studies of powders," *Review of Scientific Instruments*, vol. 72, no. 1, pp. 263–267, 2001.

[138] P. Lynch, H. Krier, and N. Glumac, "Emissivity of aluminum-oxide particle clouds: Application to pyrometry of explosive fireballs," *Journal of Thermophysics and Heat Transfer*, vol. 24, no. 2, pp. 301–308, 2010.

[139] D. R. White, "Influence of diaphragm opening time on shock-tube flows," *Journal of Fluid Mechanics*, vol. 4, no. 6, pp. 585–599, 1958.

[140] G. Fukushima, T. Tamba, A. Iwakawa, and A. Sasoh, "Influence of cellophane diaphragm rupture processes on the shock wave formation in a shock tube," *Shock Waves*, vol. 30, no. 5, pp. 545–557, 2020.

[141] C. Simpson, T. Chandler, and K. Bridgman, "Effect on shock trajectory of the opening time of diaphragms in a shock tube," *The physics of Fluids*, vol. 10, no. 9, pp. 1894–1896, 1967.

[142] E. Rothkopf and W. Low, "Diaphragm opening process in shock tubes," *The Physics of Fluids*, vol. 17, no. 6, pp. 1169–1173, 1974.

[143] E. Rothkopf and W. Low, "Shock formation distance in a pressure driven shock tube," *The Physics of Fluids*, vol. 19, no. 12, pp. 1885–1888, 1976.

[144] T. Ikui and K. Matsuo, "Investigations of the aerodynamic characteristics of the shock tubes: (part 1, the effects of tube diameter on the tube performance)," *Bulletin of JSME*, vol. 12, no. 52, pp. 774–782, 1969.

[145] T. Ikui, K. Matsuo, and M. Nagai, "Investigations of the aerodynamic characteristics of the shock tubes: (part 2, on the formation of shock waves)," *Bulletin of JSME*, vol. 12, no. 52, pp. 783–792, 1969.

[146] K. Tajima, E. Outa, and G. Nakada, "Some investigations of shock tube flow: On the propagation behavior of the initial shock front," *Bulletin of JSME*, vol. 11, no. 43, pp. 116–124, 1968.

[147] M. M. Alves, "Investigation and modeling of shock wave propagation in a shock tube with a partially opened diaphragm," PhD thesis, University of Calgary, 2019.

[148] L. Houas, L. Biamino, C. Mariani, O. Igra, G. Jourdan, and A. Massol, "The effects that changes in the diaphragm aperture have on the resulting shock tube flow," *Shock Waves*, vol. 22, no. 4, pp. 287–293, 2012.

[149] A. Roshko and D. Baganoff, "A novel device for bursting shock-tube diaphragms," *Physics of Fluids*, vol. 4, no. 11, pp. 1445–1446, 1961.

[150] M. Campbell, A. Tulgestke, D. Davidson, and R. Hanson, "A second-generation constrained reaction volume shock tube," *Review of Scientific Instruments*, vol. 85, no. 5, p. 055 108, 2014.

[151] R. Andreotti, M. Colombo, A. Guardone, P. Martinelli, G. Riganti, and M. Di Prisco, "Performance of a shock tube facility for impact response of structures," *International Journal of Non-Linear Mechanics*, vol. 72, pp. 53–66, 2015.

[152] R. Alpher and D. White, "Flow in shock tubes with area change at the diaphragm section," *Journal of Fluid Mechanics*, vol. 3, no. 5, pp. 457–470, 1958.

[153] Z. Hong, D. F. Davidson, and R. K. Hanson, "Contact surface tailoring condition for shock tubes with different driver and driven section diameters," *Shock Waves*, vol. 19, no. 4, pp. 331–336, 2009.

[154] T. A. Bazyn, "Spectroscopic measurements of the combustion of aluminum and aluminum-based energetic material particles using a heterogeneous shock tube," PhD thesis, University of Illinois at Urbana-Champaign, 2006.

[155] J. Rast, "The design of flat-scored high-pressure diaphragms for use in shock tunnels and gas guns," Naval Ordnance Lab White Oak MD, Tech. Rep., 1961.

[156] D. Davidson, D. Haylett, and R. Hanson, "Development of an aerosol shock tube for kinetic studies of low-vapor-pressure fuels," *Combustion and Flame*, vol. 155, no. 1-2, pp. 108–117, 2008.

[157] A. Dufrene, M. Sharma, and J. Austin, "Design and characterization of a hyper-velocity expansion tube facility," *Journal of Propulsion and Power*, vol. 23, no. 6, pp. 1185–1193, 2007.

[158] B. A. Cruden, "Electron density measurement in reentry shocks for lunar return," *Journal of Thermophysics and Heat Transfer*, vol. 26, no. 2, pp. 222–230, 2012.

[159] W. Tsang and A. Lifshitz, "Shock tube techniques in chemical kinetics," *Annual Review of Physical Chemistry*, vol. 41, no. 1, pp. 559–599, 1990.

[160] Pfeiffer Vacuum GmbH, *"Pfeiffer Vacuum, Know How.* [Online]. Available: https://www.pfeiffer-vacuum.com/en/know-how/.

[161] C. J. E. Aul, "An experimental study into the ignition of methane and ethane blends in a new shock-tube facility," PhD thesis, Texas A & M University, 2011.

[162] J. E. Vivanco, "A new shock-tube facility for the study of high-temperature chemical kinetics," Master's thesis, 2014.

[163] P. J. Rae and S. Mcgrane, "Achievable accuracy and precision of timing with dynasen piezo electric pins," Los Alamos National Lab.(LANL), Los Alamos, NM (United States), Tech. Rep., 2018.

[164] Parker-Hannifin Corporation, *Parker o-ring handbook*, 2018. [Online]. Available: https://www.parker.com/Literature/O-Ring%5C%20Division%5C%20Literature/ORD%5C%205700.pdf.

[165] A. R. Products, *"Seal Design Guide"*, 2009. [Online]. Available: https://www.applerubber.com/src/pdf/seal-design-guide.pdf.

[166] Crystran Ltd., *The design of pressure windows*, 2014. [Online]. Available: https://www.crystran.co.uk/windows.

[167] C. D. Slabaugh, A. C. Pratt, R. P. Lucht, S. E. Meyer, M. Benjamin, K. Lyle, and M. Kelsey, "The development of an optically accessible, high-power combustion test rig," *Review of Scientific Instruments*, vol. 85, no. 3, p. 035 105, 2014.

[168] R. S. Tranter, K. Brezinsky, and D. Fulle, "Design of a high-pressure single pulse shock tube for chemical kinetic investigations," *Review of Scientific Instruments*, vol. 72, no. 7, pp. 3046–3054, 2001.

[169] H. Kellerer, A. Müller, H.-J. Bauer, and S. Wittig, "Soot formation in a shock tube under elevated pressure conditions," *Combustion Science and Technology*, vol. 113, no. 1, pp. 67–80, 1996.

[170] B. Akih-Kumgeh and J. M. Bergthorson, "Shock tube study of methyl formate ignition," *Energy & Fuels*, vol. 24, no. 1, pp. 396–403, 2010.

[171] E. L. Petersen, "A shock tube and diagnostics for chemistry measurements at elevated pressures with application to methane ignition.," PhD thesis, Stanford University, 1999.

[172] S. M. Daley, A. M. Berkowitz, and M. A. Oehlschlaeger, "A shock tube study of cyclopentane and cyclohexane ignition at elevated pressures," *International Journal of Chemical Kinetics*, vol. 40, no. 10, pp. 624–634, 2008.

[173] D. Darcy, C. J. Tobin, K. Yasunaga, J. M. Simmie, J. Würmel, W. K. Metcalfe, T. Niass, S. S. Ahmed, C. K. Westbrook, and H. J. Curran, "A high pressure shock tube study of n-propylbenzene oxidation and its comparison with n-butylbenzene," *Combustion and Flame*, vol. 159, no. 7, pp. 2219–2232, 2012.

[174] H. Ciezki and G. Adomeit, "Shock-tube investigation of self-ignition of n-heptane-air mixtures under engine relevant conditions," *Combustion and Flame*, vol. 93, no. 4, pp. 421–433, 1993.

[175] J. Herzler, M. Fikri, K. Hitzbleck, R. Starke, C. Schulz, P. Roth, and G. Kalghatgi, "Shock-tube study of the autoignition of n-heptane/toluene/air mixtures at intermediate temperatures and high pressures," *Combustion and Flame*, vol. 149, no. 1-2, pp. 25–31, 2007.

[176] T. Javed, C. Lee, M. AlAbbad, K. Djebbi, M. Beshir, J. Badra, H. Curran, and A. Farooq, "Ignition studies of n-heptane/iso-octane/toluene blends," *Combustion and Flame*, vol. 171, pp. 223–233, 2016.

[177] J. de Vries, C. Aul, A. Barrett, D. Lambe, and E. Petersen, "Shock-tube development for high-pressure and low-temperature chemical kinetics experiments," in *Shock Waves*, Springer, 2009, pp. 171–176.

[178] M. Oehlschlaeger, D. Davidson, J. Herbon, and R. Hanson, "Shock tube measurements of branched alkane ignition times and OH concentration time histories," *International Journal of Chemical Kinetics*, vol. 36, no. 2, pp. 67–78, 2004.

[179] M. A. Oehlschlaeger, "Shock tube studies of thermal decomposition reactions using ultraviolet absorption spectroscopy," PhD thesis, Stanford University Palo Alto, CA, 2005.

[180] K. Heufer, R. Fernandes, H. Olivier, J. Beeckmann, O. Röhl, and N. Peters, "Shock tube investigations of ignition delays of n-butanol at elevated pressures between 770 and 1250 K," *Proceedings of the Combustion Institute*, vol. 33, no. 1, pp. 359–366, 2011.

[181] E. L. Petersen, M. J. Rickard, M. W. Crofton, E. D. Abbey, M. J. Traum, and D. M. Kalitan, "A facility for gas- and condensed-phase measurements behind shock waves," *Measurement Science and Technology*, vol. 16, no. 9, p. 1716, 2005.

[182] D. I. Pineda, F. A. Bendana, K. K. Schwarm, and R. M. Spearrin, "Multi-isotopologue laser absorption spectroscopy of carbon monoxide for high-temperature chemical kinetic studies of fuel mixtures," *Combustion and Flame*, vol. 207, pp. 379–390, 2019.

[183] E. L. Petersen. (). Petersen research group - shock tubes, [Online]. Available: https://petersengroup.tamu.edu/facilities/shock-tubes/.

[184] B. Koroglu, O. M. Pryor, J. Lopez, L. Nash, and S. S. Vasu, "Shock tube ignition delay times and methane time-histories measurements during excess CO_2 diluted oxy-methane combustion," *Combustion and Flame*, vol. 164, pp. 152–163, 2016.

A. TOMOGRAPHY ALGORITHM EMPLOYING TIKHONOV REGULARIZATION

```
1  function [reconstruction] = tik_tomo(b,dr, alpha_o)
2
3  % This function creates a tomographic reconstruction of a field
       variable from back projected line-of-sight measurements as
       long as that field variable contributed to the back projected
       measurement linearly with path length (e.g., the local
       absorption coefficient contributes linearly to projected
       integrated absorbance). This code only works for axisymmetric
       cases.
4  %
5  % INPUTS
6  % b:    The back projected field variable. This should be a
       column vector with the first element corresponding to the
       center of the axisymmetric area (r = 0) and the last element
       corresponding to the edge (r = R)
7  %
8  % dr:   The length step for each pixel / datapoint. (i.e. the
       thickness of each "ring element" or voxel of the flame, jet,
       etc.) This is a scalar
9  %
10 % alpha_o:  The regularization parameter. This controls the
       smoothness of the reconstruction. alpha_o = 0 corresponds to
       no regularization and higher values lead to progressively
       smoother, less noise sensitive reconstructions, although with
       less fidelity to the "exact" solution. In general, the lowest
       value that yields an acceptable noise level in the solution
       should be used. This is a scalar.
```

```
11 %
12 % OUTPUT
13 % y:    The reconstructed values for the local field variable.
       This is a column vector with each element corresponding to the
        same location as in the "b" input.
14 %
15 % Written by Ryan Tancin, August 2019, Purdue University
16 % This algorithm is directly based off of work by Daun et al.
       More information can be found in  "Deconvolution of
       axisymmetric flame properties using Tikhonov regularization",
       Daun et al., 2006
17
18
19
20 %% BEGIN CODE
21
22 nPoints = length(b);
23
24 % create the coefficient matrix A
25 for i = 1:nPoints
26     for j = 1:nPoints
27         if j < i
28             A(i,j) = 0;
29         elseif j == i
30             A(i,j) = 2*dr*((j+0.5)^2 - i^2)^(0.5);
31         elseif j > i
32             A(i,j) = 2*dr*(((j+0.5)^2 - i^2)^(0.5) - ((j-0.5)^2 -
                   i^2)^(0.5));
33         end
```

```
34      end
35  end
36
37  % create L_o Matrix
38  for i = 1:nPoints
39      L_o(i,1:nPoints+1) = zeros(1,nPoints+1);
40      L_o(i,i)     = 1;
41      L_o(i,i+1)   = -1;
42  end
43
44  L_o(:,end) = [];
45
46  A_Tik = (A'*A + alpha_o*A*(L_o'*L_o));
47
48  % solve for local field variable
49  b_Tik = A'*b;
50  x1 = (A_Tik\b_Tik)';
51
52  reconstruction = x1';  % change output vector to column vector
```

B. O-RING SEAL DESIGN

The purpose of this appendix is to outline the important considerations and design trade-offs when designing an O-ring seal for high pressure or vacuum. This is meant to be a starting point, and not an exhaustive guide. Two excellent resources for more detailed design information and tables of pertinent gland/groove and O-ring dimensions with tolerances are "The Parker O-ring Handbook" [164] and the Apple Rubber "Seal Design Guide" [165].

B.1 O-ring Seal Design Parameters

Seals are critical to the performance of any high- or low-pressure containing vessel. Proper seal design minimizes leak rates which is critical for keeping toxic gases contained inside a vessel, preventing external contaminates from entering the vessel, lowering the minimum pressure achievable (for vacuum vessels) and helping to maintain constant pressures during experiments. Sealing for the equipment designed in this dissertation was achieved through O-ring seals. The seal is created between two parts using an elastomer torus (the O-ring) which is typically installed into a groove machined into the surface of one the parts. The seal is created when the parts are mechanically mated, compressing the o-ring against the opposing surface of the mated part. As a pressure differential is created across the O-ring, it is forced into the corner of the gland. The greater the pressure, the harder the O-ring is forced into the corner and the tighter the seal becomes. The "Groove" refers to the recess machined into one of the mating surfaces, while "gland" refers to the entire area between the groove and the opposite mating surface where the O-ring is contained. When calculating the area on which system pressure is acting, the area of the groove should also be counted. In other words, system pressure is not sealed where the O-ring groove starts, but rather, where it ends (i.e., the low pressure side when sealing a high-pressure fluid).

O-rings are standardized using the SAE AS-568 standard. Sizes are specified using a "dash number" which is of the form -ABB, where A indexes the O-ring's cross-sectional thickness and BB indexes the O-ring's internal diameter. Dimensions and tolerances for grooves are specified for each O-ring size and configuration (i.e., radial or face seal). The dimensions and their tolerances are found in engineering tables such as those contained

within the Parker O-ring Handbook [164]. O-rings with larger cross section diameters require grooves with looser tolerances and have larger contact area between mating surfaces, thus, providing better sealing. Generally, the largest possible O-ring cross section should be selected for an application. Other O-ring cross-section shapes are also available, such as square or "X" shaped for different applications. Square cross sections can provide more contact area with mating surfaces and thus yield a tighter seal.

The surface of glands should have a smooth surface finish to minimize leaking. Lower values of RMS roughness yield lower leak rates. An RMS roughness of 16 μin (ISO grade N5) or lower is preferred for sealing gases and 32 μin (ISO grade N6) or lower for sealing liquids. In applications where the groove must mechanically retain the O-ring, a dovetail groove can be employed, at the cost of increased complexity and machining time.

Some important seal design considerations are listed below for convenience. This list is by no means complete.

- **Squeeze:** This is the amount that an O-ring is compressed when properly installed, usually expressed as a percentage of the O-ring's nominal cross-section. Higher % squeeze yields a tighter seal, but requires higher installation force, potentially leading to O-ring damage. Squeeze should not exceed 20% for radial seals but up to 30% can be used in face seal applications. Squeeze is determined by groove depth for face seals and gland depth (groove depth + gap between cylinder wall and piston) for radial seals [164].

- **Compression Set:** Compression set is permanent deformation of the O-ring, typically expressed as a percentage of the undeformed O-ring's cross section. Different O-ring materials have different compression set properties. Further, compression set may change with time for a given O-ring. Generally, harder O-ring materials exhibit higher levels of compression set. Compression set leads to reduced seal performance over time, and eventually to failure.

- **Hardness:** The resistance of an O-ring to distortion. The hardness of an O-ring is usually measured using the durometer (Shore A) hardness scale. Harder O-rings seal with greater force for a given % compression. Hence, a harder O-ring may provide

a tighter seal when there is a low pressure difference across an O-ring. However, higher hardness O-rings also conform less to surface imperfections. Harder O-rings are less prone to failure by extrusion, but can be difficult to assemble in piston seal configurations [164], [165].

- **O-ring stretch:** In piston seal configurations, the ID of the groove is typically slightly larger than the ID of the O-ring, meaning that the O-ring is slightly stretched in order to keep the O-ring in position during assembly. Note that this will slightly effect the O-rings cross section which in turn effects other parameters such as gland fill and squeeze. Equations to determine the effect of stretch on cross section dimensions can be found in the literature [164], [165]. Stretch is typically not more than 5% [164].

- **Percent gland fill:** This is the percentage of the gland's cross section which is occupied by the O-ring. Typically this ranges from 60% - 85% when sealing gases. Too high of a value can result in seal or gland failure from thermal expansion or O-ring swelling (from chemical interactions between the working fluid and O-ring) [164] Since swell is most common when the O-ring is exposed to liquids, lower gland fill percentages are typically used. In sealing vacuum, higher gland fill percentages reduces the dead volume which can trap gas, thus decreasing the pump-down time.

B.2 O-ring Seal Configurations

O-rings are most commonly used in either face seal or radial seal configurations. In the radial real configuration, the O-ring seals against pressure acting in the axial direction. Typically this uses a piston-seal design where the O-ring groove is machined into the male "piston" and not the cylinder (called a rod seal, which is less common). In certain situations, this configuration can limit the area exposed to system pressure and, thus, minimize the total force exerted by high-pressure gases or liquids. There is a small gap between the piston and bore to provide clearance for assembly. When the pressure difference across the O-ring is high, the O-ring may extrude into this gap causing failure of the seal. Extrusion can be reduced or prevented using an O-ring with a higher durometer, by reducing the gap between

piston and cylinder or by placing a backup ring on the low pressure side of the gland (note: a backup ring is *not* an O-ring, and cannot be used in place of an O-ring) made from a hard material to prevent extrusion of the O-ring. The use of one or more backup rings requires a wider groove width to accommodate the backup ring. Radial seals typically have tight tolerances which is a drawback in comparison to a face seal configuration. A shallow chamfer (10° - 20°) is used to prevent damaging the O-ring during installation, and reduce installation force.

Face seal O-rings seal against pressure acting in the radial direction. The two mating components which form the seal come into direct contact, and thus extrusion is not typically a concern. This relaxes design tolerances without the need for backup rings. The face seal configuration is generally preferable whenever possible because of this reason. The groove is dimensioned by the diameter of the low-pressure side of the groove (where the O-ring will be forced during operation). Note that extrusion can happen in the face seal configuration if pressure forces cause excessive deformation of the mating surfaces.

Both face seal and radial seal O-rings can be employed in non-circular configurations. This can help meet geometric constraints of a design or better contour a part to limit the area acted on by system pressure (e.g., for slot windows). As a rule of thumb, the radius of the bend should never be smaller than 3 times the O-ring's cross-sectional diameter, though 6 times is considered better. This is done to limit stresses within the O-ring which could lead otherwise lead to seal failure [164]. In face seal configurations, the perimeter of the low-pressure side of the groove should be equal to the circumference of the groove for a standard circular groove design.

C. ACCESS PORTS

Access ports allow for interface between the internal volume of a pressure or vacuum vessel and an external system, such as those required for delivery, venting and purging of gases, vacuum access, access for sensors (e.g., thermocouples, pressure transducers), and electrical access.

C.1 NPT Ports

One of the most commonly used port designs is the national pipe taper (NPT) threaded port (commonly shortened to "NPT port") which consists of a female tapered thread (typically cut into the wall of the vessel) and a plug with a tapered male thread. Ports are dimensioned by nominal pipe sizes. Sealing is achieved through interference between the root and crest of the threads as the plug is tightened, and the use of a thread sealant (e.g. PTFE (teflon) tape or "pipe dope") to seal and lubricate the threads. Ports should never be assembled without thread sealant, as this may result in leaks or galling, the latter of which may damage the plug or port and prevent disassembly. NPT threaded ports are used on the HPCC.

There are a number of advantages to using NPT ports. The port design is ubiquitous, and a large variety of off-the-shelf hardware and instrumentation is available with NPT threads. They are rated for medium/high pressures (> 400 bar). NPT ports are easy and cheap to machine. Disadvantages include the relatively high torque needed to seal the ports which may wear or damage threads over time. This means that NPT ports may be considered to have a finite life. There is no way to tell if a port is properly assembled. Tightening depends in part on "feel" and performance can depend on the skill with which sealant is applied. Installed NPT ports are prone to cracking when heated, due to the high amount of force between the male and female threads. Further, the need for thread sealant requires that the threads be cleaned of residual sealant after disassembly, and thread sealant reapplied before reuse. NPT ports have higher leak rates than ports with O-ring seals. Last, certain thread sealants/lubricants (e.g. "pipe dope") can introduce contaminants into the system.

C.2 O-ring Boss Ports

Another common type of port is the O-ring boss port, otherwise known by its SAE and ISO designations, SAE J-1926-1 and ISO-11926-1, respectively. These ports (shown in Fig. 8.8) similarly rely on a female threaded port machined into the wall of the vessel and a male threaded plug which interfaces with some external system. Unlike NPT ports, these rely on straight threads, and sealing is instead achieved through an O-ring which is fitted around the base of the male thread between the end of the thread and the hex. When the port is assembled, the O-ring is forced into a boss at the start of the female thread which provides sealing for the port. Ports are dimensioned fractionally or in metric. They are also often sized using a "dash number" which corresponds to the OD of the tube it is designed for in increments of $\frac{1}{16}$" (e.g., a -8 fitting corresponds to a fitting for a $\frac{1}{2}$" OD tube). O-rings for straight threaded tube connections are specified using the SAE, AS568 standard, with dash numbers of the form -9XX, where 9 specifies that the O-ring is for straight threaded fittings and XX is the fitting dash number (i.e. a fitting for a tube diameter of $\frac{1}{2}$" would need a -908 O-ring). Installing high durometer (e.g., PTFE which has a durometer of 90A) O-rings onto male threaded ports can be extremely difficult without special tooling. Softer durometers should be used where possible.

There are numerous advantages of O-ring boss ports. First, the torque needed to install the port is drastically reduced, and proper installation of the port is easily visible (when the fitting's hex is in contact with the surface of the female boss). Unlike NPT ports, they can be uninstalled and reinstalled repeatedly with no changing of seals or sealants, there is little wear to the port over time, and they typically have lower leak-rates. These advantages are common to other ports which use O-rings seals (e.g., face-seal O-ring ports). The primary disadvantage of this type of port is that they are somewhat less common and it may be difficult to find a commercial adapter or feed-through for a given system or component. Due to the overall advantages of O-ring boss ports, this port design was chosen for use on the Purdue HPST.

C.3 Wire Feedthroughs

For the work described within this dissertation, feedthrough of wires was achieved through drilling a hole through a blank, male-threaded port plug. The wires were fed through the hole and subsequently sealed with a 2-part adhesive such as JB Weld. While purpose-built feedthroughs can be bought commercially for high-pressure and vacuum applications, this methods was chosen for its low cost and on-the-fly adaptability. This may not be suitable for high-vacuum situations where outgassing of epoxy could be a concern. One potential solution is to use Swagelok compression fittings, since the ferrules will seal against anything of the correct diameter.

D. DESIGN CONSIDERATIONS FOR HIGH- AND LOW-PRESSURE WINDOWS

Windows are used to allow optical access into high- or low-pressure chambers or vessels while preventing the entrance or escape of gases. Windows on the HPCC and HPST are held in place using machined stainless steel window holders. The holder consists of a seat (i.e., a step which supports the window, see Fig. D.1) which acts to support the window from the low-pressure side. For vessels such as the HPCC and HPST which are designed to operate at both high and low pressures, the seat should support the window in the direction which will see a larger force. For the HPCC and Purdue shock tube, windows are sealed using a thermally curing epoxy (EPO-TEK T7109). The window seat should be machined such that there is a 0.01" gap between the window's diameter and the window holder to provide an optimal amount of space for the epoxy. The width of the shoulder/seat which the window rests on does not affect the pressure rating of the window as long as the unsupported radius remains the same. A wider shoulder may potentially yield a tighter seal against vacuum or pressure, but, at the cost of reducing the clear aperture for a given window and window holder size.

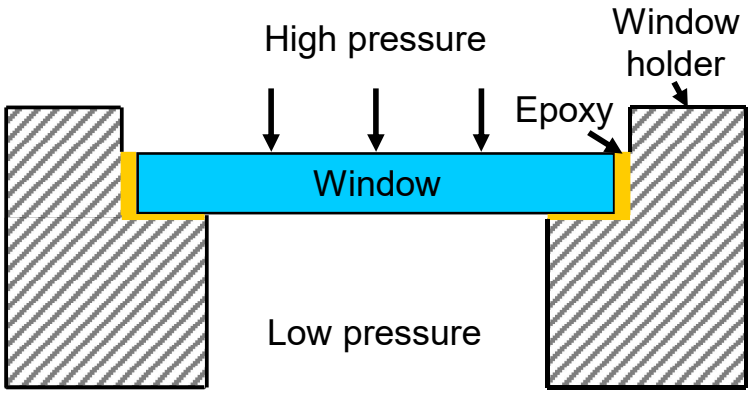

Figure D.1. Diagram showing the typical design of pressure windows for an experimental vessel. Gold lines indicate the location of epoxy seals.

The pressure rating of round windows is determined through Eq. D.1, and the pressure rating of slot or rectangular windows is determined through Eq. D.2 [166].

$$Th = \sqrt{\frac{1.1 \times P \times R^2 \times SF}{MR}} \tag{D.1}$$

$$Th = \sqrt{\frac{2.25 \times P \times L^2 \times SF}{MR + (1 + (L/W)^2)}} \tag{D.2}$$

Here, Th is the thickness of the window [m], P is the pressure [Pa], R is the unsupported radius [m], SF is the safety factor, MR is the modulus of rupture for the window material [Pa], L is the unsupported length of a rectangular window [m] and W is the unsupported width of a rectangular window [m]. Note that while Eq. D.2 is meant for rectangular windows, but provides a conservative estimate for slot shaped ones as well. Both Eq. D.1 and Eq. D.2 assume an unclamped edge condition for the windows, which is likely not entirely correct when using epoxy seals, though this also yields conservative calculations since the unclamped boundary condition yields a lower pressure rating for a given window and window holder geometry. A safety factor of 4 is recommended for windows. For wedged windows, the thickness used is the minimum thickness of the window. For complex window shapes (e.g., wedged slot windows) calculations are verified using FEA simulations to determine the maximum stress a window will experience. Note that this analysis is meant for windows at room temperature. Additional analysis is needed if windows will be subject to thermal gradients, as these introduce thermal stresses and alter the material properties of the window [167]. It is suspected that window failure on many combustion test rigs is due to thermal stress.

E. LIST OF ACTIVE SHOCK TUBE FACILITIES

Table E.1. Dimensions and other relevant parameters for several shock tube facilities around the world. This list (which is by no means exhaustive) was started from a similar table created by Campbell [131] but has since been expanded as more facilities have come into operation.

Institution	Description	Country/state	Driver			Driven			Driver/driven length ratio	Source
			ID [cm]	L [m]	Vol. [L]	ID [cm]	L [m]	Vol. [L]		
UIC		USA/Illinois	5.08	1.52	3.08	2.54	4.1	2.08	0.4	[168]
KIT		Germany	3.14	1.98	1.53	3.14	2.97	2.3	1.5	[169]
Stanford Uni.	CRVST	USA/California	16.05	13.42	271.51	11.53	0.4	4.18	0.03	[150]
McGill Uni.		Canada/Quebec	5	3	5.89	5	4.2	8.25	1.4	[170]
Stanford Uni.	HPST	California	7.62	3	13.68	5	5	.82	1.7	[171]
RPI		USA/New York	2.59	5.7	3	5.7	4.11	10.49	0.7	[172]
NUI Galway		Ireland	6.3	3.03	9.45	6.3	5.73	17.86	1.9	[173]
RWTH Aachen		Germany	8.7	5.3	31.51	8.7	6.3	37.45	1.2	[174]
Duisburg-Essen		Germany	9	6.1	38.81	9	6.4	40.72	1	[175]
KAUST	HPST	Saudi Arabia	10	2.2-6.6	17-52	10	6.6	54.98	1-3	[176]
Texas A&M	HPST	USA/Texas	7.62	2.46	11.22	15.24	4.72	86.1	1.9	[177]
Stanford Uni.	CRVST (conv.)	USA/California	16.05	13.42	271.51	11.53	9.73	101.59	0.7	[150]
Stanford Uni.	KST	USA/California	14.13	7.12	111.65	14.13	8.54	133.92	1.2	[178], [179]
KAUST	LPST	Saudi Arabia	14.2	9.1	138.54	14	9.1	138.54	1	[135]
RWTH Aachen		Germany	14	4.5	69.27	14	11	169.33	2.4	[180]
Stanford Uni.	NASA Tube	USA/California	15.24	7.55	137.72	15.24	10.51	191.72	1.4	[178]
Texas A&M	AeroST	USA/Texas	7.62	3.5	15.96	16.2	10.7	220.55	3.1	[181]
UCLA	HEST	USA/California	10.3	1.6-5.8	13-48	10.3	4.88	0.82	0.8-3.1	[132], [182]
Texas A&M	AST	USA/Texas	19.4	6.6	196	15.2	5.5	99.8	0.83	[133]
Texas A&M	Square ST	USA/Texas	.6	2	9.1	10.8	4	16.6	2	[183]
UCF		USA/Florida	14.2	4.9	77.6	14.2	8.5	134.6	1.73	[184]
UIUC		USA/Illinois	16.5	3.05	65.2	8.9	8.4	52.2	2.8	[154]
Purdue Uni.	HPST	USA/Indiana	10.3	3-6	28-57	10.3	6.6	55.0	1.1-2.2	

F. HPST MODIFICATIONS TO CORRECT FOR MANUFACTURING ERRORS

Slight modifications to several HPST components were required to correct for out of tolerance concentricity of various inline components (e.g., tube sections). These errors were caused by the dimensions of several HPST components being manufactured outside of their specified tolerance. The result was a mismatch between the inner bore of adjacent components causing an edge or step on the tube wall which would have negatively effected the incident shock wave and test conditions. The affected areas were the butt-ends of the tube sections (described in chapter 8.4.2), where it was found that the OD and ID of the tubes ends were not machined concentric. Adjacent components are held concentric by the close fit between the OD of the tube's butt and the ID of a socket (or ring in the case of tube-to-tube connections) of the adjacent component. Therefore, if the OD and ID of the tube is not concentric, then the socket will hold the tube in a position where the ODs of adjacent components are concentric but not the IDs. This is illustrated by a schematic in Fig. F.1a.

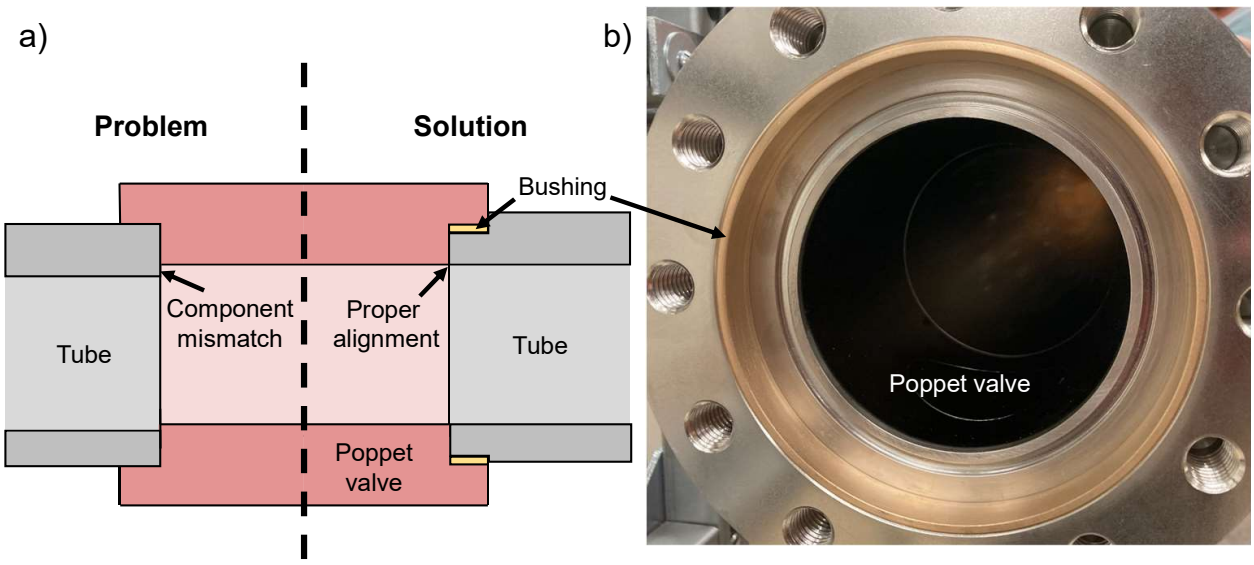

Figure F.1. Modifications to tube connections to fix concentricity errors. (a) A cross-section diagram showing the source of the concentricity error, and the solution to fix it. The mismatch has been exaggerated for clarity. (b) A photo of a tube socket on the poppet valve showing the bushing installed to fix the concentricity error.

The solution adapted by the manufacturer was to machine the OD of each tube section concentric with the tubes ID. The length of the OD which was turned true was $\geq$ the depth of the tube sockets. Therefore, a brass bushing was pressed into each tube socket, such that the each socket's ID now matched the new OD of the tube butts. A diagram illustrating the solution is shown in Fig. F.1a and a photograph of a bushing pressed into the poppet valve body is shown in Fig. F.1b. All tube ends except for the driver endwall were modified. FEA simulations were re-run in order to verify that the modifications did not alter the pressure capabilities of the HPST. The modifications were successful in correcting all concentricity errors between HPST components.

G. PUBLICATIONS

G.1 Journal Publications During Ph.D. Period

1. R. J. Tancin, G. C. Mathews, and C. S. Goldenstein, "Design and application of a high-pressure combustion chamber for studying propellant flames with laser diagnostics," *Review of Scientific Instruments*, vol. 90, no. 4, p. 045111, 2019. doi: https://-doi.org/10.1063/1.5081671

2. R. J. Tancin, R. M. Spearrin, and C. S. Goldenstein, "2D mid-infrared laser-absorption imaging for tomographic reconstruction of temperature and carbon monoxide in laminar flames," *Optics Express*, vol. 27, no. 10, p. 14184, 2019. doi: https://-doi.org/10.1364/OE.27.014184

3. R. J. Tancin, Z. Chang, M. Gu, V. Radhakrishna, R. P. Lucht, C. S. Goldenstein, "Ultrafast laser-absorption spectroscopy for single-shot, mid-infrared measurements of temperature, CO, and CH_4 in flames," *Optics Letters*, vol. 45, no. 2, pp. 583–586, 2020

G.2 Conference Publications During Ph.D. Period

1. R. J. Tancin, Z. Chang, V. Radhakrishna, M. Gu, R. P. Lucht, C. S. Goldenstein, "Ultrafast laser absorption spectroscopy in the mid-infrared for measuring temperature and species in combustion gases," in *AIAA Scitech 2020 Forum*, 2020, p. 0517

2. R. J. Tancin, M. Ruesch, S. F. Son, R. P. Lucht, C. S. Goldenstein, "Ultrafast-laser-absorption-spectroscopy measurements of gas temperature in multi-phase, high-pressure combustion gases," in *AIAA Scitech 2021 Forum*, 2021, p. 0719. doi: https://-doi.org/10.2514/6.2021-0719

3. R. J. Tancin, R. M. Spearrin, and C. S. Goldenstein, "Mid-infrared laser-absorption imaging of temperature and CO in laminar flames," in *11th National Combustion Meeting*, 2019

4. A. McDonald, R. J. Tancin, M. Ruesch, C. S. Goldenstein, "Spectrally resolved, 1D, mid-infrared imaging of temperature, CO_2, and HCl in AP-HTPB propellant flames," in *AIAA Scitech 2021 Forum*, 2021, p. 0723

5. V. Radhakrishna, R. J. Tancin, G. C. Mathews, R. P. Lucht, C. S. Goldenstein, "Single-shot ultrafast-laser-absorption measurements of temperature, CO, NO, and H_2O in HMX fireballs," in *AIAA Scitech 2021 Forum*, 2021

6. M. McClain, M. Ruesch, R. J. Tancin, C. N. Dennis, C. S. Goldenstein, S. F. Son, "Characterization of the melt layer of ammonium perchlorate single crystals," in *AIAA Propulsion and Energy 2020 Forum*, 2020, p. 3902

G.3 Publications in Progress

1. R. J. Tancin, M. Ruesch, S. F. Son, R. P. Lucht, C. S. Goldenstein, "Ultrafast-laser-absorption-spectroscopy measurements of gas temperature and CO in multi-phase, high-pressure combustion gases," *Optics Express*, 2021: Ready to submit

2. A. McDonald, R. J. Tancin, and C. S. Goldenstein, "Spectrally resolved, 1D, mid-infrared imaging of temperature, CO_2, and HCl in propellant flames," *Applied Physics B: Lasers and Optics*, 2021: Accepted pending revisions

3. V. Radhakrishna, R. J. Tancin, G. C. Mathews, R. P. Lucht, C. S. Goldenstein, "Single-shot mid-infrared ultrafast-laser-absorption-spectroscopy measurements of temperature, CO, NO, and H_2O in HMX combustion gases.," *Applied Physics B: Lasers and Optics*, 2021: Ready to submit

4. R. J. Tancin, M. Ruesch, S. F. Son, R. P. Lucht, C. S. Goldenstein, "Spatially resolved ultrafast-laser-absorption-spectroscopy measurements of CO, HCl and temperature in aluminum and aluminum-lithium propellant flames," *Combustion and Flame*, 2021: In progress